FAULT MITIGATION IN PERMANENT MAGNET SYNCHRONOUS MOTORS UNDER AN INTERNAL TURN-TO-TURN FAILURE

By

Jorge G. Cintron-Rivera

A DISSERTATION

Submitted to
Michigan State University
in partial fulfillment of the requirements
for the degree of

Electrical Engineering - Doctor of Philosophy

2014

ABSTRACT

FAULT MITIGATION IN PERMANENT MAGNET SYNCHRONOUS MOTORS UNDER AN INTERNAL TURN-TO-TURN FAILURE

By

Jorge G. Cintron-Rivera

In this research the behavior and mitigation of turn-to-turn faults in PMSMs are studied. The challenge with PMSMs under a turn-to-turn fault is with the rotor magnets. Typically rare earth magnets are used in PMSMs, due to the high remnant flux density and excellent coercivity. These characteristics make rare earth magnets the strongest commercially available. Thanks to this, healthy PMSMs have high torque density and are suitable for traction and power generation systems. However, what makes them excellent machines also makes them dangerous in the event of a turn-to-turn fault. The problem arises when a fault occurs and the magnetic field produced by the magnets continuously contributes to the fault by electromagnetic induction. Magnets are capable of inducing high voltages in the windings and they cannot be turned off during fault conditions. In post-fault operation, if the rotor continues spinning, even a full inverter disconnection will not assist in the mitigation of the fault current.

This research demonstrates how to detect a fault and reduce the fault current by controlling the current through the remaining healthy coils. The main idea is to generate a magnetic field, using the remaining healthy coils, to cancel some of the magnetic field created by the magnets. Although magnets cannot be turned off, their effect in the faulted area can be minimized using this technique. The technique applies the principle of the field-weakening control strategy to reduce the magnetic flux linking the fault, and therefore reduce and gain a degree of control over the fault current. This mitigation technique keeps the fault current

within acceptable levels and if conditions allow, the faulted PMSM can continue operating with a reduced power capacity. This has the potential of extending the post-fault life span of the motor, which could allow for continuous operation at least for a limited time.

Two fault tolerant PMSMs, with fractional winding configuration, were designed to test the proposed mitigation technique. The difference between the motors is in the number of layers in the winding and the slot/pole/phase combination. One machine has a single layer winding using a 2/5 slots/pole/phase combination, while the other has a double layer winding with a 1/2 slots/pole/phase combination. Through experimental and finite elements analysis this dissertation demonstrates the effectiveness of the proposed fault mitigation technique in regulating the fault current during a turn-to-turn fault.

I dedicate this Dissertation to my wife Sheila Liz Luna-Miranda, who offered me unconditional love and support throughout the course of my Ph.D. career; and to my unborn baby, who brings happiness and joy to our lives.

I would also like to dedicate this Dissertation to my parents Aracelis Rivera-Morales and Efrain Cintron-Rosado, for their love and unconditional support.

ACKNOWLEDGMENTS

First, I would like to thank God for the health and strength provided to me and to everyone. Without these qualities, this career would not be possible. Also, thanks for all the wisdom and knowledge gained during my Ph.D career.

Special thanks to my wife, Sheila Liz Luna-Miranda, for her unconditional support with my professional and personal goals. She has been with me during this wonderful journey, helping me to overcome problems and giving me the strength to accomplish this goal. I want to thank my parents, Aracelis Rivera-Morales and Efrain Cintron-Rosado, for their unconditionally support and all the strong values and perseverance they taught me. Also, thanks to all my family members, especially to Carmen and Pedro Vazquez, who together with my parents gave me that initial push to start my Ph.D and continous support throughout my entire professional career.

I would like to thank my research advisor Dr. Elias G. Strangas, for his support, guidance, confidence and motivation to pursue and complete my doctoral degree. Also, I would like thank my graduate committee; Dr. Fang Peng, Dr. Joydeep Mitra, Dr. Ranjan Mukherjee, for their guidance and support.

This work was possible thanks to the collaboration and support from my excellent friends in the Electrical Machines and Drives Laboratory; thank you all. The relationships built in our Laboratory are remarkable, and for that I am grateful.

Finally, I would like to thank Michigan State University for the Enrichment Fellowship, and Dr. Percy Pierre for the Sloan Engineering Program support. Also, I would like to thank the UNCF special programs corporation for the NASA's Harriett Jenkins pre-doctoral fellowship.

TABLE OF CONTENTS

LIST OF TABLES

LIST OF FIGURES

Chapter 1

Introduction

Permanent magnet synchronous motors (PMSM) are used in many commercial products. Their high power density and torque capacity make them suitable for traction drives applications. Automotive industries exploit these features to design and fabricate vehicles with exceptional MPG performance to satisfy the needs of the consumers and alleviate the air pollution problem. The outstanding performance of PMSMs overcomes their main drawback, which is that strong magnets, made from rare earth materials, are required to achieve suitable operation. Rare earth materials increase the production cost; however, the resulting performance and power capacity are worth the cost.

Having strong magnets permanently inserted into a PMSM can be hazardous in the event of a failure, especially for a turn-to-turn fault in the winding. This is because having a high magnetic field contained within a faulted stator winding has the potential to induce voltages across the fault. The magnetic field produced by these magnets is not controllable and cannot be turned off. When a fault occurs, magnets contribute to the fault current, which leads to overheating and possible destruction of the machine and its surroundings.

Considering that these motors are widely utilized in applications where human interaction is required, it is vital to develop a safety response protocol to any type of fault in a PMSM, a protocol that ensures the safety of the users, as well as, the overall integrity of the entire system.

1.1 Literature Review on Faults of PMSMs

Faults in PMSMs are categorized into mechanical or electrical [1]; mechanical faults include rotor eccentricity, shaft bearings deterioration and parts breakage. On the other hand, electrical faults include, magnet demagnetization, open circuit phase, turn-to-turn contact due to insulation degradation, and failure of electronics, [2].

Open circuit phase faults occur when a phase winding breaks or when an electronic switching device fails, [3]. Extensive research has been performed for open circuited phase remedial strategies, [4–7]. It has been demonstrated that acceptable post-fault operation may be achievable in three phase machines by controlling the neutral current using a fourth inverter leg, [8–10]; other remedial strategies were developed for PMSMs with more than three phases, [11].

This Dissertation is entirely focused on the mitigation of turn-to-turn short faults, which are among the most common faults in PMSMs, 30 % to 40 %, [12–15]. Contrary to open circuit faults, there is no remedial strategy to safely achieve full post-fault operation in turn-to-turn faulted PMSMs. These faults can occur between turns of the same or different phases, [16]. However, faults tend to occur between turns of the same phase coil, especially when a fault tolerant PMSM is used. In this type of motor the phase windings do not share any of the slots; hence, the phase to phase mutual inductances are dramatically reduced, and the phases are physically isolated [17]. Yet, without a proper mitigation, an incipient turn-to-turn fault can easily propagate to more turns and worsen the severity of the contact point resistance. This is due to the rapid increase in the coil temperature, caused by a large circulating fault current, [18]. It is vital to detect and mitigate incipient turn-to-turn faults to stop and prevent further damage to the PMSM, [18]. The effects of an turn-to-turn fault

on the vector oriented controller are studied in [18–20].

Several detection methods have been proposed for PMSMs, [17, 21–23]; where the unbalanced operating conditions created by the fault are used for detection purposes. For example, in [24] and [25] the voltage imbalances are used to detect the fault, while [26] and [27] use sequence component and impedance changes, respectively. The third harmonic components of line currents, also contain information about the health of the machine, as demonstrated in [15].

In the majority of the mitigation techniques, the stator current is controlled to produce a magnetic flux linkages that is equal in magnitude but opposes the flux linkage produced by the magnets. This reduces the induced EMF voltage in the faulted turns and suppresses the fault circulating current. One important aspect, is that once the fault has been detected and cleared, the machine is not operational, as its torque output capacity is completely nulled by the stator current.

One possible response to a turn-to-turn fault is to shut-down the drive's electronics. This remedial strategy is known as uncontrolled generator (UCG); it is applicable for open and turn-to-turn faults and the operation principle is described in [28, 29]. In this technique the fault current is not controlled and it can easily increase the fault severity due to over-current and overheating. In [30] a method to keep the fault current within its rated limit during a turn-to-turn fault in a bar wound machine is presented. It demonstrates that injecting rated current at 90^o lagging the back EMF results in a fault current that is kept within the rating limits of the coil, but the torque output capacity is completely nulled. In [30] this mitigation technique is compared to previously presented techniques, where the inverter was used to create a short across all phases of the motor, [31]. Shorting all phases of the motor, while operating, generates strong counter torque and transient currents capable of creating

a catastrophic failure.

Welchko et al. [32] proposed a similar method to mitigate turn-to-turn faults in PMSMs. This method consists of injecting maximum current along the d-axis when a fault is detected; this technique was named flux nulling. The magnet flux nulling technique uses the d-axis current to cancel the back EMF, so that only a small voltage is induced in the faulted winding. This method minimizes the fault current and nulls the torque capacity of the motor. Other mitigation techniques have been developed for machines containing more than the standard three phases, [33]. However, having more phases increases the cost and complexity of a machine and drive.

1.2 Problem Statement

PM motors contain magnets that are buried in or mounted on the surface of their rotors. As the rotor spins, the rotating magnetic field created by the magnets induce a voltage known as the electromotive force (EMF) in the stator windings. This physical phenomenon is described by Faraday's law of induction, which states how a changing magnetic field will interact with an electrical circuit to create an EMF. The magnitude of the EMF voltage induced in the motor stator winding is directly proportional to the rotor angular speed and the magnetic strength of the magnets.

The problem arises because the rotor magnets cannot be turned off during a fault. As the rotor moves inside the stator, the magnets induce a voltage in the faulted winding. This voltage will create a circulating fault current inside the motor that will generate heat and has the potential to propagate and/or destroy other areas of the motor. The work in this Dissertation is focused on the study and development of a fault mitigation method that has

the potential to continue the operation of a faulted PMSM.

1.3 Methodology

Here a method to mitigate turn-to-turn faults is introduced. It is demonstrated that the stator currents, at the appropriate angle and magnitude, can restrict the fault current rms value and therefore decrease the power dissipated across the fault. The idea is to use the direct axis current to adjust the amount of flux linkage that induces the back emf voltage across the fault. By canceling some of the flux produced by the magnets, it is possible to reduce the voltage across the fault and hence the fault current. This concept is described as a low-speed field-weakening, where the flux linkage produced by the magnets is weakened by the flux produced by the line current, a technique that is normally used at high speeds. However, it will be demonstrated that this technique reduces the fault current, when applied at speeds below the nominal. This leads to a controller capable of reducing the fault current and allow post-fault operation of the motor, depending on the fault severity.

The method is based on the flux nulling technique, but it also allows the injection of q-axis current that enables the PMSM's torque production. The main idea of this method is to restrict the fault current rms, to limit the fault power losses and delay the fault propagation. Here, the fault current rms is not limited to the lowest possible value, instead, it is limited to a safe level that allows the machine to continue operating under reduced capacity.

1.4 Objectives and Contributions

This objective of this dissertation is to provide a fault mitigation technique capable of limiting the amount of fault current, while allowing the PMSM to continue operating under restricted

operating conditions. High fault current levels promote the rapid propagation of the fault due to the thermal stress created by the increased fault power losses generated in a concentrated area. By using a magnetic field-weakening strategy at speeds below the nominal, to reduce the voltage induced in the faulted portion, it is possible to gain some control freedom over the fault current.

The proposed method limits the amount of fault current in order to limit the fault power losses and delay the propagation of the fault; it also includes a detection strategy and a fault parameter estimation method. Estimation of the fault parameters is vital, since these parameters are used to estimate the rms value of the fault current and take action upon the fault, if necessary.

The main research contributions are listed as follows:

1. A detailed analysis of the behavior and characteristics of faulted PMSMs, including simulations and experimental validation. This analysis shows how the fault current is developed and which operating conditions have higher impact on it.

2. A feasible detection and estimation algorithm for turn-to-turn faults based on the voltage space vector information. The method was successfully tested in the detection of several incipient turn-to-turn faults in the early stages; a 0.5 Ω and a 0.25 Ω faults across 15 *turns* out of the total 15 *turns* of the winding. One of the main advantages of this method is that it can be easily implemented in a DSP unit; it requires information of the machine parameters and operation prior to final development. This information comes in the form of lookup tables, a technique that is normally used in high performance controllers.

3. A mitigation algorithm capable of limiting the fault current to a predetermined safe

value, and allow continued operation of the PMSM under reduced capacity. Continuation of the motor operation is dependent upon the severity of the fault.

Analytical, simulation and experimental data were used to test and validate the proposed methodology. Using a 3.8 kW - 25 A fault tolerant PMSM, developed at the MSU Electrical Machines and Drives Laboratory, it was possible to insert faults into the machine to test the proposed algorithm in a safe environment.

1.5 Organization

First, in chapter 2 this work presents the theoretical background and modeling of healthy PMSM. The modeling of healthy PMSMs serves as a base point for the understanding of turn-to-turn faulted motors. Moreover, the models used for faulted motors are derived from the healthy models in chapter 3. The faulty models are detailed and accurate, and are utilized to estimate the amplitude and rms values of the fault current in chapter 5.

Chapter 4 shows the characteristics and parameters of the single layer fault tolerant PMSM designed and assembled in the Electrical Machines and Drives Laboratory at Michigan State University. This motor was used to validate the proposed methodology in chapter 5.

Chapter 5 is the core chapter of this work, as is there that the proposed methodology for detection, estimation and mitigation is presented. It is important to mention that the main contribution is the mitigation of the fault current; the detection and estimation methods were developed in order to test the mitigation. However, they were proven to work as a full fault mitigation system.

Finally in chapter 7 all the conclusion are given.

Chapter 2

Theoretical Background

2.1 Healthy PMSM Analysis and Modeling

This research is focused on three phase PMSMs with wye connected stator windings. A wiring configuration that is widely used in industry and traction drives systems. Commonly the neutral point in these machines is not accessible, only the three phases are available for the control of these machines through current controllers, i_{abc}. The three phase stator windings and the reaction from the rotating rotor magnets in a PMSM are modeled as shown in figure 2.1. In this figure $\hat{e}_{abc}$ represents the magnitude of the the induced sinusoidal EMF voltages and M_{xy} are the mutual inductances between the phases.

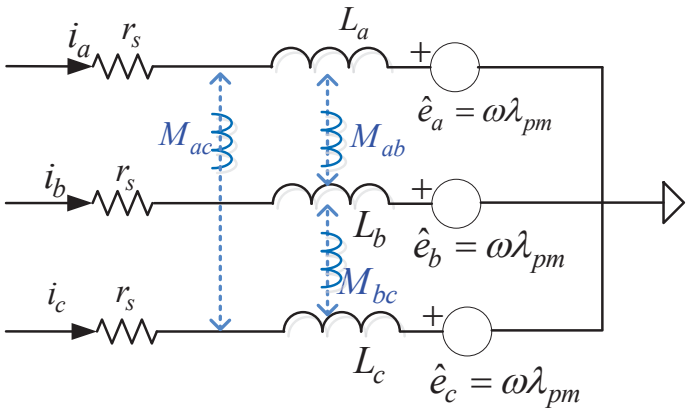

Figure 2.1: Three phase model for a PMSM

For a three phase balanced system, the stator terminal voltages are given as follows,

$$\begin{aligned} v_a &= r_s i_a + L_a \frac{d}{dt} i_a + \omega_e \lambda_a + M_{ab} \frac{d}{dt} i_b + M_{ac} \frac{d}{dt} i_c \\ v_b &= r_s i_b + L_b \frac{d}{dt} i_b + \omega_e \lambda_b + M_{ba} \frac{d}{dt} i_a + M_{bc} \frac{d}{dt} i_c \\ v_c &= r_s i_c + L_c \frac{d}{dt} i_c + \omega_e \lambda_c + M_{ac} \frac{d}{dt} i_a + M_{bc} \frac{d}{dt} i_b \end{aligned} \tag{2.1}$$

The electromagnetic torque produced by the PMSM is calculated using the power into the motor and the rotor speed as shown in 2.2.

$$T_o = \frac{e_a i_a + e_b i_b + e_c i_c}{\omega_m} \tag{2.2}$$

where ω_m is the rotor mechanical angular speed.

The rotor rotation is governed by,

$$J \frac{d\omega_m}{dt} = T_o - T_{load} - k_f \omega_m \tag{2.3}$$

where T_{load} is the load torque, J and k_f are the moment of inertia and friction coefficient respectively.

It is not common or convenient to use the three phase representation of the motor model to calculate terminal quantities, understand the behavior of the machine, and describe its control strategy. A better model representation is obtained by using the Park's transformation matrix in equation 2.4. This matrix transforms the model in equation 2.1 to the rotor frame of reference dq, as shown in equation 2.5.

$$P = \frac{2}{3}\begin{bmatrix} \cos(\theta) & \cos(\theta - \frac{2\pi}{3}) & \cos(\theta + \frac{2\pi}{3}) \\ \sin(\theta) & \sin(\theta - \frac{2\pi}{3}) & \sin(\theta + \frac{2\pi}{3}) \\ 0.5 & 0.5 & 0.5 \end{bmatrix} \tag{2.4}$$

The transformation matrix is invertible and used to transform bidirectionally, from ($abc \rightarrow dq$) and ($dq \rightarrow abc$). To transform from the abc frame of reference to the dq frame of reference the transformation matrix is used as follows,

$$x_{dq0} = P \cdot x_{abc} \tag{2.5}$$

where x is the variable to be transformed.

The dq frame of reference is known as the synchronous frame of reference, where all the electrical quantities are referred to the rotor position. Since PMSMs are synchronous machines, all the electrical quantities in the synchronous frame of reference do not change as in the stator reference; instead, the dq quantities become DC; this simplifies the analysis and control structure of a PMSM.

The angle θ in equation 2.5 is extremely important for the transformation process, since it represents the new frame of reference. For PMSM this angle is the rotor position, which is obtained using a rotor position sensor or estimator. Fig. 2.2 shows the orientation frame to which the transformation is referred. It is a widely common practice to align the rotor position so that the flux linkage produced by the magnets, λ_{pm}, only shows up in the positive d-axis.

Equations 2.6 to 2.9 show the machine model in the dq frame of reference, where the equation set 2.1 was transformed using Park's transformation, with the alignment presented

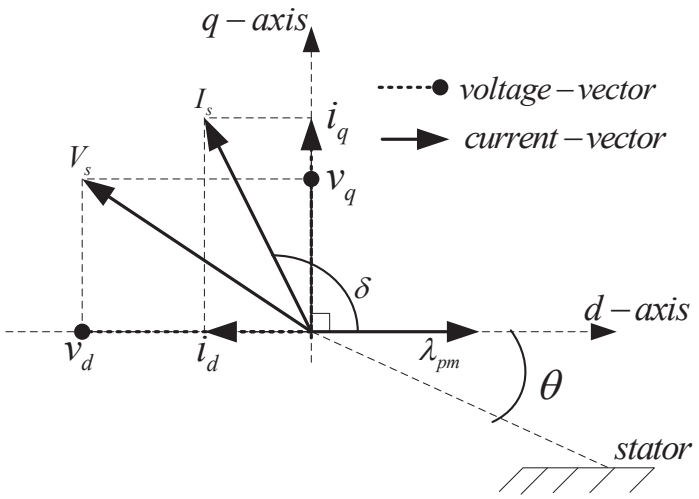

Figure 2.2: Steady State space vector diagram for IPMSM

in figure 2.2.

$$\begin{aligned} v_d &= R_s i_d + L_d \frac{di_d}{dt} - \omega_e L_q i_q \\ &= R_s i_d + \frac{d\lambda_d}{dt} - \omega_e \lambda_q \end{aligned} \tag{2.6}$$

$$\begin{aligned} v_q &= R_s i_q + L_q \frac{di_q}{dt} + \omega_e L_d i_d + \omega_e \lambda_{pm} \\ &= R_s i_q + \frac{d\lambda_q}{dt} + \omega_e \lambda_d \end{aligned} \tag{2.7}$$

$$\lambda_d = L_d i_d + \lambda_{pm} \tag{2.8}$$

$$\lambda_q = L_q i_q \tag{2.9}$$

where λ_d and λ_q represent the flux linkage in each of the axes and λ_{pm} is the flux linkage produced by the rotating magnets.

This mathematical system of equations represents the equivalent circuit model shown in figure 2.3.

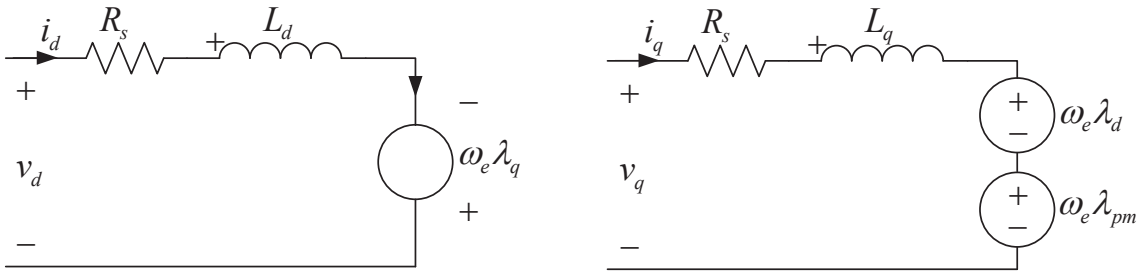

(a) PMSM d-axis equivalent circuit

(b) PMSM q-axis equivalent circuit

Figure 2.3: Equivalent circuit model in the synchronous frame of reference, healthy machine model

The torque in the synchronous frame of reference is given by,

$$T = \frac{3P}{4}\left\{\lambda_d i_q - \lambda_q i_d\right\}. \tag{2.10}$$

This classical model is based on ideal conditions, where the effects of iron losses, self and cross saturation are neglected. Nevertheless, it reveals essential information about the PM motor operation and behavior.

Important remarks about the dq classical model are as follows:

- Torque is produced by the interaction between flux linkages and currents in each of the axes. It is produced by i_q, since it is perpendicular to λ_{pm}, while i_d serves to adjust the amount of flux linkage in de d-axis. Normally in interior PMSMs i_d is negative, and used to optimize the amount of reluctance torque produced by the PMSM. It also allows for field weakening at high speeds.

- Back EMF voltage only shows up in v_q, due to the alignment shown in figure 2.2. This allows the experimental rotor alignment using back emf voltage measurements.

- The i_d can demagnetize the magnets if it is not properly controlled. The flux along

the d-axis is a contribution from the flux generated using i_d and the established flux by the magnets, $\lambda_d^{total} = \lambda_d^{i_d} + \lambda_{pm}$. Having excess of negative i_d can permanently demagnetize the magnets.

2.2 Non-ideal characteristics of PMSM

The classical d- and q- axis model presented in the previous section is useful for understanding the operation principle of the machine. However, from the control point of view, the model lacks the non-ideal characteristics of a machine such as the self and cross saturation effects. These nonlinear effects are not negligible; in fact, they are very common and expected. In order to develop a high performance controller, the knowledge of these effects is essential. Better estimates of the machine inductances can be determined if the level of self and cross saturation is known.

i_d and i_q saturate the iron paths in each corresponding axis. When this happens, the flux linkages produced by the magnetizing currents are not longer decoupled as shown in the ideal model (2.8) and (2.9). Instead, the flux linkages become coupled to both axis currents; this coupling effect can be modeled as follows:

$$\lambda_d\left(i_d, i_q\right) = L_d(i_d)i_d + L_{dq}(i_d, i_q)i_q + \lambda_{pm} \tag{2.11}$$

$$\lambda_q\left(i_d, i_q\right) = L_q(i_q)i_q + L_{qd}(i_d, i_q)i_d \tag{2.12}$$

where $L_d(i_d)$ and $L_q(i_q)$ are the baseline inductances for each of the axes. They represent the corresponding axis self-inductance as a function of the axis current and are calculated assuming no cross saturation from the other-axis current. $L_{dq}\left(i_d, i_q\right)$ and $L_{qd}\left(i_d, i_q\right)$ are

the cross coupling inductances for each of axis and add the cross saturation effects to the machine to the model.

Equations 2.11 and 2.12 could be written in a variety of ways to model the effect of both currents on the d and q axis fluxes. The formulation used here assigns all the cross coupling to the quasi-mutual inductances L_{qd} and L_{dq}, the rest of the saturation to L_d and L_q, and no effect of saturation to the flux due to magnets, without decreasing the model accuracy.

The machine model including the saturation effects is calculated by substituting equations 2.11 and 2.12 into equations 2.6 and 2.7. After simple algebraical manipulation the modified machine model is given by

$$\begin{aligned} v_d = R_s i_d + \left[L_d(i_d)\frac{di_d}{dt} + L_{dq}(i_d, i_q)\frac{di_q}{dt} \right] \\ -\omega_e \left\{ L_q(i_q) i_q + L_{qd}(i_d, i_q) i_d \right\} \end{aligned} \tag{2.13}$$

$$\begin{aligned} v_q = R_s i_q + \left[L_q(i_q)\frac{di_q}{dt} + L_{qd}(i_d, i_q)\frac{di_d}{dt} \right] \\ +\omega_e \left\{ L_d(i_d) i_d + L_{dq} i_q(i_d, i_q) + \lambda_{pm} \right\} \end{aligned} \tag{2.14}$$

$$T = \frac{3P}{4} \left\{ \lambda_d \left(i_d, i_q \right) \cdot i_q - \lambda_q \left(i_d, i_q \right) \cdot i_d \right\}. \tag{2.15}$$

The parameters required to model a PMSM are determined experimentally using a process known as characterization. In this process the terminal voltages, currents and position of the rotor are measured for all operating conditions. All the measured data is used to mathematically solve the models backward and calculate the parameters.

2.3 Experimental Procedure and Characterization

The characterization process is divided in two main procedures, experimental data collection and offline data processing. This section describes step by step the experimental process.

This technique is described and validated in [34], where a simplified characterization method for PM machines was proposed, the simplified method is based on the methods presented on [35, 36]. It has reduced components count, since no AC voltages sensors or analog filters are required to measure the machine line voltages. The components used in this process are, a TMS320F28335 Digital Signal Processor (DSP) with CAN interface, current sensors, a DC link voltage sensor, and a computer to log the data via CAN communication, as it is shown in Fig. 2.4. These are the same components used in a traditional drive system, hence the method is suitable for field, non-laboratory environment.

2.3.1 Line to neutral voltage estimation

The line to neutral voltage of phase A is required for the characterization process. Normally in motor drives the voltages are not measured or used by the control system. Without sensors to measure this quantity, it is accurately estimated using the known information in the DSP unit. Figure 2.4 shows the DSP as the main control unit for the DC-AC inverter that feeds the PM machine. Therefore, the voltage level at which the control unit is operating the inverter is known and it is possible to transmit this information via CAN interface to the data logging computer.

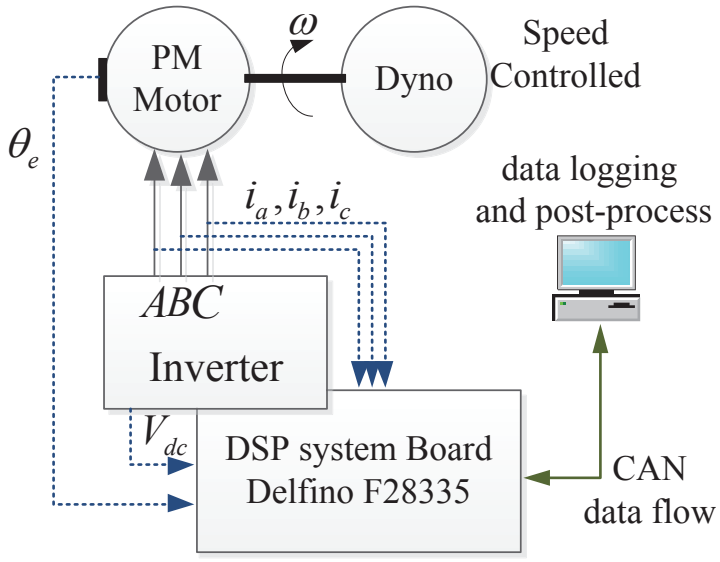

Figure 2.4: Experimental Setup for the characterization process

2.3.2 Rotor Alignment

The estimated line to neutral voltage is used to align the position sensor measurement to the rotor flux axis. A careful alignment must be performed, since the torque capability of the machine is very sensitive to position errors, [36].

The rotor position sensor measurement is properly align to the rotor flux axis using the following steps:

1. Provide sufficient DC voltage to the inverter, in order to be able to match the back EMF of the machine. The DC voltage can be estimated using the machine EMF vs. speed profile to calculate, $V_{dc} > \sqrt{2} v_{emf_{l-l}}^{SVM}$. SVM, stands for Space Vector Modulation.

2. Set the inverter to regulate the machine line currents to zero. Then the dynamometer is used to spin the machine at a constant speed. The speed must be high enough to produce measurable back EMF, but below base speed.

3. Record the electrical rotor position measurement and the estimated back EMF voltage of phase A. If the desired orientation frame of reference is the one described by Fig. 2.2, the zero reading of the electrical rotor position sensor must be aligned with the positive peak of the back EMF voltage, as shown in Fig. 2.5. The rotor magnet flux linkage lags 90^o from the produced back EMF, in vector notation it takes the form $\vec{\lambda}_{pm} = \lambda^d_{pm} + j\lambda^q_{pm}$. λ^d_{pm} takes the value of the magnet flux linkage at an electrical position of 90 degrees, while the λ^q_{pm} is the value at 0 degrees, as indicated in Fig. 2.5. Therefore, $\vec{\lambda}_{pm} = \lambda^d_{pm} + j\lambda^q_{pm} = \lambda^d_{pm} = \lambda_{pm}$ as it is described by Fig. 2.2, where the flux linkage due to the magnets lies positively in the d-axis.

4. Finally, after aligning the rotor, apply only a negative d-axis current to verify that no torque is produced. With the position sensor measurement aligned to the rotor flux axis, only the q-axis current is capable of producing torque. If a significant amount of negative d-current is applied and the machine remains at standstill the alignment is correct. On the other hand, if the machine moves with negative d-axis current, while keeping the q-axis current at zero, the alignment is not correct and the process must be repeated until perfect alignment is achieved.

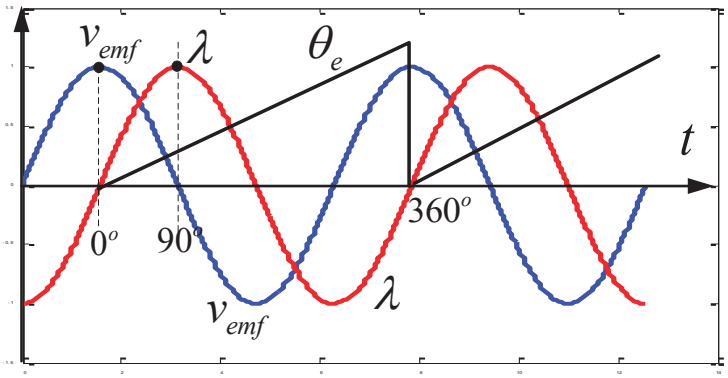

Figure 2.5: Rotor alignment using the electrical position and estimated back EMF

2.3.3 Experimental Data Collection

Accurate estimates of the machine parameters are essential for the development of a high performance motor controller. The estimation process starts by accurately finding the machine flux linkage, $\lambda_d\left(i_d, i_q\right)$ and $\lambda_q\left(i_d, i_q\right)$, considering the saturation effects on the machine.

The necessary information to calculate the flux linkages are v_{an}, i_a, and θ. These three quantities are available in the DSP unit, in the form of feedback and estimation in the case of the phase voltage. The information is used for control purposes, but also it is transmitted to the data logging computer, where the offline computation takes place.

The first step of the experimental process is to use a dynamometer to rotate the PM machine at the desired speed. The speed at which the machine is characterized should be below the rated, but sufficiently high to produce a measurable back EMF. In the case where the core losses are to be considered, the process may be repeated for different speeds.

While keeping the machine rotating at a constant speed the stator current I_s is varied in steps from 0 to $I_s^{\max}$, and for every current step the current-angle δ is varied in steps from 90 to 180 degrees, for reference see Figure 2.2. For every combination of I_s and δ v_{an}, i_a, and θ are recorded.

2.3.4 Post Processing Parameter Extraction

Data post-processing is performed offline after collecting all the required data points. In this work the data processing was carried out using the Matlab software tool.

The corresponding axis quantities, i.e v_d, v_q, i_d and i_q, are determined for every collected data point using the fundamental of the recorded waveform. Figure 2.6 shows an example on how to extract these d- and q-axis quantities from the recorded data, the black square

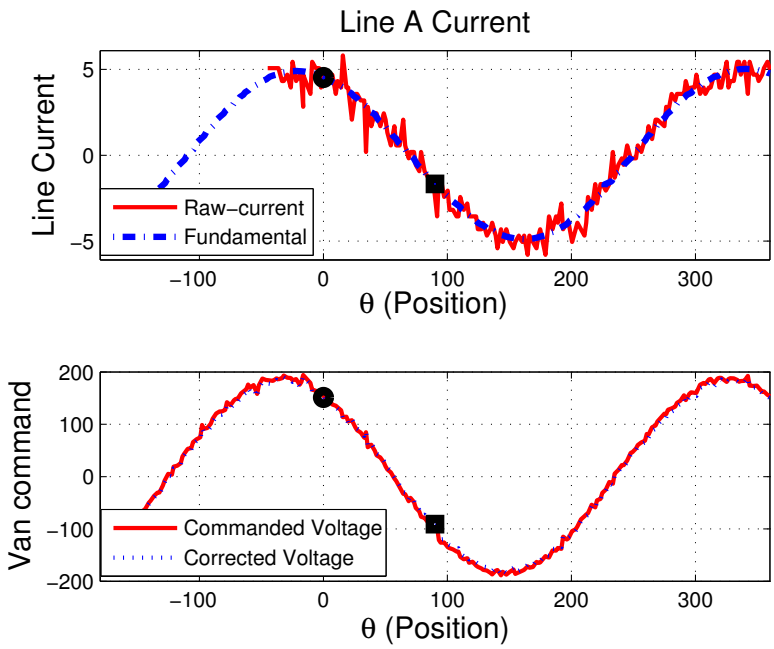

Figure 2.6: Experimental data to determine the d- and q-axis quantities

indicates d-axis values and the black circle indicates the q-axis values. Determining the value of the magnet flux linkage λ_{pm} is important, since it is part of the total flux linkage on the d-axis. It is estimated using the data collected at no current. With no current the inverter has to match the back EMF of the machine, therefore the permanent magnet flux is calculated as follows:

$$\lambda_{pm} = \frac{v_q}{\omega_e} = \frac{\hat{v}_{emf}}{\omega_e}, \quad \omega_e = \frac{d\theta_e}{dt} \tag{2.16}$$

Using the d- and q-axis quantities and the value of λ_{pm} it is possible to calculate the actual flux linkages of the machine. All the collected data points were recorded while operating at steady state conditions and only the fundamental waveforms were used to estimate the d- and q-axis quantities. Therefore, the derivative terms of equations 2.13 and 2.14 are zero. By combining equations 2.11 and 2.12 with equations 2.13 and 2.14 with all the derivatives

set to zero, the flux linkages equations are written as:

$$\lambda_d\left(i_d, i_q\right) = \frac{v_q - i_q R_s}{\omega_e} \tag{2.17}$$

$$\lambda_q\left(i_d, i_q\right) = \frac{i_d R_s - v_d}{\omega_e} \tag{2.18}$$

If the d-axis flux due only to the d-axis current is required, it can be estimated by subtracting λ_{pm} from λ_d, see equation 2.11.

The information extracted up to this point is sufficient to develop a high performance controller, since $\lambda_d\left(i_d, i_q\right)$, $\lambda_q\left(i_d, i_q\right)$ are the actual non-ideal flux linkages of the machine. From them the machine torque can be calculated and lookup tables can be developed. The apparent axis inductances, are estimated using the flux linkages of the machine and the corresponding axis currents as follow:

$$L_d(i_d, i_q) = \frac{\lambda_d(i_d, i_q) - \lambda_{pm}}{i_d} \tag{2.19}$$

$$L_q(i_d, i_q) = \frac{\lambda_q(i_d, i_q)}{i_q} \tag{2.20}$$

Equations 2.19 and 2.20 are estimates of the machine inductances, where the cross coupling terms are neglected. For better accuracy the saturation model, in equations 2.11 and 2.12 is used to represent the flux linkages of the machine. The baseline inductances, $L_d(i_d)$ and $L_q(i_q)$, and the cross-coupling terms, $L_{dq}(i_d, i_q)$ and $L_{qd}(i_d, i_q q)$, are calculated as follows:

$$L_d(i_d) = \frac{\lambda_d(i_d, 0) - \lambda_{pm}}{i_d}, \;\; L_q(i_q) = \frac{\lambda_q(0, i_q)}{i_q} \tag{2.21}$$

$$L_{dq}(i_d, i_q) = \frac{\lambda_d(i_d, 0) - \lambda_d(i_d, i_q)}{i_q} = \frac{\Delta\lambda_d(i_d, i_q)}{i_q} \tag{2.22}$$

$$L_{qd}(i_d, i_q) = \frac{\lambda_q(0, i_q) - \lambda_q(i_d, i_q)}{i_d} = \frac{\Delta\lambda_q(i_d, i_q)}{i_d} \tag{2.23}$$

Using equations 2.21 - 2.23 it is possible to reconstruct the machine non-ideal flux linkages. $L_{dq}(i_d, i_q)$ and $L_{qd}(i_d, i_qq)$ represent the deviations from the baseline inductors as the oppositive axis current is varied.

2.4 Field Oriented Vector Controlled PMSM

A typical controller for PMSM is presented in figure 2.7, the design process for a torque controller is fully covered in [37]. This type of controller is known as the field oriented controller (FOC) for PMSM, where the magnet flux is oriented in the positive direction of the d-axis, as shown in figures 2.2 and 2.8.

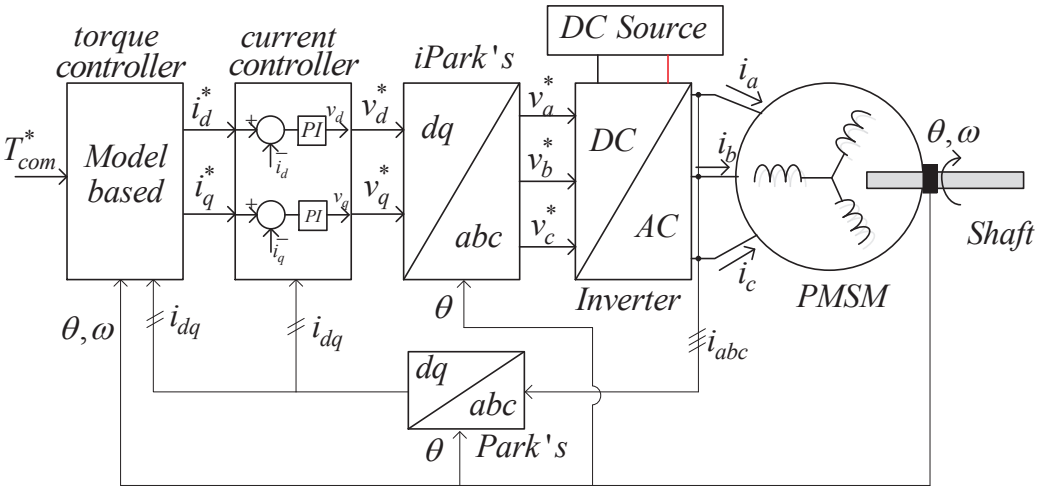

Figure 2.7: Generalized torque controller for a PMSM

The concept is to separately control the the d and q axes currents, i_d and i_q, to achieve the desired torque. These two current components must be properly controlled and coordinated for each operating point. The direct axis current is used to control and adjust the amount of flux linkage on the direct axis and is not capable of producing torque. On the other hand,

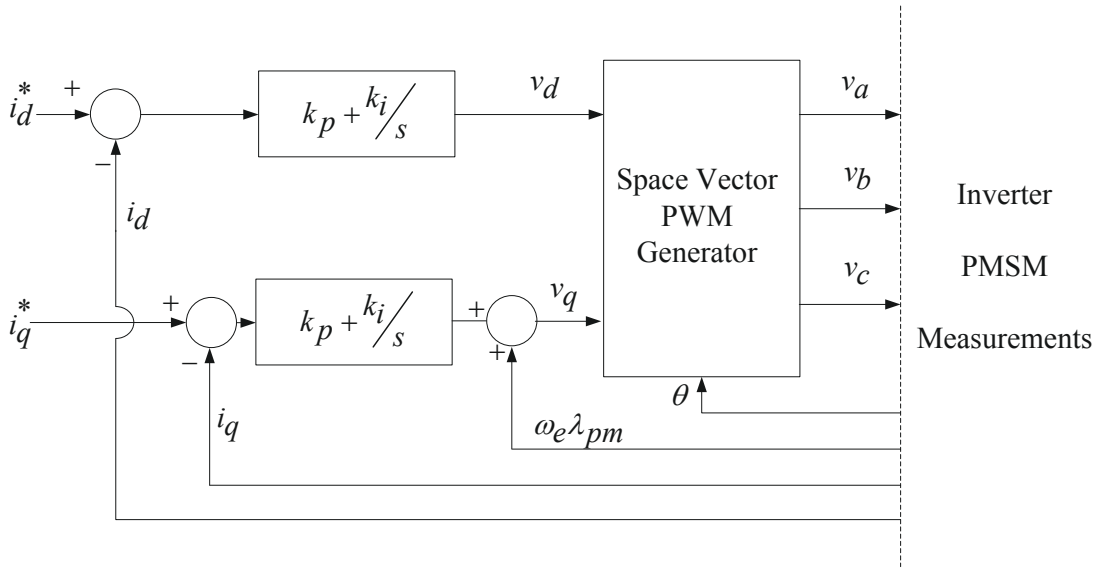

Figure 2.8: Detailed FOC current controller for a PMSM

the quadrature axis current is the main torque producing component. To illustrate the importance of commanding the correct current vector $i_d + ji_q \rightarrow i_s \angle \delta$, the torque equation 2.10 is rewritten as follow,

$$T_e = \frac{3P}{4} \left(\lambda_{pm} \, i_s \sin \delta + \frac{1}{2} \left(L_d - L_q \right) \, {i_s}^2 \sin 2\delta \right). \tag{2.24}$$

Equation 2.24 shows the two torque components in a PMSM. The main torque, produced by the interaction of magnets flux and i_q and the reluctance torque that comes from the difference in the axes inductances and currents. Not all PMSMs have reluctance torque, this torque component is available on interior permanent magnets where $L_d \neq L_q$. Other types of PMSM, like surface mount, are only capable of producing the main torque as their axes inductances are equal, $L_d = L_q$.

As shown in figure 2.9 PMSMs operate in two regions, the constant torque region and

the constant power region. The boundary for each operating mode is the rotor speed, for speed below the nominal it is possible to minimize the current amplitude with respect to the torque without exceeding the maximin ratings of the machine. This region is also known as the Maximum Torque per Amp (MTPA) region; the optimal current angle that results in MTPA is determined using equation 2.24 as $\frac{d}{d\delta}\left(\frac{T_e}{i_s}\right) = 0$. The optimum current angle for the entire MTPA region is determined by equation 2.25. This operating mode is shown in figure 2.10, this mode is the line segment that extends from the origin to point A.

$$\delta_{opt} = \cos^{-1}\left(-\left(\frac{\lambda_{pm}}{4(L_d - L_q)i_s}\right) + \sqrt{\left(\left(\frac{\lambda_{pm}}{4(L_d - L_q)i_s}\right)^2 + \frac{1}{2}\right)}\right) \tag{2.25}$$

Once the motor exceeds the nominal speed it is no longer possible to continue MTPA operation, since the terminal voltage of the machine will exceed its ratings. In this case, the control is switched to field weakening, where the current angle is controlled in order to maintain the PMSM operating at its rated voltage. Controlling this angle controls the amount of i_d current. As shown in figure 2.2, this current opposes the flux linkage from the magnets and it is capable of reducing the amount of flux in the d-axis. Reducing this flux linkage, reduces de amount of voltage in the terminals of the machine.

As shown in figure 2.10 there are two possible field weakening operating modes, mode 1 and mode 2. In mode one the controller applies field weakening so that the resulting voltage magnitude is equal to the machine rated voltage. This operating mode is shown in figure 2.10, and it is depicted by the line segment AB. In this line segment the machine operates under the rating current circuit, $i_s^2 = i_d^2 + i_q^2$, and its only constraint is the lines voltages.

Voltage form an ellipse in the dq operating plane, and this ellipse shrinks as the speed continues to increase. Point B in figure 2.10 shows the point at which the machine current

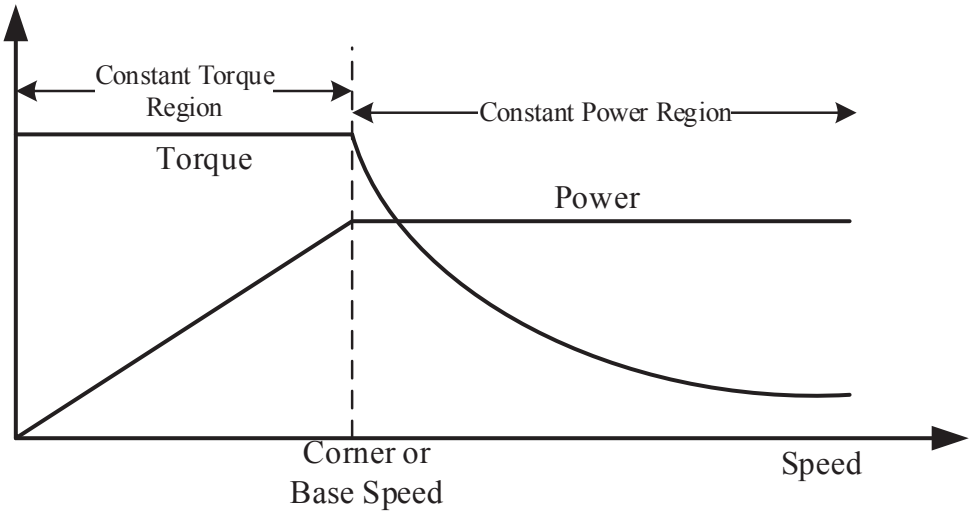

Figure 2.9: PMSM operating regions

rating will be exceeded if the machine speed continues to increase. The behavior of the voltage ellipse is governed by equation 2.26.

$$v_s^2 = \omega_r^2 [\frac{\left(i_d + \frac{\lambda_{pm}}{L_d}\right)^2}{1/L_d} + \frac{\left(i_q + 0\right)^2}{1/L_q}] \tag{2.26}$$

Mode 2 field weakening is not always available, it depends on the machine parameters and design. If point C is outside the current rating circle, then mode 2 is not available. The position of point C depends on the parameters of the machine and it is given by $\frac{\lambda_{pm}}{L_d}$. If point C is inside the current circle, the field weakening mode 2 is achieved by constraining the voltage and current applied to the machine for all conditions in the operating segment BC.

Finally most controllers are developed solving the motor model backwards to find the best combination if i_d and i_q that will result in the desired torque output and speed. Lookup

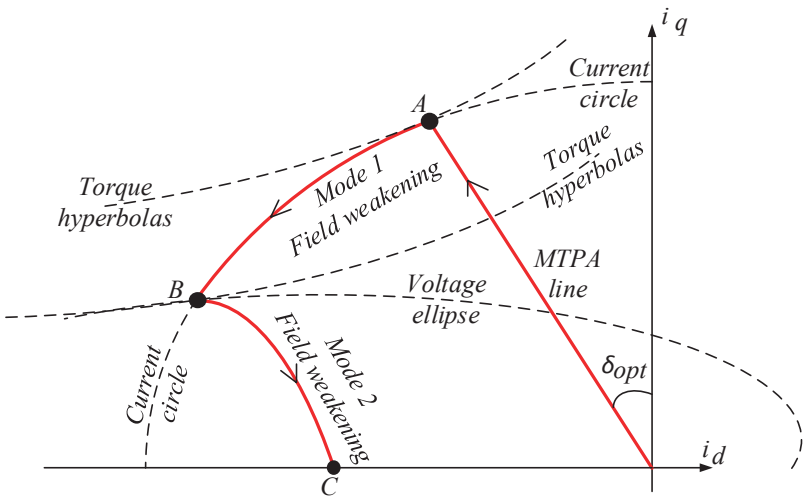

Figure 2.10: PMSM operating path in the dq plane

tables are often used to obtain the commands, given and operating conditions. In [37, 38] the torque and flux linkage information are used to develop develop the tables that follow the behavior shown in figure 2.10. Other authors use model based systems to develop the controllers, as presented on [39], [40] and [41].

2.4.1 High Performance FOC Design for Traction Drives Applications; Including the Saturation And Cross Saturation Effects

In this work high performance controllers were designed for two high power PMSMs, used in a traction drive system [42,43]. The application was a hybrid-electric ground vehicle capable of developing high torque and operate at higher speeds.

Future ground vehicle platforms are expected to generate significantly greater levels of onboard electric power. While traditional alternators can provide approximately 600 A current at 28 VDC (16.8 kW), emerging high-voltage generators directly driven by the engine's crankshaft can produce nearly an order-of-magnitude increase in electric power

$(125 - 160\ kW)$. Benefits of the increased electric power include greater electrification of vehicle loads and intelligent power management, including some of the most significant loads such as the main engine cooling fan(s) and air conditioning compressor. A key challenge remains to ensure that these loads along with the generator operate at maximum efficiency.

The key to improving the performance and efficiency of a motor drive is to develop controllers based on real parameters, [34, 43, 44]. Such controllers are capable of acknowledging the parameters' non-ideal behaviors and using them to operate as efficiently as possible.

In this work, a method to approximate the parameters of a PMSM is proposed. The method is based on experimental data and it includes the saturation effects using piecewise linear functions. The method was validated, in the MTPA and field weakening regions, using simulations based on real parameters from two 125 kW PMSMs.

The effects of iron saturation are covered in section 2.2, a graphical illustration of these effects is given in figure 2.11. Figures 2.7 and 2.8 show the typical configuration for a high performance FOC. It is important to note the relationship between torque and speed to the commands i_d and i_q. For any operating condition (T and ω_m), there exist an optimal combination of (i_d and i_q) that maximizes the efficiency and delivers the required torque.

The determination of all the combinations of i_d and i_q for all operating conditions is performed prior to the development of the final controller. Often developers neglect these effects to simplify the controller design, and eliminate the need of characterizing the PMSM before the development of the controller. This can cause a serious decreases in the performance of the overall system, as the saturation effects in PMSM are considerably noticeable, [45].

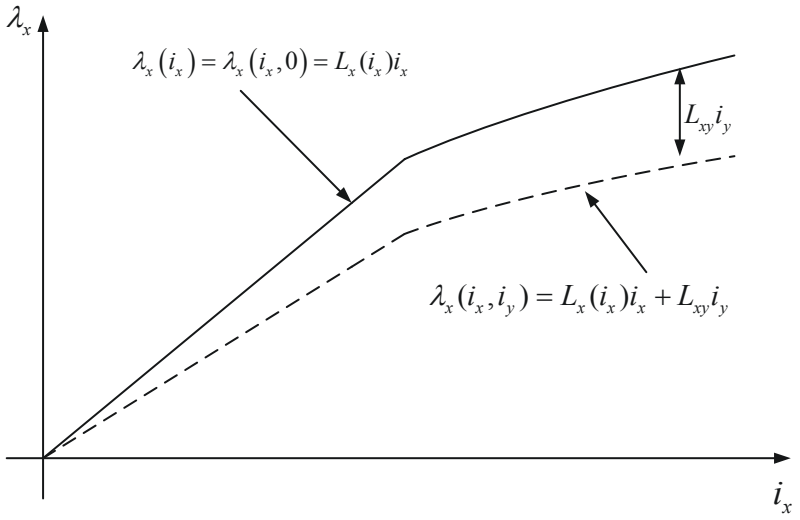

Figure 2.11: Self and cross saturation of the flux linkages

2.4.1.1 Parameters Extraction; To Demonstrate the Saturation Effects

Two PMSMs, a motor and a generator, were characterized in order to study the effects of iron saturation. The characteristics for each machine are given in table 2.1.

Table 2.1: Rated Specifications for the PMSMs

Parameter	Motor	Generator
Rated Power	125 kW	125 kW
Rated Speed	1500 RPM	1900 RPM
Max Speed	5000 RPM	3000 RPM
Line Voltage	480 V_{ll}	480 V_{ll}
Number of Poles	4	8

The parameters for both machines were determined at 700 RPM using the characterization technique presented in section 2.3. This speed is sufficient to generate a measurable back-EMF voltage and it is below the base speed. Therefore, it is possible to collect experimental data for all the combinations of i_d and i_q up to rated current.

The experimental results for the characterization process are shown in figures 2.12 to 2.15.

They demonstrate that self and cross-saturation are non-ideal characteristics and cannot be ignored or assumed to be negligible. For the motor, the flux linkage along the d-axis had as much as 38.5 % variation due to cross saturation, while along the q-axis it had as much as 23.7 % variation.

The generator behavior is similar, with flux variations as high as 31.4 % on the d-axis flux and 14.5 % on the q-axis due to cross saturation. These non-ideal parametric variations have a negative impact on the torque production of the machine, since the torque is directly proportional to the flux linkages, as shown in equation 2.15. Efficiency is also affected, as the parametric variations will de-tune the motor controller. For a given operating condition, the de-tuned controller will not inject the optimal currents to generate the desired torque. This is because the saturation effects decrease the amount of flux linkages the machine can produce and the de-tuned controller has to compensate the torque mismatch by increasing the magnitude of the q-axis current. Resulting in a non-optimal i_d and i_q commands to produce the desired torque.

2.4.1.2 Proposed Parameter Approximation

In order to develop a high performance controller, accurate knowledge of the parameters is required across the entire operating range. Look Up Tables (LUTs) are commonly used to develop controllers based on real parameters. By using a controller based on a LUT, it is possible to fully include the non-ideal parameter behavior shown in figures 2.12 to 2.15 in the PMSM controller.

The main drawback of a LUT is the required memory in the controller. The memory space requirement is directly proportional to the resolution of the LUT, [43]. In many applications, Digital Signal Processors (DSPs) are used to implement the controller. These DSPs are

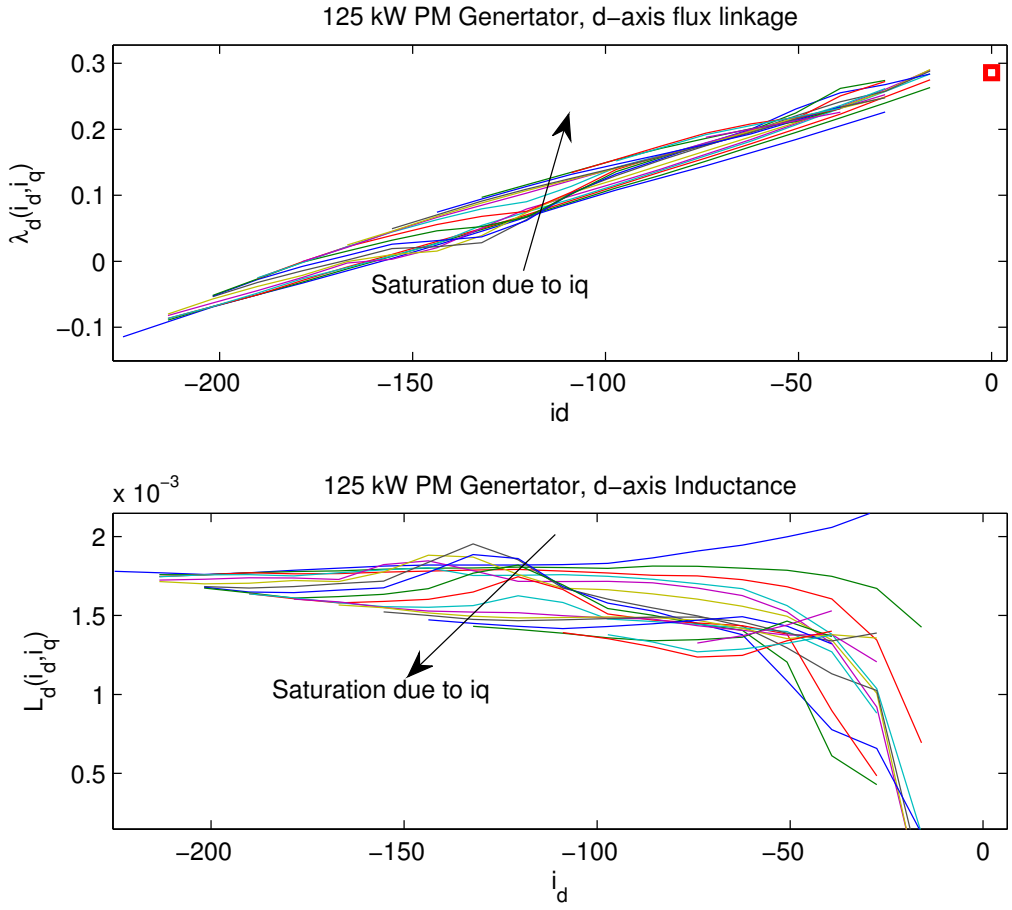

Figure 2.12: Generator experimentally extracted d-axis flux linkage and d-axis inductance. The Arrow points at the direction which i_q is increased.

commercially fabricated with a limited memory capacity. A LUT can be implemented in a DSP controller; however, the LUT resolution must be reduced to fit it in the available memory. This can lead to a decrease in performance of the controller, as information is removed from the table's entries.

An accurate curve-fit method to approximate the real parameters of the motor and generator is proposed in this section. The method is a dynamic piecewise linear approximation that includes the parameters' non-ideal characteristics, i.e., the cross-saturation effect. It can perform as well as a full parametric LUT controller, but it will not overstress

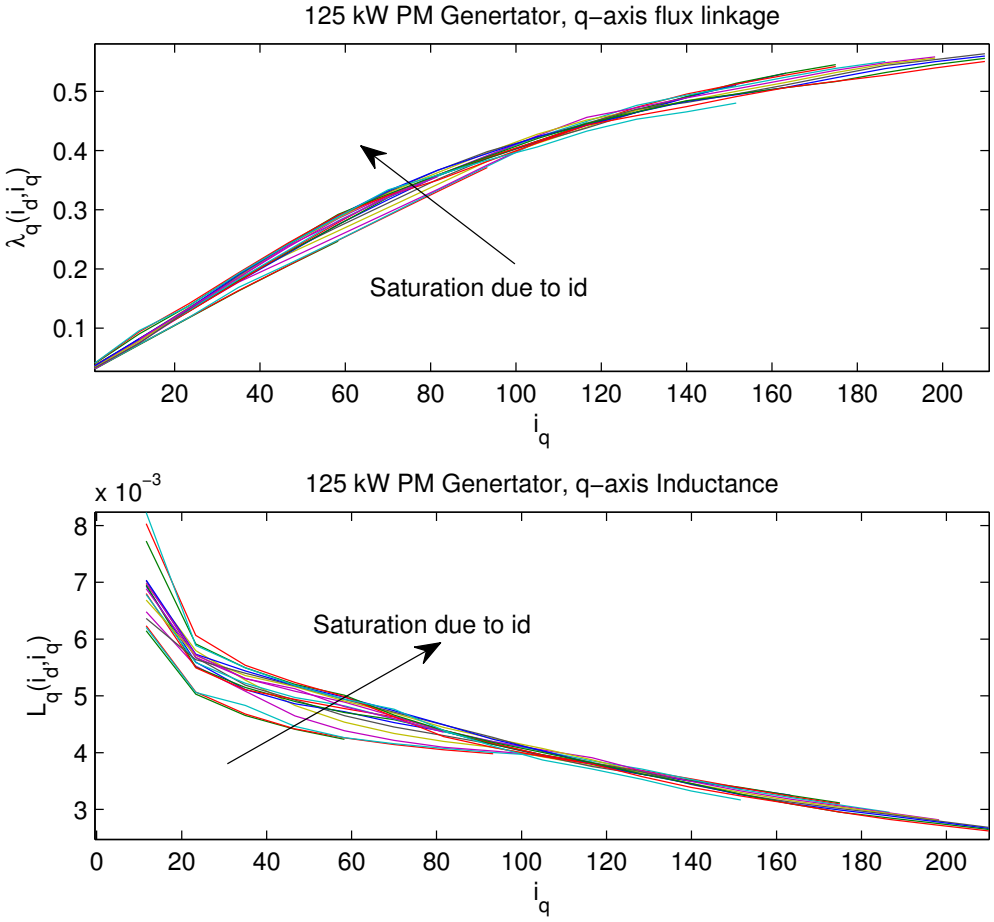

Figure 2.13: Generator experimentally extracted q-axis flux linkage and q-axis inductance.The Arrow points at the direction which i_d is increased.

the DSP/microcontroller memory, nor consume much computation time. For the case of $L_d(i_d, i_q)$, the true inductance, shown in figures 2.12 to 2.14, is divided into two linear sectors, as shown in figure 2.16. The first step is to determine the baseline d-axis inductance from the experimental data, given by 2.27.

$$L_d(i_d, i_q)\Big|_{i_q = 0} = L_d(i_d, 0) \tag{2.27}$$

The two linear approximations for 2.27 are highlighted in figure 2.16 by the line with stars

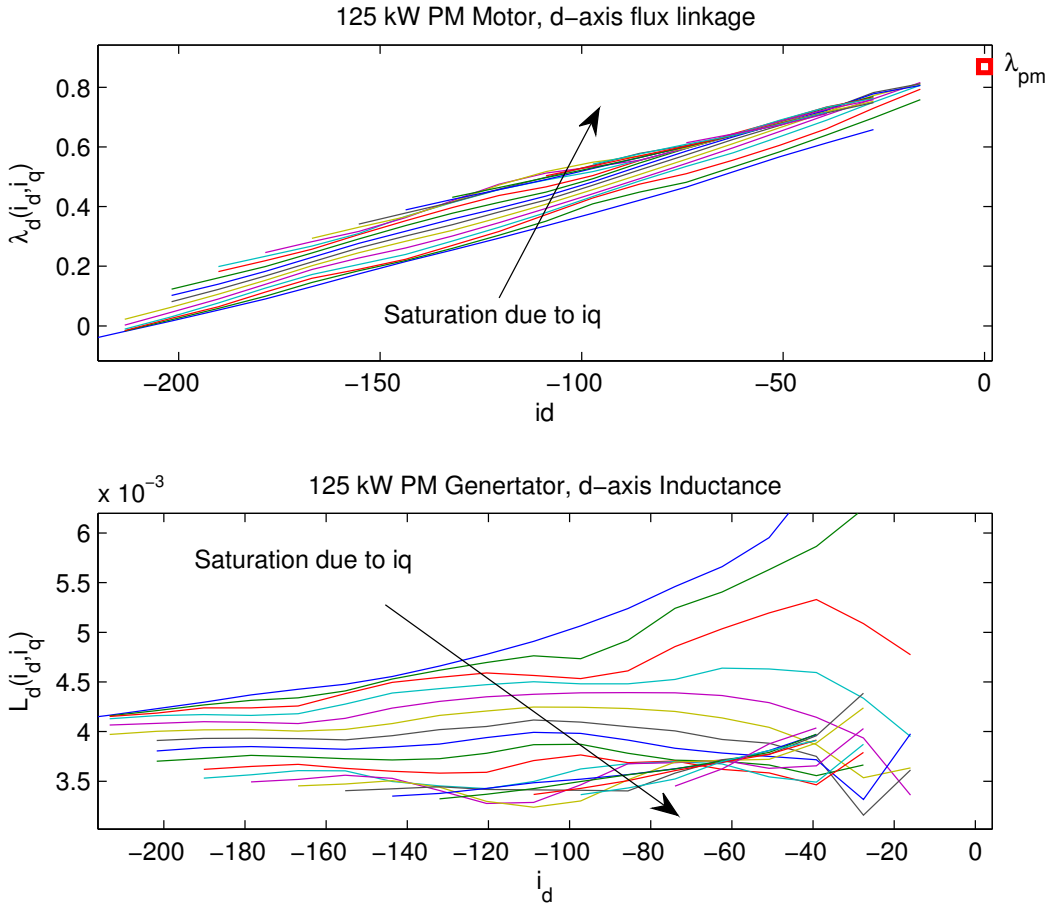

Figure 2.14: Motor experimentally extracted d-axis flux linkage and d-axis inductance. The Arrow points at the direction which i_q is increased.

markers. Finally, the cross saturation for this case is added by subtracting from this baseline approximation, as the other axis current increases. It is assumed that cross-saturation in the d-axis increases linearly with the q-axis current. The incremental function is defined as $\Lambda(i_q)$. By using the experimental data and inspection, it is determined that the function representing the cross-saturation terms is as shown in equation 2.28. Finally, the total inductance in these two sectors is given by equation 2.29.

$$\Lambda_d^{\text{sec }1\&2}(i_q) = \frac{-\Delta_L(i_q)}{i_{rated}} i_q \tag{2.28}$$

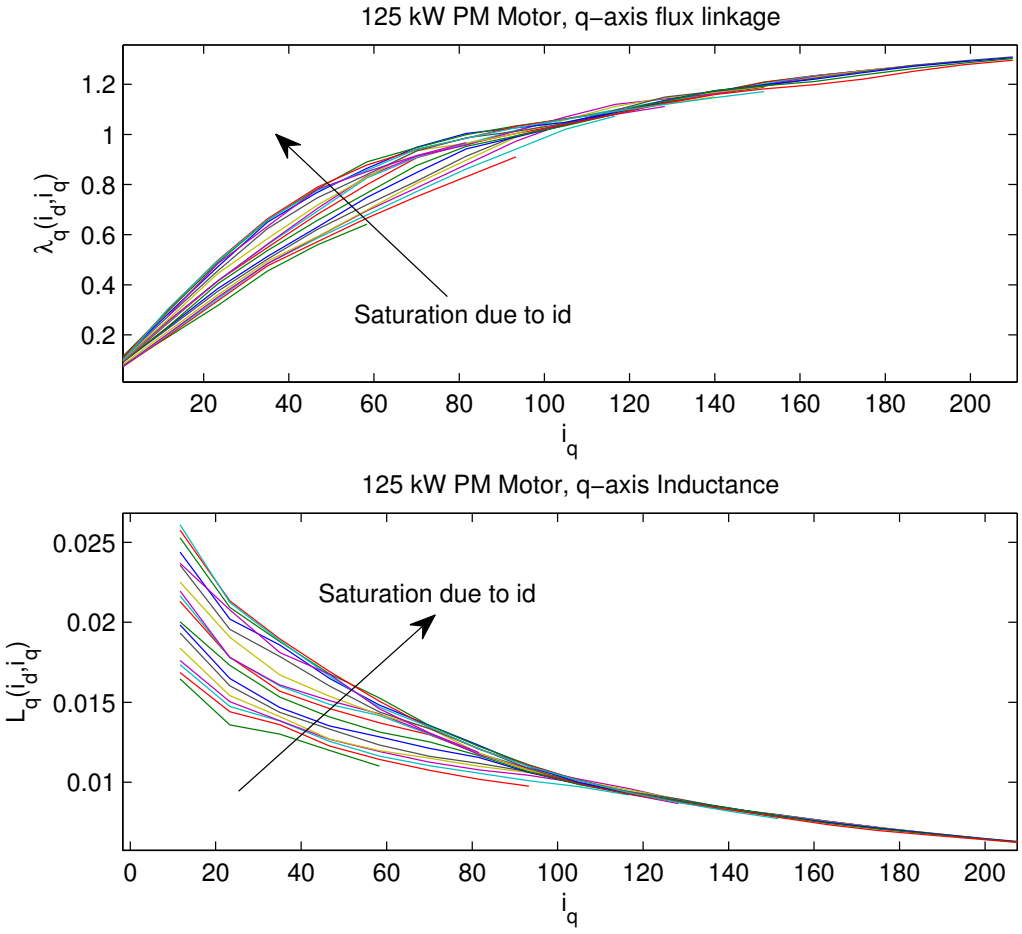

Figure 2.15: Motor experimentally extracted q-axis flux linkage and q-axis inductance. The Arrow points at the direction which i_d is increased.

$$L_d(i_d, i_q) = L_d(i_d) + \Lambda_d^{\text{sec }1\&2}(i_q) \tag{2.29}$$

In figure 2.16, the two sector linear approximations and the true experimental inductances are plotted together to illustrated the approximation accuracy. The dashed straight line segments are the linear approximation, while actual parameters are represented by the solid lines.

The q-axis inductance requires more linear sectors, as shown in figures 2.13 to 2.15, since it suffers higher saturation than the d-axis quantities. Instead of two sector to approximate

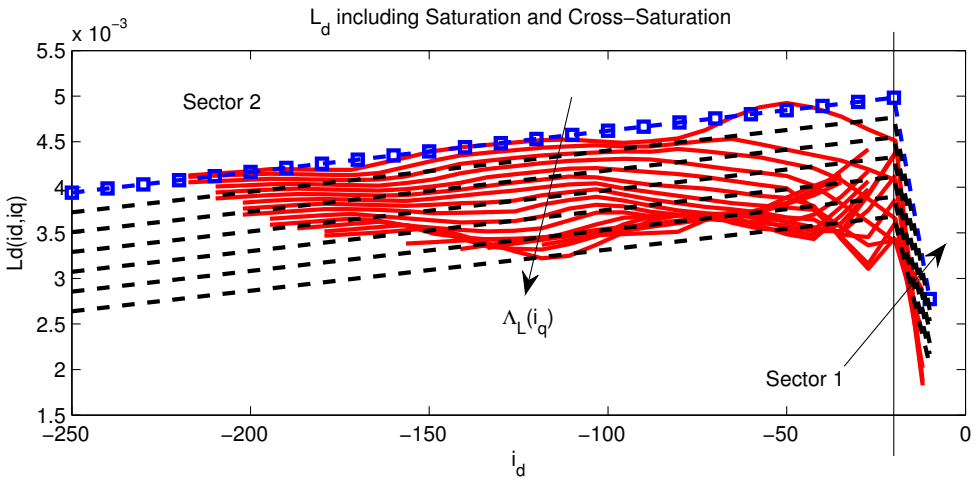

Figure 2.16: Motor d-axis inductance piecewise linear approximation, including cross saturation.

this inductance, four sectors are used as shown in figure 2.17.

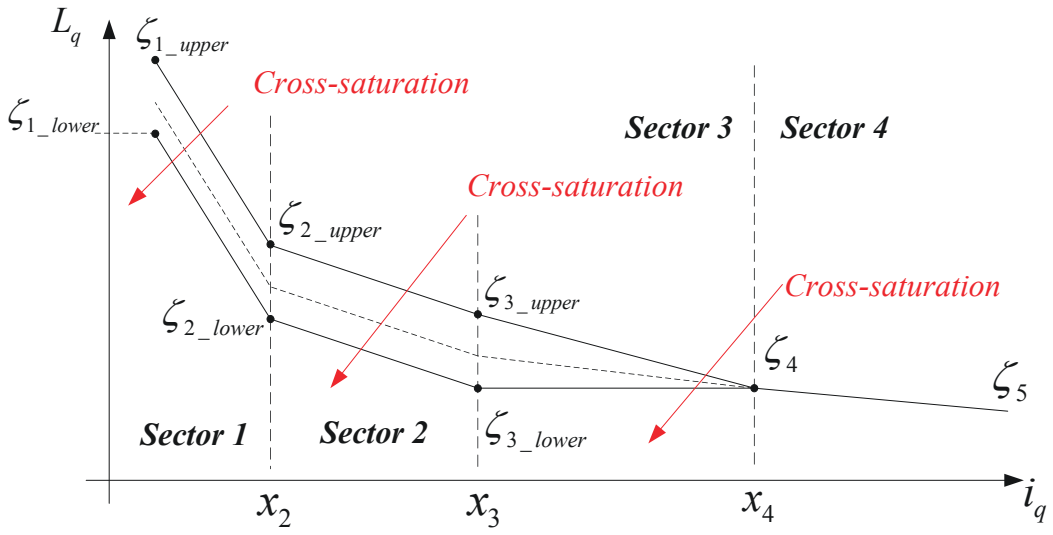

Figure 2.17: q-axis inductance piecewise linear approximation, including cross saturation in four sectors.

The linear approximations made in each sector are discussed from right to left, beginning with sector 4. As shown in figures 2.13 to 2.15, the effect from the d-axis current is minimal

in this segment. Therefore, the inductance approximation is made by finding the equation of the line that passes through points ζ_4 and ζ_5 as shown in figure 2.17.

In sector 3, the cross-saturation effects are added by introducing a slope change to the base line inductance $L_q(0, i_q)$. In this sector, ζ_4 is a fixed point, but the slope of the baseline inductance is adjusted as a linear function of i_d as shown in equation 2.30, and the cross-saturation is added using $\Lambda_d^{sector3}(i_d)$ in equation 2.31. The expression to determine the approximated q-axis inductance in sector 3 is given by equation 2.32.

$$m(i_d) = \frac{\zeta_{3\_lower} - \zeta_{3\_upper}}{i_{d\_rated} \cdot (x_4 - x_3)} \cdot i_d + \frac{\zeta_4 - \zeta_{3\_upper}}{x_4 - x_3} \tag{2.30}$$

$$\Lambda_d^{sector3}(i_d) = \frac{\zeta_{3\_upper} - \zeta_{3\_lower}}{i_{rated}} \cdot i_d + \zeta_{3\_upper} \tag{2.31}$$

$$L_q(i_d, i_q)\Big|_{sector3} = m(i_d) \cdot (i_q - x_3) + \Lambda_d^{sector3}(i_d) \tag{2.32}$$

In sectors 2 and 1, the linear approximation is made using the same technique used for the d-axis inductance in equation 2.29; where the slope is constant and the cross-saturation is modeled by the linear function $\Lambda_q^{sector2\&1}(i_d)$. Note that all values of ζ are known from the experimental data. The complete approximation for the motor q-axis inductance along with the true experimental values are shown in figure 2.18.

The inductance approximations for the generator were determined using the same technique and the results are similar to those of the motor.

2.4.1.3 Controller Performance Evaluation

To evaluate the accuracy of the proposed parameter approximation method, a performance simulation based on experimental data was developed for each PMSM, as shown in figure

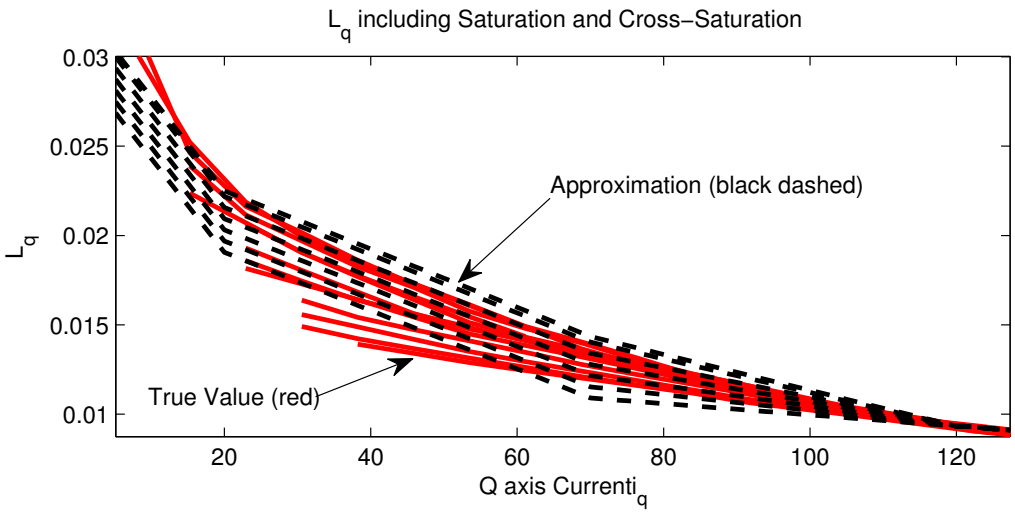

Figure 2.18: Motor q-axis inductance piecewise linear approximation on top of the experimental q-axis inductance.

2.19. The simulation was performed with four different controllers; one using a highly detailed parametric LUT including the saturation effects, one LUT without the saturation effects, one using parameters determined using FEA magneto static analysis and finally one with the proposed approximation method. For this study, only the copper losses were considered. This leads to high efficiency results, but it serves as a proof of concept.

First, a highly detailed controller was developed using a LUT. This controller contains all the saturation effects of the motor. Therefore, this controller is used as the baseline. The tables' resolution has steps of 2.5 A from zero to 250 A. For each current step there is a table entry that matches a torque command and a speed to a set of i_d and i_q. The second controller was developed using experimental data, but the cross-saturation effects were ignored. For this case the table's resolution is the same as the first case. The third controller was developed using the proposed parameter approximation method. Finally, a controller based on parameters from FEA was developed to compare with the experimental parameters based controllers. The controllers developed using the proposed and FEA parameters are based on curve fit methods, not LUT.

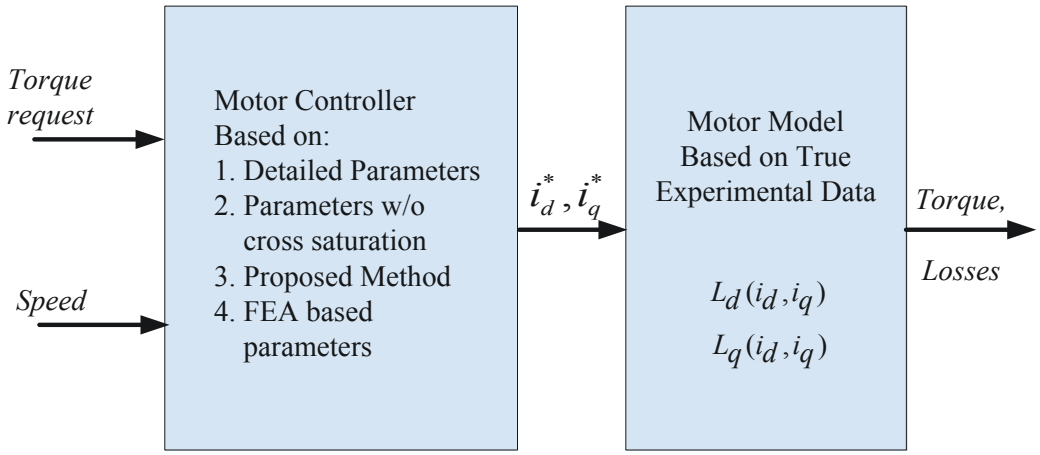

Figure 2.19: Simulation based performance evaluation, using the PMSM experimental parametric data.

Each controller was tested in the MTPA and field-weakening regions. For each region, the torque command was varied from 200 Nm to maximum, and the copper power losses and torque for each operating point were calculated. The results for the performance simulation are shown in figures 2.20 to 2.23.

Figures 2.20 and 2.21 show the performance simulation for the generator. For both operating regions, the controller that performed almost as well as the baseline, the high resolution LUT controller, was the controller designed with the proposed parameter approximation method. This statement is based on the lower power losses and the torque tracking effectiveness.

Figure 2.20 shows that minimum power losses were achieved with the base line controller and the controller using the proposed parameters approximation technique. On the other hand, the controllers designed using FEA parameters and the parameters ignoring cross-saturation are the controllers that yielded the highest power losses. Similar behavior was

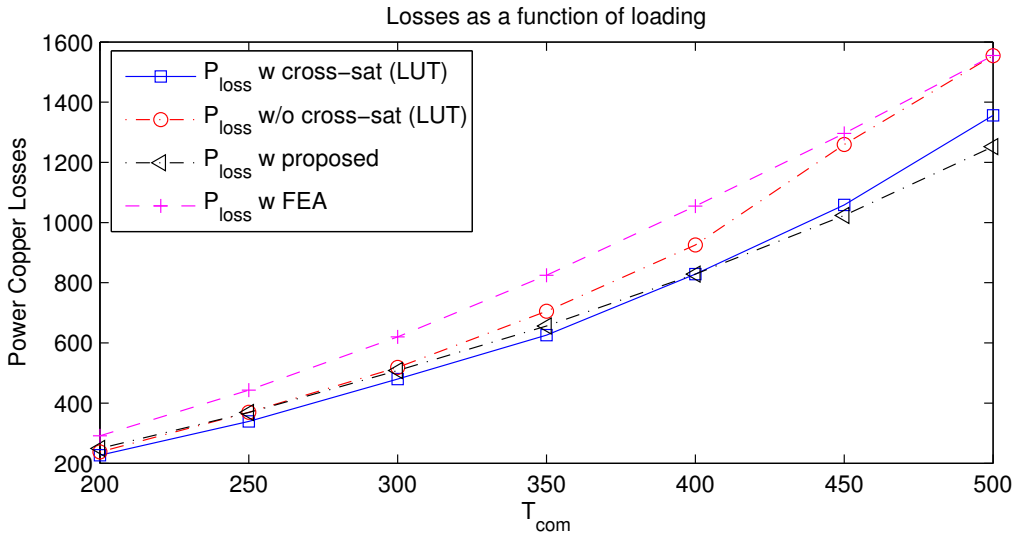

(a) Generator power losses at nominal conditions

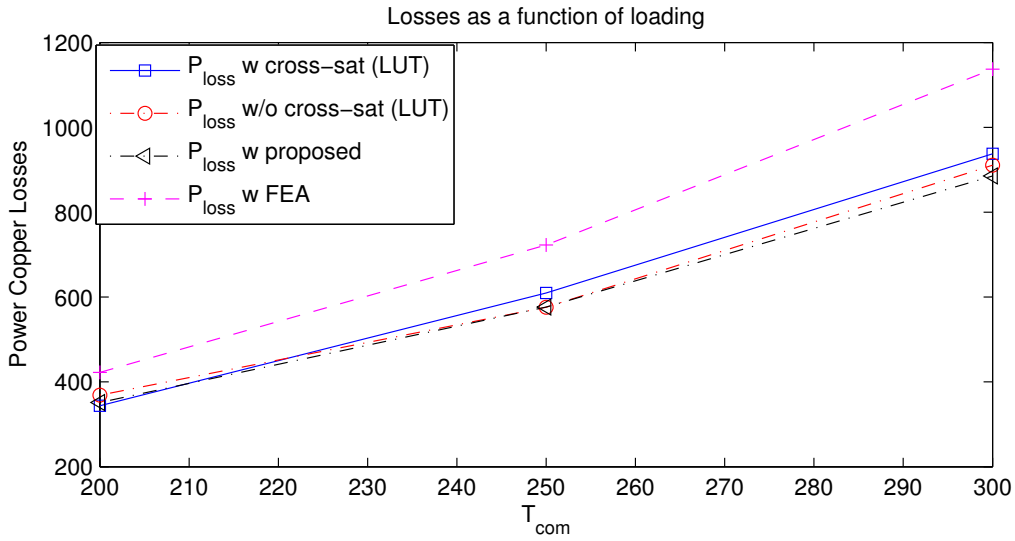

(b) Generator power losses at 3000RPM, field weakening region

Figure 2.20: Generator P_{losses} in MTPA and field weakening mode, only considering copper losses.

noted for the torque performance shown in figure 2.21 where the controller designed using the proposed parameters follows the detailed LUT controller torque performance.

The motor exhibited similar behavior as shown in figures 2.22 and 2.23. However, power losses are higher for the motor, this is because it has a higher line resistance and is more prompt to higher cross-saturation than the generator. The motor has higher cross-saturation

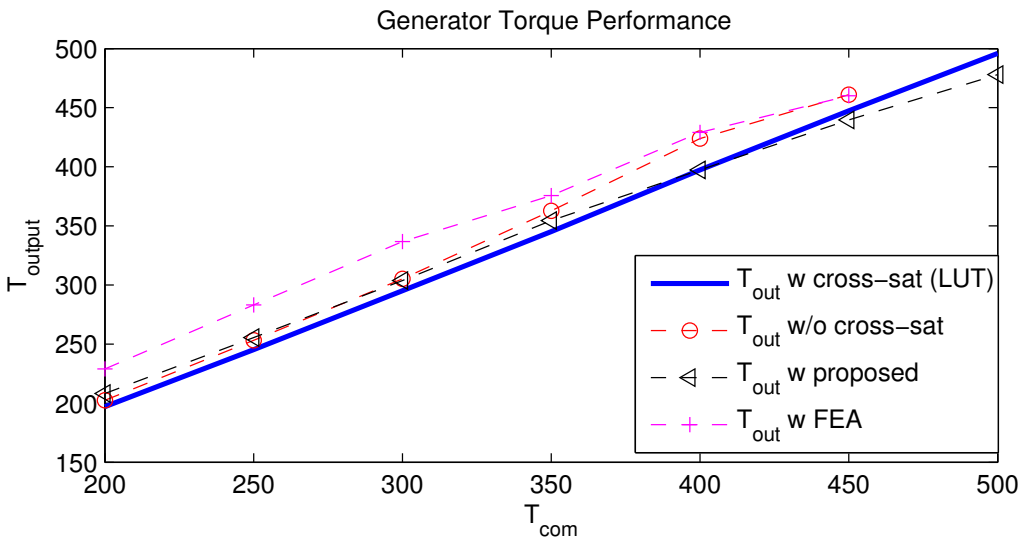

(a) Output torque vs. commanded torque profile in the MTPA region

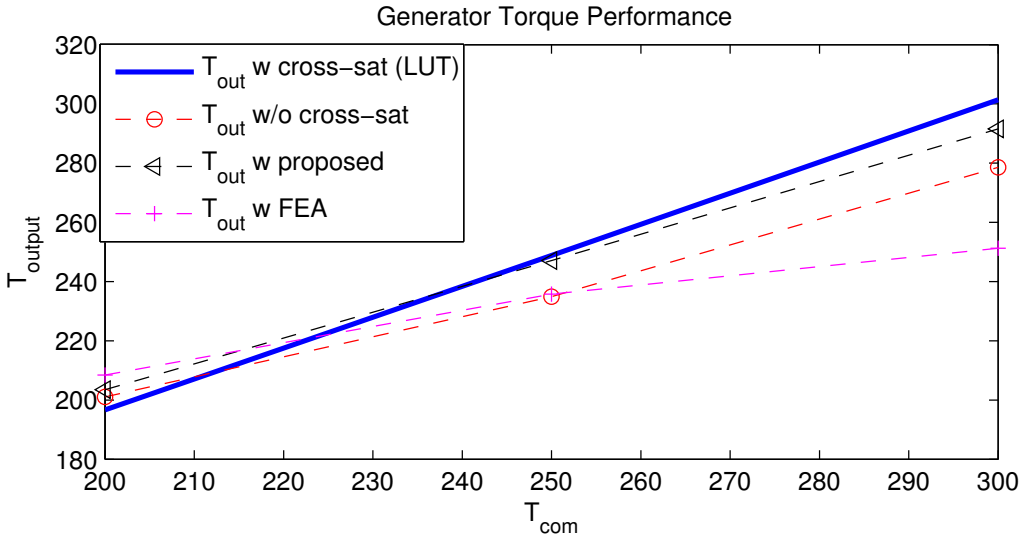

(b) Output torque vs. commanded torque profile in the field weakening region, 3000 RPM.

Figure 2.21: Generator T_{out} mismatch with the commanded torque T_{com}.

due to the intensity of the magnets flux linkage (λ_{pm}), which is much higher in the motor than in the generator. The intense flux linkage saturates the iron and makes the machine prompt to suffer cross-saturation. For the motor, the controller designed using the proposed parameter approximation method had the closest performance to the detailed LUT controller.

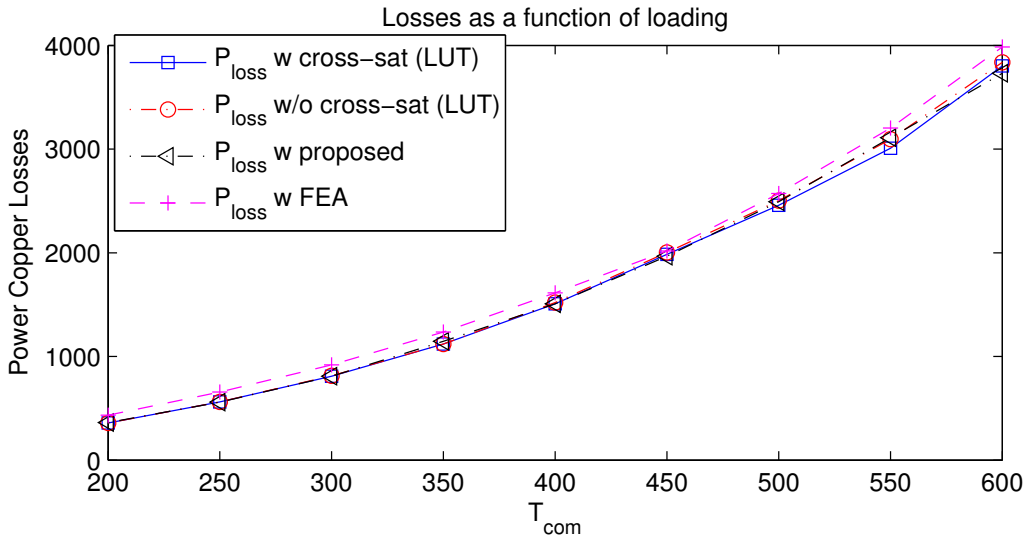

(a) Motor power losses at nominal conditions

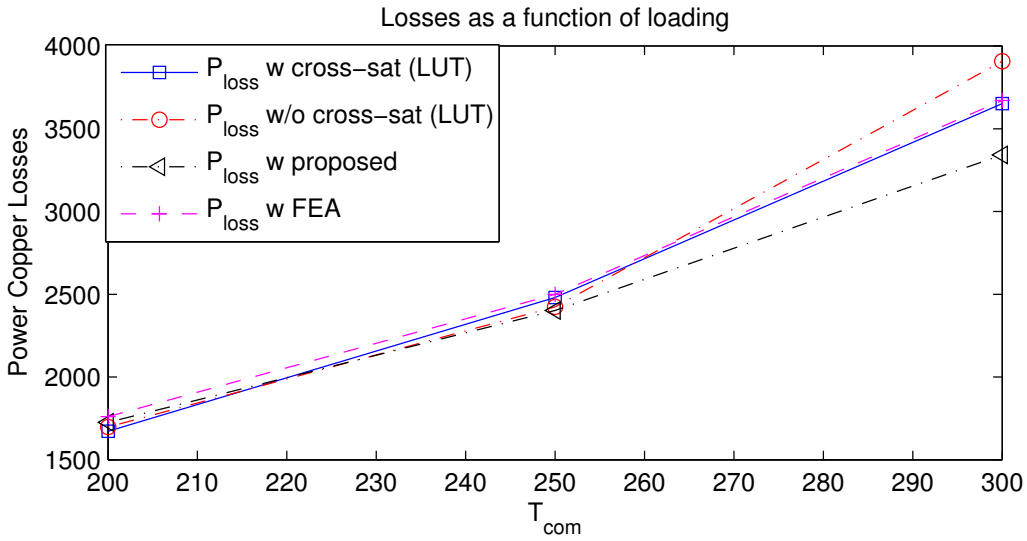

(b) Motor power losses at 3000RPM, field weakening region

Figure 2.22: Motor P_{losses} in MTPA and field weakening mode, only considering copper losses.

2.4.1.4 Remarks

In this section, the effects of iron saturation on the performance of a motor drive are studied using two PMSMs. The flux linkages and inductances of each machine were determined through a characterization process and are shown in figures 2.12 to 2.15. Saturation is evident from these figures and cannot be ignored or assumed negligible.

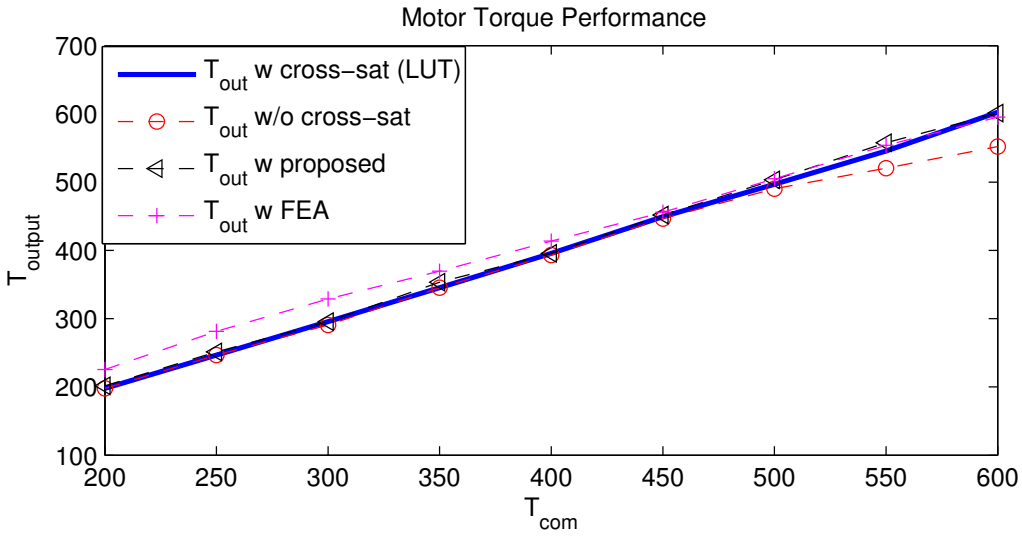

(a) Output torque vs. commanded torque profile in the MTPA region.

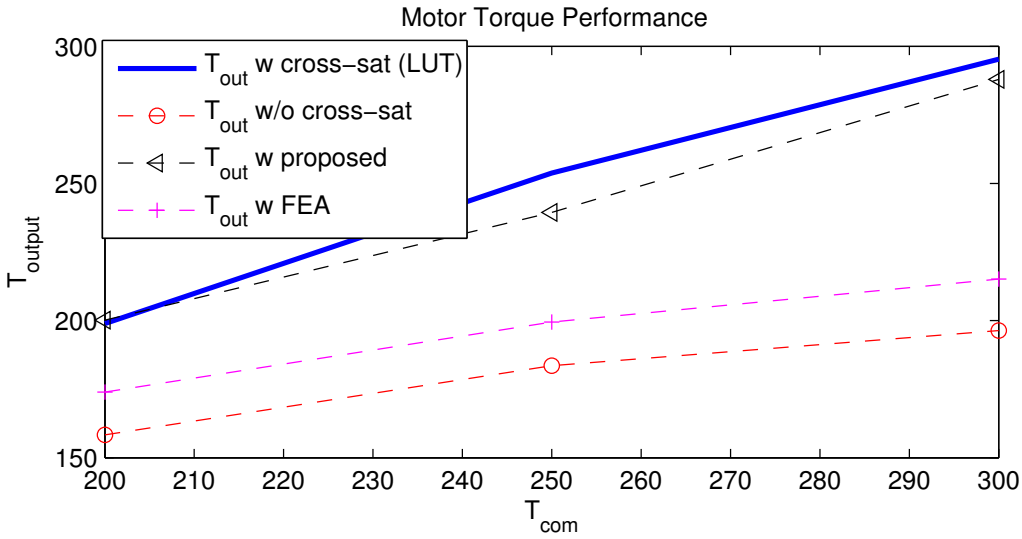

(b) Output torque vs. commanded torque profile in the field weakening region, 3000 RPM.

Figure 2.23: Generator T_{out} mismatch with the commanded torque T_{com}.

It is possible to obtain the parameters required to design a motor controller through FEA simulations or experimental data collection. The inclusion of cross-saturation effects in the controller development is vital to ensure a high performance, high efficiency controller.

A method to include these effects is proposed. It was tested against controllers based on high resolution LUT, LUT without cross-saturation, and FEA parameters. Figures 2.20 and 2.21 demonstrate the validity of the method. The simulations showed that the proposed

method results in low losses and good torque performance; both metrics are comparable to the performance of the high resolution LUT controller at both MTPA and field weakening regions.

Compared with conventional approaches, the proposed method applied to a 125 kW machine contributed to a reduction in copper losses as high as 900 W, resulting in an efficiency gain of 1.36%. The proposed controller, incorporating a dynamic piecewise linear approximation of the machine flux linkages, is realizable in the majority of motor control DSPs used in high performance PMSM controllers due to its computational efficiency. This efficiency also reflects on the memory utilization in the DSP unit, figure 2.24 the memory utilization for various control techniques. The controller helps to improve the dynamic response of the drive and its improved efficiency contributes to a decreased thermal burden on the cooling system in vehicle applications.

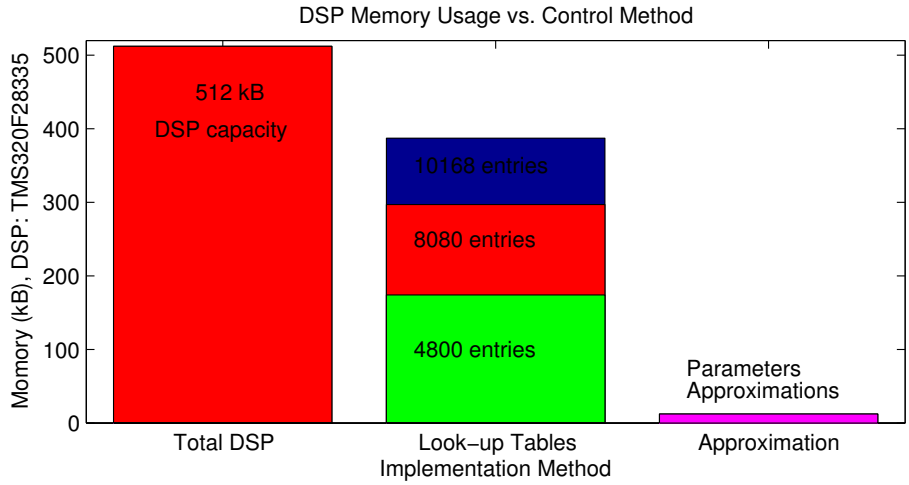

Figure 2.24: DSP memory utilization based on the control method, including look-up table resolution.

Chapter 3

Modeling of Permanent Magnet Synchronous Motors under a Turn-to-Turn Fault

Modeling is an essential tool to understand the behavior of PMSMs and develop new techniques for PMSMs. It enables researchers to study operational characteristics and come up with control techniques before trying them in a real system. This chapter develops a faulty machine modeled to predict the behavior of a faulted PMSM and design a controller capable of mitigating the fault.

Modeling is an important part of fault mitigation systems. Faulted PMSMs models are derived from the healthy operational characteristics and models. There are two types of models, FEA parameters based and analytically derived. The first one, consist in calculating all the machines parameters using FEA, including the parameters of the faulted winding and the remaining healthy windings. While in the second modeling method, the faulted parameters are estimated from the healthy parameters. These models are similar for detection, control and characterization techniques, [3, 20, 46, 47].

3.1 Winding and Fault Severity

A turn-to-turn fault is modeled by splitting a portion of a healthy phase coil into two separate coils, denoted as a_h for the healthy part and a_f for the faulted area. The number of turns involved in the fault is denoted as N_f and the total number of turns per phase is N_{total}. The schematic representation for a faulted machine is shown in figure 3.1.

A fault resistor, r_f, is included in the model to take into account the severity of the damaged winding. A turn-to-turn fault starts with low severity, $r_f \to \infty$, and as the winding insulation continues to deteriorate it has the potential to become a highly severe fault or short circuit, where $r_f \to 0$, [12]. Winding insulation deterioration is due to many possible reasons, among these possibilities are: high voltage spikes from the DC link and PWM phase voltages, aging, overheating and mechanical stress.

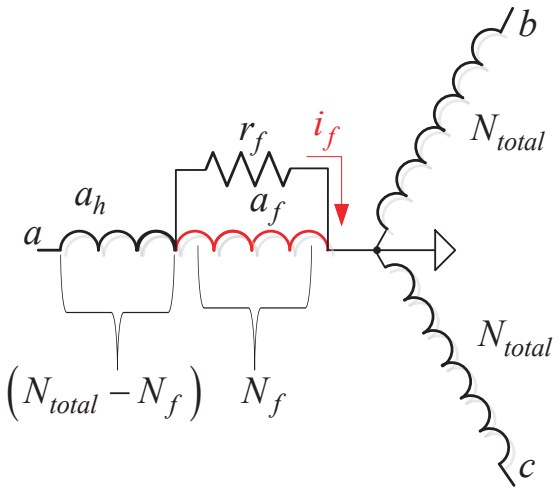

Figure 3.1: PMSM with a turn-to-turn fault on phase A

Once a fault is developed, a circuit path is created through r_f. This circuit allows the fault current, i_f, to flow, and it puts in danger the integrity of the whole PMSM. This dissertation shows that this current has the potential to grow as high as or even higher than

the current ratings of the winding. Therefore, a method to detect and correct is required in applications where lives could be in danger.

For researchers, the term fault mitigation means to completely extinguish the fault current, i_f. In this work the mitigation technique is aimed to gain a degree of control over the fault current, not necessarily achieve complete suppression of it.

3.2 Detailed Modeling of turn-to-turn Faults

A turn-to-turn fault affects the electrical quantities in the phase it resides. It directly reduces the flux that links the coil, the voltage and increases the line current. This presents challenges in the control, as the system is no longer three phase balanced. This type of fault is modeled with the electrical circuit shown in figure 3.2 and has been adopted and validated by others; [19], [24], [21].

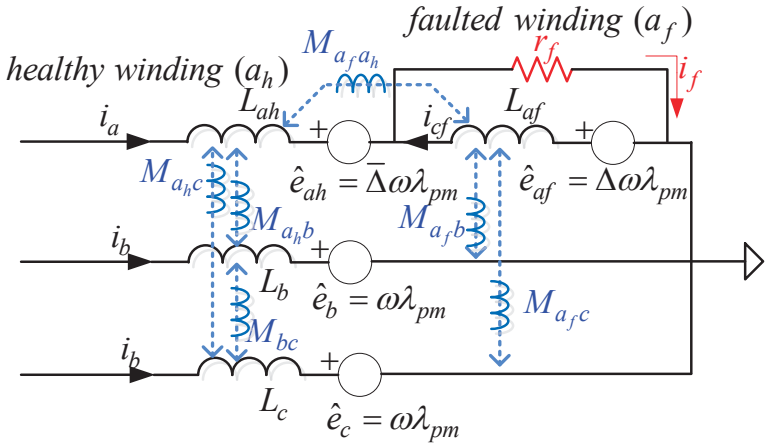

Figure 3.2: Three phase electrical model for a faulted PMSM

Each coil is modeled using its own resistance, self and mutual inductances and its induced back EMF. The induced voltage across r_f depends on the number of turns involved in the

fault, and is estimated using the ratio (Δ) between N_f and N_{total}.

$$\Delta = \frac{N_f}{N_{total}} \tag{3.1}$$

$$\bar{\Delta} = \frac{N_{total} - N_f}{N_{total}} = (1 - \Delta) \tag{3.2}$$

The mathematical expressions for the faulted machine shown in figure 3.2 are determined using circuit analysis techniques. This mathematical model is shown in the system of equations 3.3.

$$\begin{bmatrix} v_{ah} \\ v_{af} \\ v_b \\ v_c \end{bmatrix} = \begin{bmatrix} r_{ah} & 0 & 0 & 0 \\ 0 & r_{af} & 0 & 0 \\ 0 & 0 & r_s & 0 \\ 0 & 0 & 0 & r_s \end{bmatrix} \cdot \begin{bmatrix} i_a \\ i_a - i_f \\ i_b \\ i_c \end{bmatrix} + \begin{bmatrix} e_{a_h} \\ e_{a_f} \\ e_b \\ e_c \end{bmatrix} + \\ + \begin{bmatrix} L_{ah} & M_{a_h a_f} & M_{a_h b} & M_{a_h c} \\ M_{a_h a_f} & L_{af} & M_{a_f b} & M_{a_f c} \\ M_{a_h b} & M_{a_f b} & L_b & M_{bc} \\ M_{a_h c} & M_{a_f c} & M_{bc} & L_c \end{bmatrix} \frac{d}{dt} \begin{bmatrix} i_a \\ i_a - i_f \\ i_b \\ i_c \end{bmatrix} \tag{3.3}$$

where the back emf voltages are given by,

$$\begin{bmatrix} e_{a_h} \\ e_{a_f} \\ e_b \\ e_c \end{bmatrix} = \begin{bmatrix} \omega_e \cdot \bar{\Delta} \lambda_{pm} \cdot \sin(\theta) \\ \omega_e \cdot \Delta \lambda_{pm} \cdot \sin(\theta) \\ \omega_e \cdot \lambda_{pm} \cdot \sin(\theta - \frac{2\pi}{3}) \\ \omega_e \cdot \lambda_{pm} \cdot \sin(\theta + \frac{2\pi}{3}) \end{bmatrix} \tag{3.4}$$

The back EMF in the total phase is the sum of the healthy and faulted induced back

EMFs voltages. From figure 3.2, the voltage equation for each of the coils in phase A is given by,

$$v_a = v_{ah} + v_{af} \tag{3.5}$$

$$v_{af} = i_f \cdot r_f \tag{3.6}$$

By replacing equations 3.5 and 3.6 into the model equation 3.3, it is possible to rearrange the system of equations with the turn-to-turn fault as shown by the new system of equations 3.7.

$$\begin{bmatrix} v_a \\ v_b \\ vc \\ 0 \end{bmatrix} = \begin{bmatrix} r_s & 0 & 0 & -r_{af} \\ 0 & r_s & 0 & 0 \\ 0 & 0 & r_s & 0 \\ -r_{af} & 0 & 0 & r_{af} + r_f \end{bmatrix} \cdot \begin{bmatrix} i_a \\ i_b \\ i_c \\ i_f \end{bmatrix} + \begin{bmatrix} e_a \\ e_b \\ e_c \\ -e_f \end{bmatrix} + \begin{bmatrix} L_a & M_{a_h b} + M_{a_f b} & M_{a_h c} + M_{a_f c} & -(L_{a_f} + M_{a_h a_f}) \\ M_{a_h b} + M_{a_f b} & L_b & M_{bc} & -M_{a_f b} \\ M_{a_h c} + M_{a_f c} & M_{bc} & L_c & -M_{a_f c} \\ -(L_{a_f} + M_{a_h a_f}) & -M_{a_f b} & -M_{a_f c} & L_{a_f} \end{bmatrix} \frac{d}{dt} \begin{bmatrix} i_a \\ i_b \\ i_c \\ i_f \end{bmatrix} \tag{3.7}$$

The system of equations 3.7 is more suitable to represent and model a faulted PMSM and it can be divided in two parts. First, rows $1 \rightarrow 3$ represent the remaining healthy part of the motor and the influence of the fault current. This part of the model shows that the PMSM is capable of keep on operating and producing torque after a turn-to-turn fault takes place. The second part is the faulted circulating current model, this is the fourth row in the system of equations. This fault current is governed by the number of turns involved in the

fault, the line currents and the rotor speed as $e_f \propto \omega_e$.

Some remarks deducted from this model are as follows:

1. The fault current is directly proportional to the fault resistance, this includes the winding internal resistance r_{af} and the resistance due to the damage to the insulation r_f, named the fault point of contact.

2. High mutual inductances between coils have a negative impact in the performance of a faulted PMSM. This is because mutual inductances between the coils enable the remaining phases in the machine to contributed toward the fault current in a indirect manner.

3. Parameters are dependent on the PMSM topology and the number of turns involved in the fault. For accuracy, these parameters are determined using finite element analysis, (FEA).

3.3 Frame of Reference Transformation Including the Fault

As shown in equation 3.7 the system has four variables. This complicates the transformation as Park's in equation 2.4 transforms three variables to two. This problem is solved by augmenting Park's transformation matrix. The resultant matrix is known as the Concordia transformation and is given in equation 3.8, [19].

$$\Gamma_{(abcf\rightarrow dqh_0f)} = \frac{2}{3}\begin{bmatrix} \cos(\theta) & \cos(\theta-\frac{2\pi}{3}) & \cos(\theta+\frac{2\pi}{3}) & 0 \\ \sin(\theta) & \sin(\theta-\frac{2\pi}{3}) & \sin(\theta+\frac{2\pi}{3}) & 0 \\ \frac{1}{2} & \frac{1}{2} & \frac{1}{2} & 0 \\ 0 & 0 & 0 & \frac{3}{2} \end{bmatrix} \tag{3.8}$$

This transformation is used to change from the stator frame of reference to the rotor frame of reference, (3.9), including the fault.

$$\begin{bmatrix} d \\ q \\ h_0 \\ f \end{bmatrix} = \Gamma \begin{bmatrix} i_a \\ i_b \\ i_c \\ i_f \end{bmatrix} \tag{3.9}$$

In this new set of equations, h_0 is the zero sequence component. For a faulted machine $h_0 \neq 0$ as the fault throws off the electrical symmetry of the stator windings. Equations 6.1 to 3.13 show the faulted model of a PMSM in the dq frame of reference.

$$\begin{aligned} v_d = 2/3(i_d r_s + e_d + L_d\frac{di_d}{dt} - i_f r_{af}\sin(\theta) - \frac{di_f}{dt}(L_{af} + M_{a_h a_f})\sin(\theta)) \\ = \bar{v}_d + \tilde{v}_d \end{aligned} \tag{3.10}$$

$$\begin{aligned} v_q = 2/3(i_q r_s + e_q + L_q\frac{di_q}{dt} - i_f r_{af}\cos(\theta) - \frac{di_f}{dt}(L_{af} + M_{a_h a_f})\cos(\theta)) \\ = \bar{v}_q + \tilde{v}_q \end{aligned} \tag{3.11}$$

where $\bar{v}$ is the expected healthy value and $\tilde{v}$ is the variation cause by the fault.

The zero sequence component of the applied voltage vector and the fault voltage are calculated using equations 3.9 and are shown in equations 3.12 and 3.13.

$$v_o = h_o = \frac{1}{2}\left(-i_f r_{af} - (L_{af} + M_{a_1 a_2})\frac{di_f}{dt} + e_o\right) \tag{3.12}$$

$$v_f = f = \frac{3}{2}\left(-i_a r_{af} + i_f(r_{af} + r_f) - e_f - (L_{af} + M_{a_1 a_2})\frac{di_a}{dt} + L_{af}\frac{di_f}{dt}\right) \tag{3.13}$$

Equation 3.13 comes from the extended Concordia Park's transformations.

Chapter 4

Fault Tolerant Machines Specifications and Characteristics

Two PMSMs were designed and built to study the effects of turn-to-turn faults in PMSMs, a fractional 2/5 SPP single layer machine and a fractional 1/2 SPP double layer machine. These types of motors are used in transportation products, such as hybrid powertrains, where any type of failure can endanger lives. This drives the motivation and the interest in studying how different winding configurations affect the fault behavior and determine which type of winding has better fault tolerance. Extensive experimentation was performed to both machines to demonstrate and study the fault behavior for each winding configuration.

The detailed design process for the machines is fully described in [48], and the background theory comes from [49]. This work is focused on fault current mitigation for turn-to-turn faulted PMSMs and therefore, only a brief description about the motor parameters is presented in this chapter.

4.1 Design

Standard induction motor WEG frames were used to house the fractional winding permanent magnet machines. This fabrication method is simple, fast and low cost, but the final product has poor cooling properties. Cooling issues were overcame by performing short duration

experiments under controlled operating conditions. Having poor cooling is bad for any electrical component; however, for research purposes, this bad quality offers a way to study the thermal effects due to a fault under accelerated conditions.

4.1.1 Stator and Rotor Configuration

Figure 4.1 shows the motors used to study the behavior of turn-to-turn faults and the possibility of fault current mitigation. Both motors have concentrated windings, this type of winding has better fault toleration than distributed windings. The reason is that in concentrated windings the phases are wound physically separated from each other.

The difference in the two windings is the number of layers. Figure 4.1(a) shows a single layer machine vs. figure 4.1(b) that is a double layer machine. As shown in figure 4.1(a), single layer machines offer better physical isolation between the phases. In this winding topology the phase coils do not share the stator teeth nor the slot opening, therefore, maximum physical isolation is archived. The advantage of having physically isolated coils is that in the event of a controlled failure, only the affected phase suffer the effects of the fault, not the remaining phases.

The double layer machine, figure 4.1(b), also has a concentrated winding, where each coil is separately wound. The disadvantage with this winding configuration is that the coils share the slot openings. Depending on the fault severity, a healthy coil sharing the slot with a faulted coil could be affected by the effects of the fault.

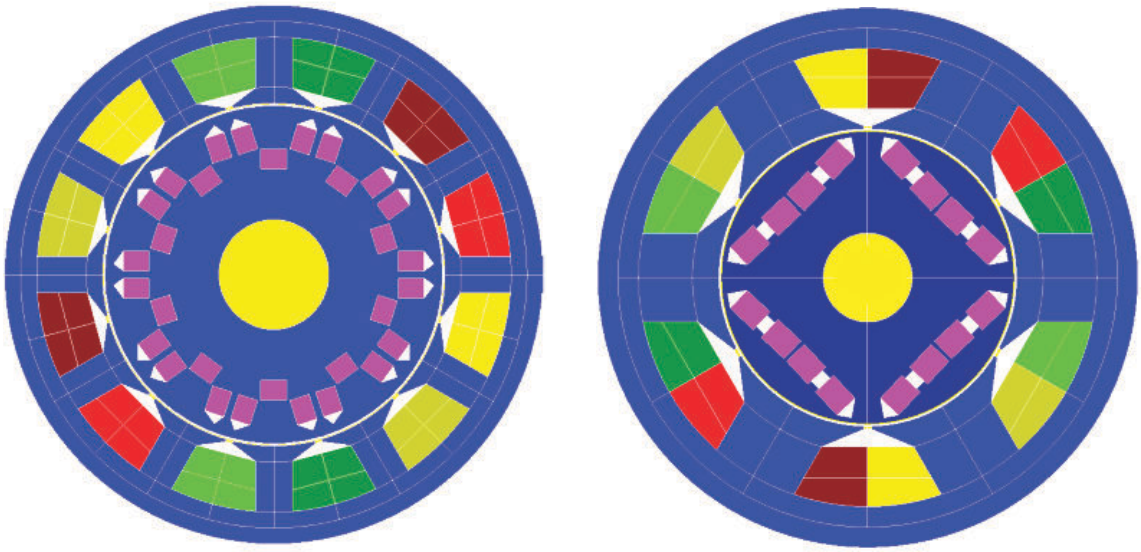

(a) A single layer 2/5 SPP concentrated fractional winding PMSM

(b) A double layer 1/2 SPP concentrated fractional winding PMSM

Figure 4.1: Fault tolerant PMSM with fractional winding configuration

Table 4.1: Stator and Rotor physical specifications

Motor parameters	2/5 SPP machine	1/2 SPP machine
number of phases	3	3
number of slots	12	6
number of poles	10	4
number of turns per coils	150	152
Rotor Diameter	69 mm	49.2 mm
Stator Diameter	110 mm	91 mm
Airgap	1 mm	1 mm
Machine Length	72 mm	72 mm
Magnet type	NdFeB	NdFeB

4.2 Winding Configuration

A detailed study of turn-to-turn faults is not feasible with off-the-shelf PMSMs, as the windings are internally connected and only the three input phases are accessible. Therefore, the fault current, induced by an insulation failure between two or more turns, is not measurable from the input terminals. This problem was solved by constructing the two PMSMs with the phase A winding sectioned into coils as shown in figure 4.2. Each of these coils is wired and

connected to an interconnection box, where it is possible to externally insert a fault resistor and monitor the circulating fault current.

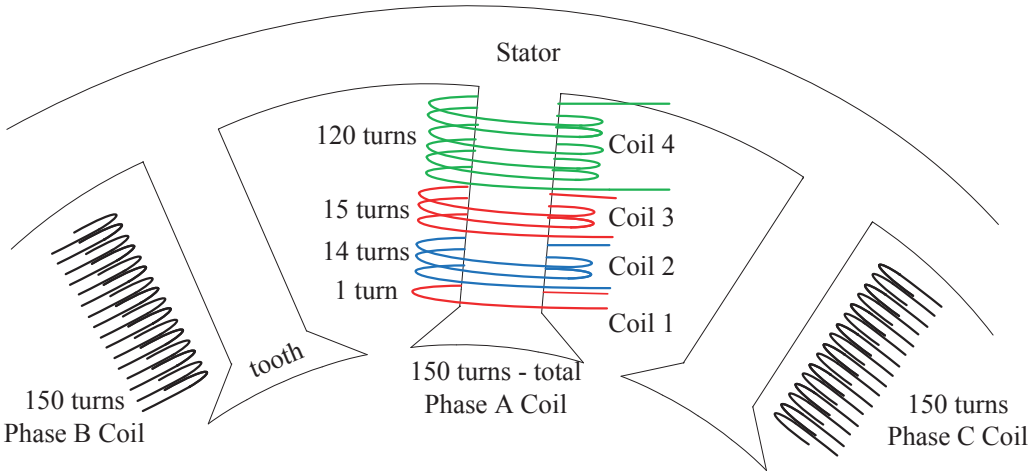

(a) Stator Winding configuration for the double layer 2/5 SPP concentrated fractional winding PMSM

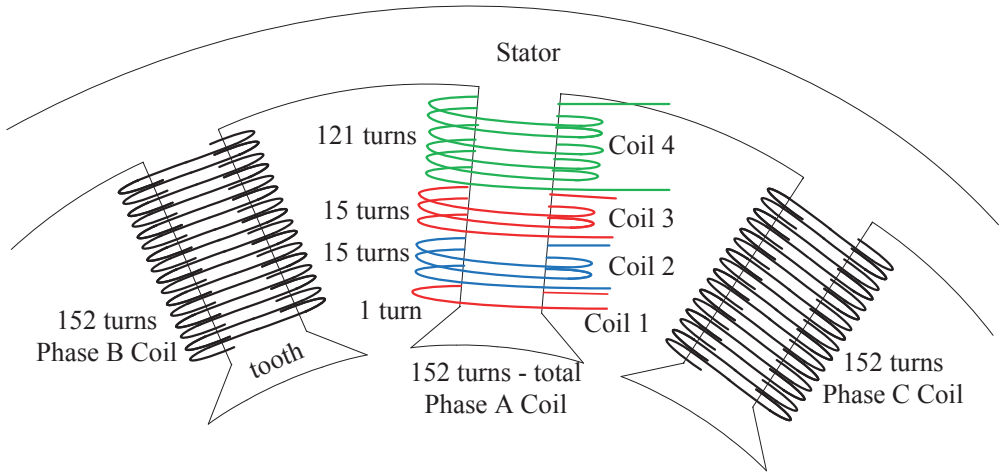

(b) Stator Winding configuration for the double layer 1/2 SPP concentrated fractional winding PMSM

Figure 4.2: Stator winding configuration for the fabricated PMSMs

Splitting of a phase coil into separated coils, as shown in figure 4.2, allows for the study of the fault current behavior as a function of the number of turns involved. For example, it is possible to study a one turn failure by inserting any fault resistance across coil 1. Coils 1 and 2 can be combined to represent 10% of the turns in the coil faulted; while the combination

of coils 1, 2 and 3 can be used to represent a 20% coil failure.

The resistance of the coils, r_s, is determined analytically by estimating the length of the coil and the its cross sectional area using the resistance equation 4.1. These quantities are estimated using the wire gauges and winding configuration information.

$$R = \rho \frac{l}{A} \tag{4.1}$$

The resistance value is verified using accurate measurements once the machine is assemble. In this work the resistance was measured using a multi-meter.

4.3 Finite Elements Analysis: Magneto Static Analysis to Extract parameters

This chapter is focused on the determination of the machine parameters using finite elements analysis, which is a reliable tool for electro-mechanical simulations. These parameters are used to populate and solve the faulted PMSM model presented in chapter 3. Through FEA it is possible to determine all the parameters for any specific fault scenario.

4.3.1 Inductance Determination Procedure, Including a Turn-to-Turn Fault

To determine the inductances of the phases and the faulted coil a magneto static FEA simulation was performed without the rotor magnets, as it is shown in figure 4.1. This eliminates the magnetic flux due to the magnets and allows for the determination of the coil inductances. The geometry used for the inductance determination is shown in figure 4.3,

where $phasef$ models the turns involved in a fault.

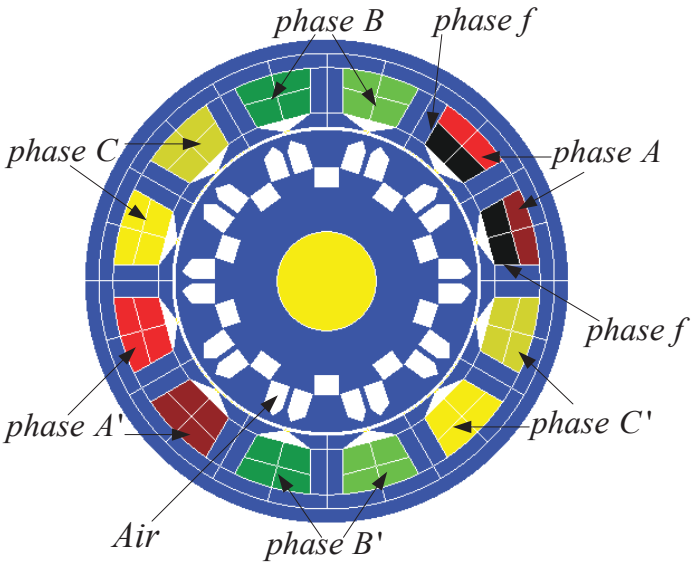

Figure 4.3: FEA geometry setup for the magneto static simulation, used to determinate the inductances of the $2/5SPP$ machine.

In the finite elements analysis each phase region, including the faulted region $phasef$, is assigned to a coil conductor. The analysis is performed by applying current in only one of the coils conductors, while measuring the magnetic flux across all the coils conductors. Using this information the self and mutual inductances for a given fault scenario are calculated using equation 4.2.

$$inductance = \frac{\lambda}{i} \tag{4.2}$$

The same finite elements analysis and geometric alteration procedures were performed for the $1/2SPP$ machine.

4.3.2 Fault Study Case and Nominal Parameters

In this section the inductances required to develop model equation 3.3 are determined for the specific case of a fifteen turns insulation failure. The technique described in section 4.3.1 is used to determine these inductances for the specific case, but it is applicable to any other fault scenarios.

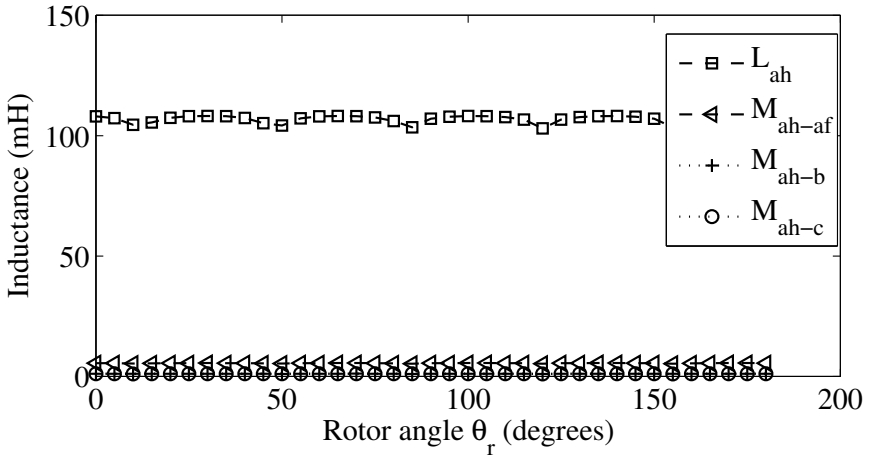

(a) Phase A remaining healthy coil a_h inductance L_{ah} and the mutual inductances between the other coils, including the faulted region. Specific case: $N_f = 15\ turns$ - 2/5 SPP single layer machine.

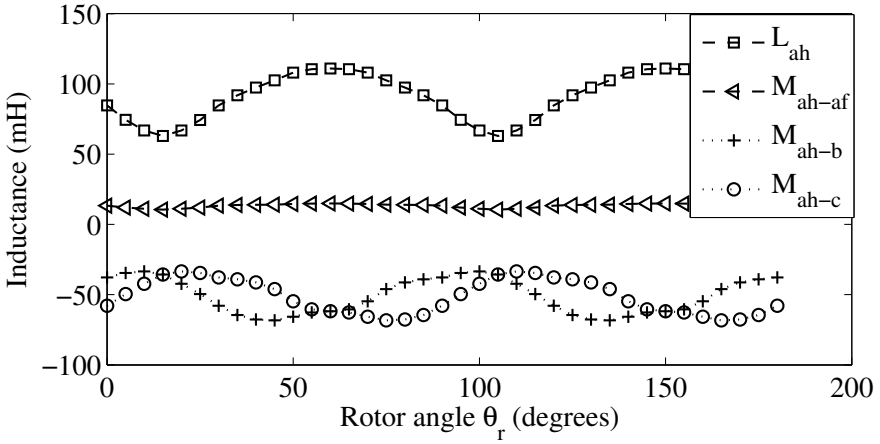

(b) Phase A remaining healthy coil a_h inductance L_{ah} and the mutual inductances between the other coils, including the faulted region. Specific case: $N_f = 15\ turns$ - 1/2 SPP double layer machine.

Figure 4.4: Inductances determination; in this case current is applied only to the healthy part of phase A and the magnetic flux generated by the current across all the coils is measured.

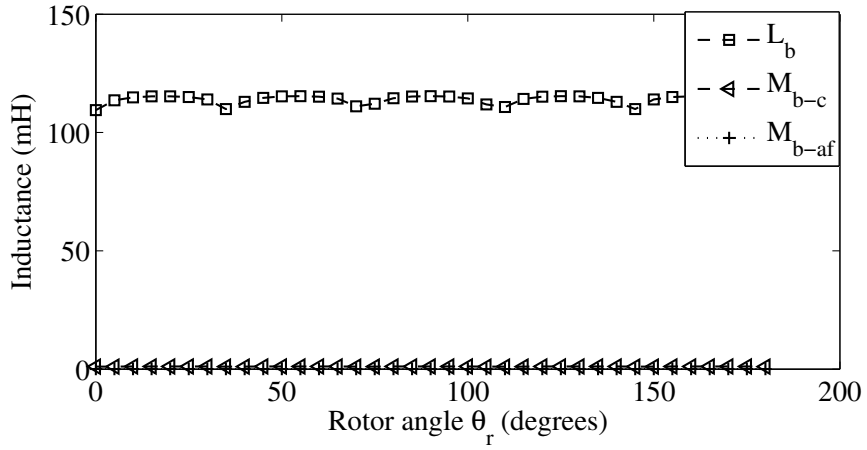

(a) Healthy phase B coil a_b inductance $L_b = L_s$ and the mutual inductances between the other coils, including the faulted region. Specific case: $N_f = 15\ turns$ - 2/5 SPP single layer machine.

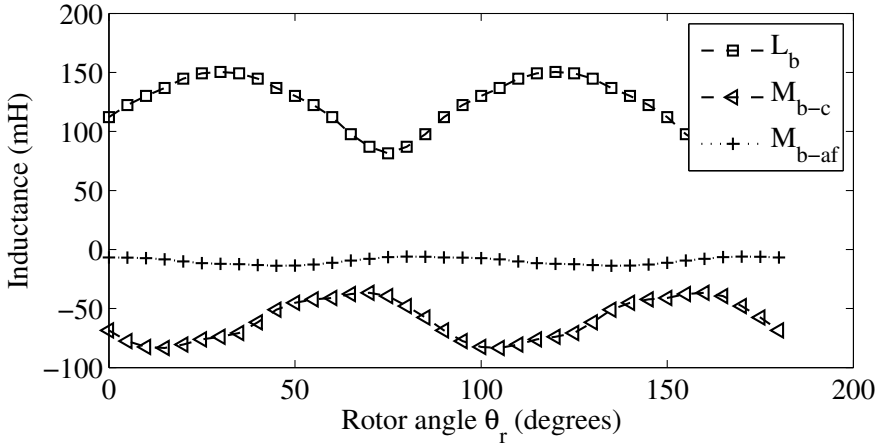

(b) Healthy phase B coil a_b inductance $L_b = L_s$ and the mutual inductances between the other coils, including the faulted region. Specific case: $N_f = 15\ turns$ - 1/2 SPP double layer machine.

Figure 4.5: Inductances determination; in this case current is applied only to the healthy phase B and the magnetic flux generated by the current across all the coils is measured.

It is important to notice the inductance behavior differences between the single layer 2/5 SPP machine and the double layer 1/2 SPP. Figures 4.4, 4.5 and 4.6 show the main and most important difference between the machines, where high mutual inductances were detected in the double layer winding. The mutual inductances between the phases for the double layer machines oscillates between 36.65 mH and 83.45 mH as shown in figure 4.5(b).

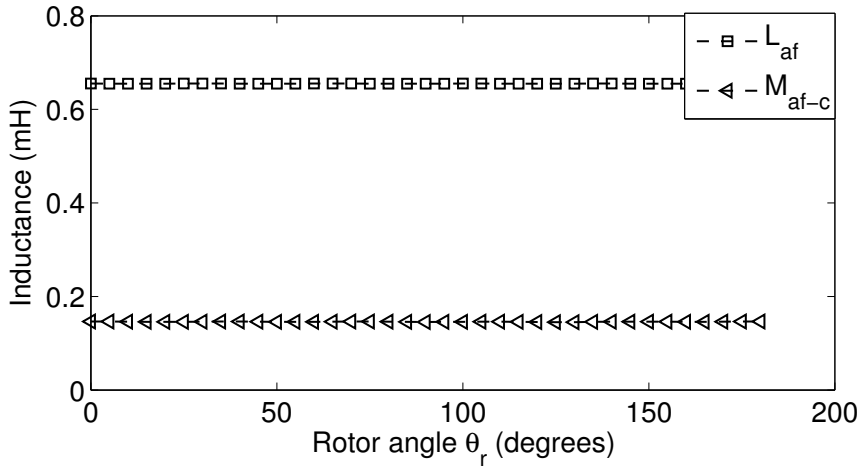

(a) Faulted coil a_f inductance L_f and the mutual inductances between the other coils, including the healthy phases $M_{a_fc} = M_{a_fb}$. Specific case: $N_f = 15$ *turns* - 2/5 SPP single layer machine.

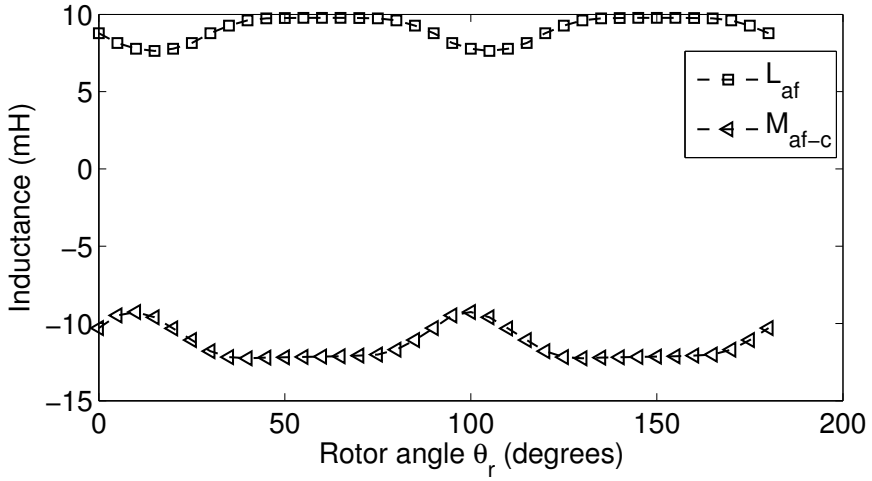

(b) Faulted coil a_f inductance L_f and the mutual inductances between the other coils, including the healthy phases $M_{a_fc} = M_{a_fb}$. Specific case: $N_f = 15$ *turns* - 1/2 SPP double layer machine.

Figure 4.6: Inductances determination; in this case current is applied only to the faulted coil conductor and the magnetic flux generate by the current across all the coils is measured.

In the double layer machine the slot opening contains two different coils from two different phases, as shown in figure 4.2; therefore, high coupling between all the coils exists. This behavior does not exist in the single layer winding machine, since each coil is wound around a tooth and dosn't share any slot opening. This gives the advantage to the single layer

2/5 SPP machine as a fault tolerant PMSM.

Another peculiarity on the 1/2 SPP machine is the magnitude of the inductances variation as a function of the rotor position. Figure 4.5(b) is a clear example of these inductances variation, in the 2/5 SPP machine the L_b varies from 110.5 mH to 115.3 mH, whereas in the 1/2 SPP the variations are from 81.5 mH to 150.0 mH.

A summary of the machine parameters is given in tables 4.2 and 4.3.

Table 4.2: Healthy PMSM Parameters

Motor parameters	2/5 SPP machine	1/2 SPP machine
$L_s = L_a = L_b = L_c$	112 mH average	122 mH average
$M_s = M_{bc} = M_{ca} = M_{ab}$	≈ 0	62 mH average
λ_{pm}	0.23 $V.s$	1.51 $V.s$
R_s	1.5 Ω	1.5 Ω

Table 4.3: Machine Parameters Based on a 15 turns fault

Motor parameters	2/5 SPP machine	1/2 SPP machine
L_{ah}	107 mH average	92 mH average
L_{af}	0.655 mH average	8.8 mH average
$M_{a_h a_f}$	6.35 mH average	13.7 mH average
$M_{a_f b} = M_{a_f c}$	≈ 0	11.7mH

4.4 General Impedance Model for Turn-to-Turn Faulted PMSMs

In section 4.3.2 a technique to determine the parameters of the faulted machine, for a specific number of faulted turns, using finite elements analysis is described. The technique is accurate and detailed; however, it only models one specific fault scenario.

A model that accounts for fault severity changes is important in order to facilitate the study of the progression of a fault and its implication on the PMSM performance. In this

section the fault parameters are modeled using the information of the healthy machine with an analytical model based approximation. This allows the estimation of the fault quantities for any fault scenario in a relatively simplistic way.

First, the inductance of a N_{total} turns coil conductor around a tooth is calculated using P, the permeance, as shown in equation 4.3.

$$L = N_{total}^2 P \tag{4.3}$$

If an insulation failure occurs, the coil conductor is modeled by dividing the entire coil into two: a healthy and a faulted area as shown in figure 4.7.

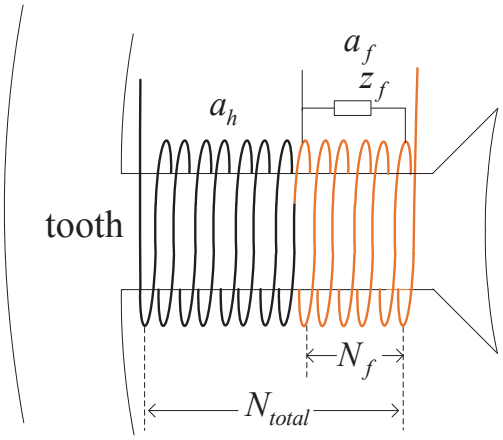

Figure 4.7: Single tooth, containing the faulted coil

The inductances for each of the coils is calculated as follows;

$$L_s = \mu N_{total}^2 \frac{A}{l} \tag{4.4}$$

$$L_{af} = \mu N_f^2 \frac{A_f}{l_f} \tag{4.5}$$

$$L_{ah} = \mu (N_{total} - N_f)^2 \frac{A_{ah}}{l_{ah}} \tag{4.6}$$

where L_s, L_{af} and L_{ah} are the healthy inductance, the inductance of the faulted coil and the inductance of the remaining healthy coil, respectively.

To find an analytical expression for the faulted coil inductance L_f, as a function of the number of turns involved in the fault and the healthy inductance, equation 4.5 is divided by equation 4.4. The resultant expression is given by equation 4.7.

$$L_{af} = L_s \Delta^2 k_{Al} \tag{4.7}$$

k_{Al} is a constant that represents the changes in the permeance of each coil due the fault. In this research the value of k_{Al} is determined using finite elements analysis. The value is dependent on the fault location and the turns involved in the fault.

Other important quantities to model the fault behavior are the mutual inductances between the faulted coil and all other healthy coils. This quantities are calculated using the healthy data of the machine as follows;

$$M_{a_h a_f} = \Delta(1 - \Delta) L_s \tag{4.8}$$

$$M_{a_f b} = M_{a_f c} = \Delta M_s \tag{4.9}$$

The proposed parametric modeling technique presented in section 4.4 is validated using FEA data as shown in figure 4.8. The FEA data was obtained using the parameter determination process presented in section 4.3 for different fault case scenarios; the results are compared to the analytically determined values as shown in figure 4.8. Both FEA and model based parameters are in agreement for the range of fault scenarios in figure 4.8.

Experimental validation of the proposed parametric modeling is shown figure 4.9, for

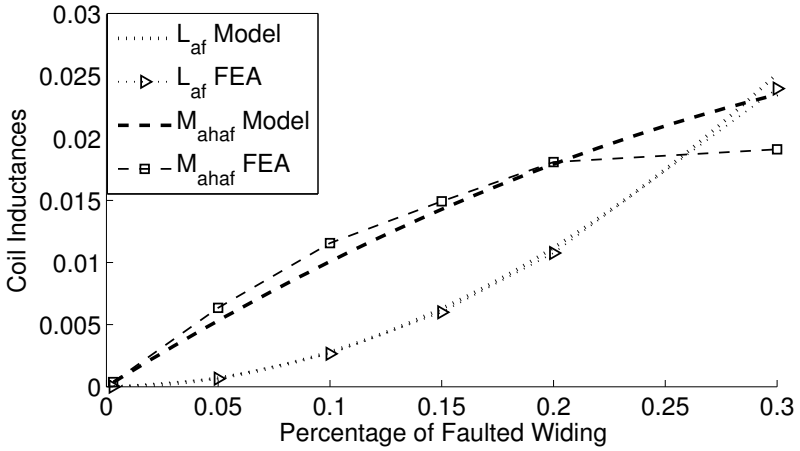

Figure 4.8: Parametric validation, where $k_{Al} = 2.5$ and $r_f = 0.5\ \Omega$

two operating conditions. For this validation the fault current was determined using FEA, calculated using the model with the analytical approximation of the parameters and experimentally measured.

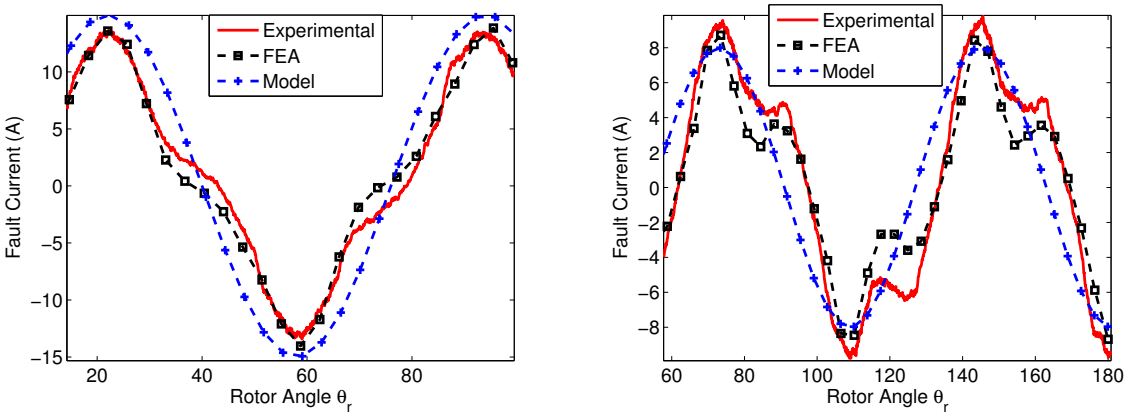

(a) Comparison for for commanded current $I = 10\ A < 90^o$

(b) Comparison for commanded current $I = 10\ A < 150^o$

Figure 4.9: Experimental, finite elements and modeling results comparison. Study case: 15 faulted turns, 300 RPM.

The same modeling technique applies to the 1/2 SPP machine.

4.5 Torque Experimental Determination

Figure 4.10 shows the torque profile for each of the PMSMs, determined from experimental data. These curves are required for the development of high performance motor drives. From them, it is possible to determine the conditions for which maximum torque per amp is achieved.

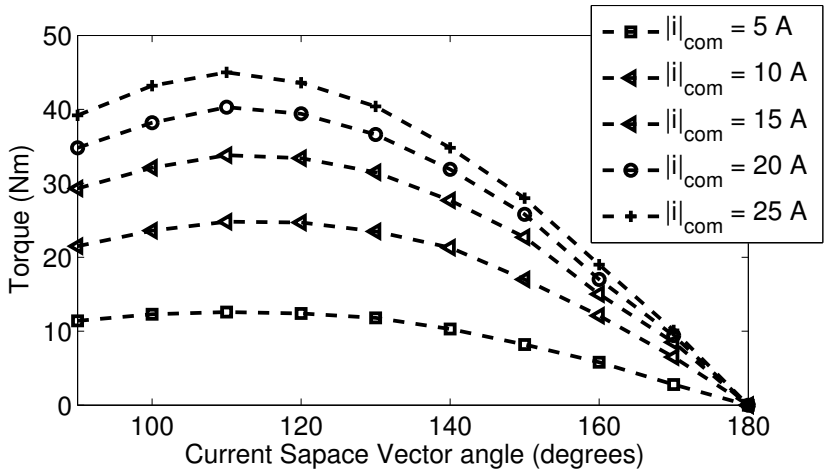

(a) 2/5 SPP machine torque as a function of the current space vector angle

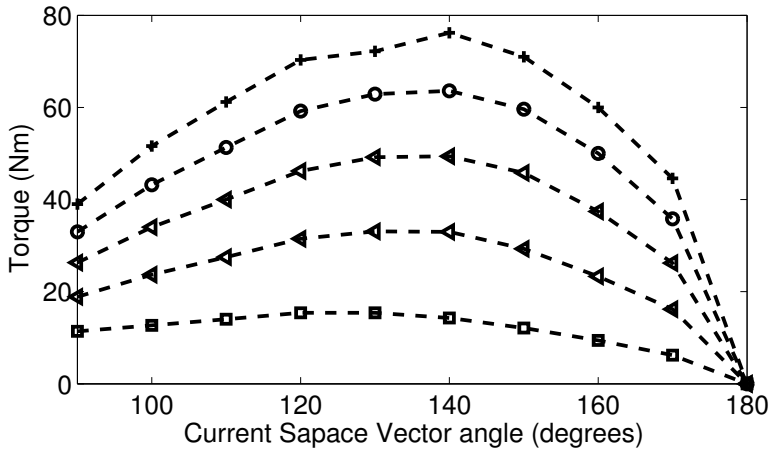

(b) 1/2 SPP machine torque as a function of the current space vector angle

Figure 4.10: Torque profiles as a function of the current space vector angle (δ), legend on figure 4.10(a) applies to figure 4.10(b)

Chapter 5

Fault Current Analysis and Behavior

This chapter explores the behavior of the fault current under different operating conditions. Through modeling, FEA and experimental data it is demonstrated that some degree of control is gained over i_f by controlling the current angle δ.

The concept is to use the angle of the space vector current to keep i_f at bay. It is demonstrated that using a field weakening technique at speeds below the rated gives sufficient controllability over i_f, enough to limit the current to a predetermined value.

5.1 Fault Current Analysis

The fault current in vector form is given by equation 5.2, it is calculated from the fault model described by figure 3.2 and equation 3.7. In this form it is clear that the fault current is fed by three quantities. The first one is the current in the phase where the fault resides ($i_a(t)$), the second quantity is the back EMF produced by the machine, and finally ($i_b(t)$) and ($i_c(t)$) through the mutual inductances between the faulted coil to the remaining healthy coils.

$$Z_{a_f} = r_f + r_{af} + j\omega L_{af} \tag{5.1}$$

where Z_{af} is the equivalent impedance across EMF e_{af}.

$$\vec{i}_f = \frac{\vec{i}_a \cdot \left\{ r_{af} + j\omega \cdot (L_{af} - M_{a_f a_h}) \right\}}{Z_{a_f}} + \frac{\Delta\lambda_{pm}\omega}{Z_{a_f}} - \frac{j\omega \cdot (M_{a_f b} \cdot \vec{i}_b + M_{a_f c} \cdot \vec{i}_c)}{Z_{a_f}} \tag{5.2}$$

The fault current contribution due to the mutual inductances, $M_{a_f b}$ and $M_{a_f c}$, in equation 5.2 can be neglected depending on the topology of the PMSM. The electrical circuit shown in figure 5.1 must be carefully studied using the motor winding structure and geometry to determine the impact of the mutual inductances. Generally PMSMs are designed with low mutual inductances, such as the single layer winding PMSM presented in chapter 4.

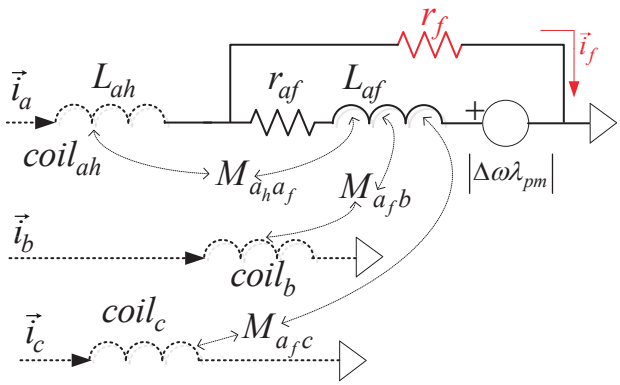

Figure 5.1: Electrical model for the faulted phase

$M_{a_h a_f}$ plays an important role in the development of fault current in the faulted area. This mutual inductance, $M_{a_h a_f}$, is not negligible as the faulted coil shares the same slot with the remaining healthy part of the coil. This coupling between the healthy and faulted parts of the coil allows $i_a(t)$ to contribute toward the fault current in a direct manner, as it is electrically connected and indirectly through $M_{a_h a_f}$.

Assuming that $M_{a_f b}$ and $M_{a_f c}$ are nearly zero, the fault current phasor in equation 5.2 is simplified to equation 5.3. For the purposes of this work, this assumption is valid, since

the 2/5 SPP machine presented in chapter 4 is used for experimental validation.

$$\vec{i}_f = \overbrace{\vec{i}_a \cdot \frac{\left\{r_{af} + j\omega \cdot (L_{af} - M_{af}a_h)\right\}}{Z_{af}}}^{\vec{i}_a \text{ contribution}} + \underbrace{\frac{\Delta\lambda_{pm}\omega}{Z_{af}}}_{\text{Back EMF contribution}} \tag{5.3}$$

With this assumption the main contributors to the fault current are $i_a(t)$ and the back emf induced by the magnets across the faulted coil. The line current $i_a(t)$ is a quantity that depends on the operating conditions of the PMSM, speed, power and torque. Therefore, it is important to regulate these operational conditions under post-fault operation.

5.1.1 Induced Fault Current in the Faulted Loop

In this subsection the fault current contribution from the back emf, as shown in the second terms of equation 5.3 is analyzed. The fault severity (r_f) and the rotor speed are contributors to the fault current by magnetic induction. To understand this behavior the line currents are set to zero. Under this condition, i_f exist only if the PMSM rotor moves inside the stator.

The electrical model for this case is given by the circuit shown in figure 5.2 and the fault current in the time domain is calculated as shown in equation 5.4.

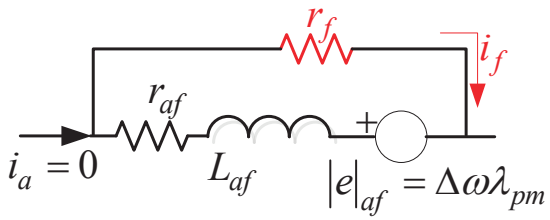

Figure 5.2: Fault current as a function of the rotor speed and fault Severity

$$i_f(t) = \frac{\Delta\omega\lambda_{pm}}{Z_{af}}\sin(\omega t) \tag{5.4}$$

The magnitude of the fault is calculated as a function of the speed and the fault severity (r_f) as shown in equation 5.5.

$$|i|_f = \frac{|e_{af}|}{|Z_{af}|} = \frac{\omega_e \Delta\lambda_{pm}}{\sqrt{R_f^2 + \left(\omega L_{af}\right)^2}} = \frac{\left(\Delta\lambda_{pm}\right)^2 \cdot \omega^2}{R_f^2 + \left(\omega L_{af}\right)^2} \tag{5.5}$$

where $R_f = r_f + r_{a_f}$

Having knowledge of the fault current magnitude helps to determine which operating conditions exceeds the current limits of the winding. Equation 5.5 is analyzed at its extreme conditions, when the impedance approaches a pure resistor and when it approached an inductive behavior.

First let assume that $R_f \gg X_{L_{af}}$, where the fault impedance is mostly inductive. Under this condition the fault current magnitude is approximated as,

$$|i|_f \approx \frac{\Delta\lambda_{pm}}{R_f} \cdot \omega_e \tag{5.6}$$

For a PMSM with a low severity faults, where R_f is reasonably larger, it is concluded that the fault current is directly proportional to the speed. The fault current shows a linear behavior with a slope equal to $\Delta\lambda_{pm}/R_f$. This slope is directly related to the number of turns involve in the fault and the characteristic rotor magnets flux linkage.

The second case to study, is the case when the impedance is dominated by the inductance term, $X_{L_{af}} \gg R_f$. For this case the fault current is estimated as follows,

$$|i|_f \approx \frac{\Delta\lambda_{pm}}{L_{af}} \approx \frac{\Delta\lambda_{pm}}{\Delta^2 L_{as}} = \frac{\lambda_{pm}}{\Delta L_{as}} = \frac{N_{total}\lambda_{pm}}{N_f L_{as}} \tag{5.7}$$

where L_{as} is the healthy characteristic line inductance.

For this extreme case, the fault current is only dependent on the number of turns involved in the fault and the PMSM characteristics, not the rotor speed.

Figure 5.3 shows the complete fault behavior dictated by equation 5.5. It also demonstrates that fault tolerant PMSMs designed with relatively high inductive characteristics are better at limiting the fault current, as it is bounded by $\Delta\lambda_{pm}/L_{af}$.

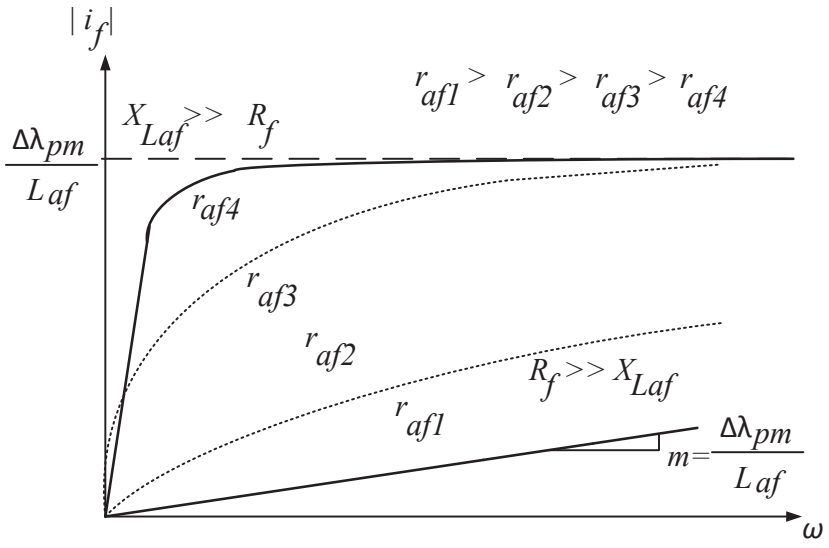

Figure 5.3: Open circuited PMSMs, fault current behavior

5.1.2 Fault Current Worst Case Scenario

It has been reported that the worst case scenario for a PMSM is the single turn fault. This statement is based on the fact that this fault has the lowest impedance and, therefore can allow the highest fault current flow. However, this statement is only valid for full short faults, where $r_f = 0\ \Omega$, as shown in figure 5.4. Table 4.2 shows the parameters used for this case study of the worst case scenario.

The goal of this work is to study the behavior of the fault current in the early stages of

a turn-to-turn fault, where $r_f > 0\ \Omega$, and before the fault becomes a full short circuit. The idea to to develop a controller capable of adjusting the operating conditions of the motor, that maintains acceptable currents and temperature levels, in order to stop the propagation of the fault.

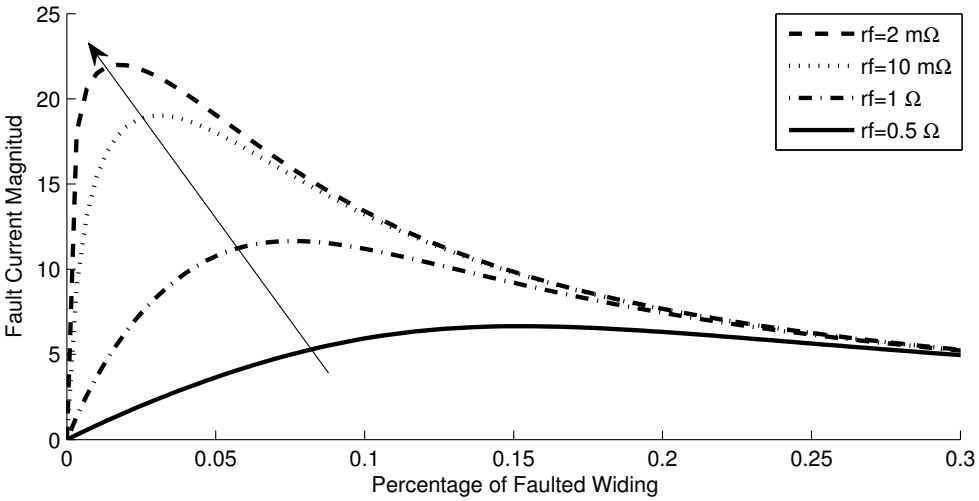

Figure 5.4: Open circuited PMSM at 300 RPM, worst case scenario as a function of the fault resistenace

Special consideration must be taken when dealing with incipient faults, as the maximum fault current no longer occurs when there is a single turn fault. Figure 5.4 shows the displacement of the maximum fault current peak as r_f increases. This behavior is due to the change in impedance across the fault. For low severity faults the worst scenario happens when the number of turns involved in the fault is considerably large. For this case, the current is primary driven by the emf voltage, $i_f \approx e_{af}/r_f$, and in order to create high fault current high e_{af} is required, which means more faulted turns.

The worst case for the fault current, in terms of the number of turns involved in the fault, is entirely coupled to the fault across the turns. In order to avoid over-stressing the faulted PMSM, this behavior must be well understood, since there is the possibility of operating

under the worst case scenario, and the control algorithm must recognize all the possible operating conditions.

5.2 Sensitivity Analysis

Sensitivity analysis is used to determine the effects upon the fault behavior due to changes in a parameter. The sensitivity, $S_{fault \to \xi}$, is calculated as shown in equation 5.8. With this analysis it is possible to determine how the current space vector, magnitude and angle, affects the fault current. The model shown in equation 5.3 is used to find the sensitivity of fault related quantities to changes in a parameter or input quantities as follows:

$$S_{fault \to \xi} = \frac{\partial F}{\partial \xi} \tag{5.8}$$

$$\partial F = F + F_{change} \tag{5.9}$$

$$\partial \xi = \xi + \xi_{change} \tag{5.10}$$

where $\partial \xi$ is the quantity changed by ξ_{change} and ∂F is the change in the behavior due to $\partial \xi$.

The sensitivity of the fault voltage $v_f = i_f r_f$ is determined in equation 5.11, in order to understand the effect of the current space vector angle upon the fault voltage. The results for $S_{i_f r_f \to \partial \delta}$ are shown in figure 5.5. This figure shows how the sensitivity of the fault voltage to the control angle δ increases as the current space vector angle is increased. It is important to notice that as the angle (δ) is increased, the voltage across the fault decreases. Having higher sensitivity as δ increases and the fact that the slop is positive, means that the voltage across the fault becomes more alterable as the angle δ is increased.

$$S_{i_f r_f \rightarrow \partial\delta} = \frac{\partial(i_f r_f)}{\partial\delta} \tag{5.11}$$

where $\partial\delta = 90^o - \delta_{change}$.

Since the fault current becomes more alterable as the angle δ is increased, a degree of control is gained upon this fault current. This translates to a gain of control over i_f by controlling the current angle δ. This serves as the basis for the mitigation technique proposed in this Dissertation.

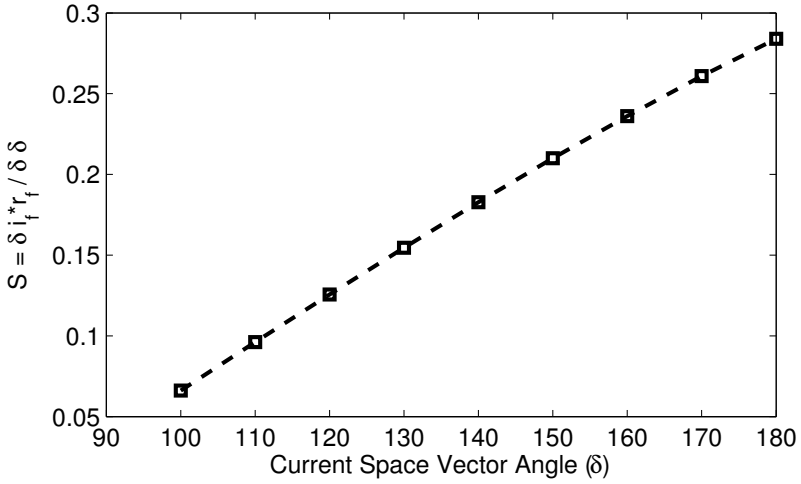

Figure 5.5: Sensitivity of $v_f = i_f r_f$ to changes in the current space vector angle (δ). Operating conditions; $\Delta = 15/300$, $speed = 300\ rpm$, $|I_a| = 5\ A$ and $r_f = 0.5\ \Omega$.

A similar behavior is noticed with the sensitivity of the voltage across the fault due to changes in the current space vector magnitude is calculated. This calculation was performed according to equation 5.12 for different values of the angle δ, and the results are shown in figure 5.6. It is concluded that the changes in $|I_s|$ have more effect upon the voltage across the fault as the angle δ is increased. This is in accordance this figure figure 5.5 and means that at higher angles the i_f becomes more alterable; and therefore, the magnitude of the current space vector has higher impact upon i_f.

$$S_{i_f r_f \to \partial |I_s|} = \frac{\partial (i_f r_f)}{\partial |I_s|} \tag{5.12}$$

where $\partial |I_s| = |I_s| - |I_s| \cdot \%change$.

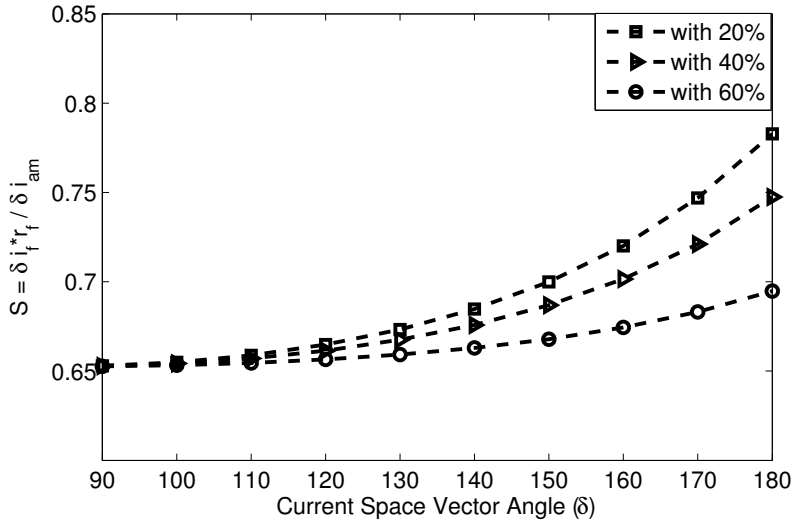

Figure 5.6: Sensitivity of $v_f = i_f r_f$ to changes in the current space vector magnitude. Operating conditions; $\Delta = 15/300$, $speed = 300\ rpm$ and $r_f = 0.5\ \Omega$.

5.3 Fault Current Behavior for Various Operating Conditions: Analysis using FEA and Experimental Results

In this section the fault current behavior is tested using FEA and experimental data for different operating conditions. The FEA and experimental setups are discussed in subsections 5.3.1 and 5.3.2 respectively.

The goal of this subsection is to test the effects of the current angle δ upon the fault current. As mentioned in previous sections, this angle plays a vital role in the behavior of

the fault current.

5.3.1 Transient Magnetic FEA Setup

The geometry with the detailed mesh and the electric coupled circuit, used to simulate the fault, are shown in figures 5.7 and 5.8 respectively. These were developed using the electrical and mechanical specifications for the machines described in chapter 4. The regions for each of the areas are the same as in figure 4.3, where the faulted area is denoted by the black regions.

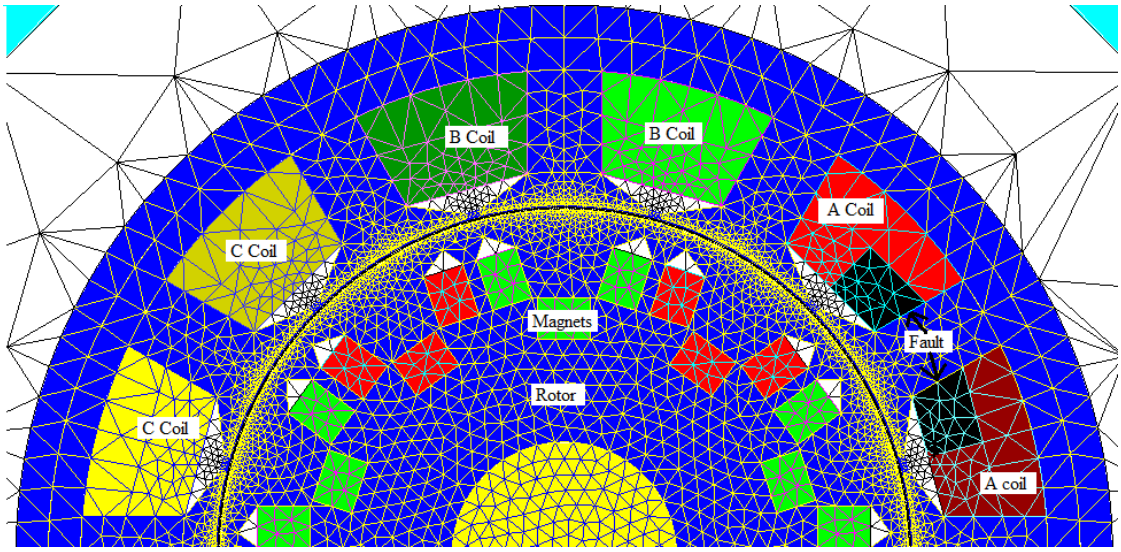

Figure 5.7: FEA geometry, including calculation mesh for the 2/5 SPP PMSM.

The circuit shows the different coils and passive elements in the machine, where R_s and L_s represent the line resistances and inductances. The faulted coil component is denoted by A_{af}, while A_{ah} represents the remaining healthy part of phase A coil, where the fault is inserted. The healthy phases B and C are represented by the coils components B and C.

Equations 5.13 to 5.15 shows the expressions for each of the current sources in figure 5.8. The parameters swept and step size for the FEA simulations are given in table 5.1.

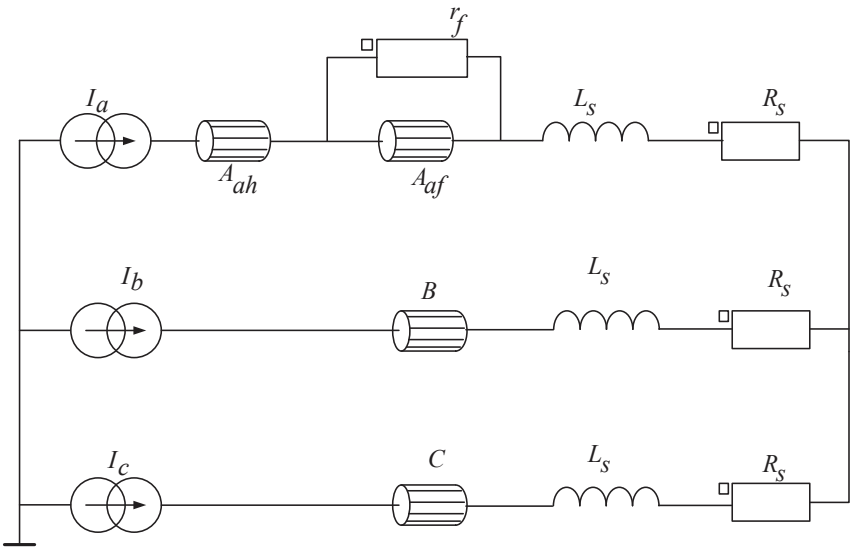

Figure 5.8: FEA Circuit, with the A coil divided into the healthy A_{ah} and the faulty A_{af} parts.

Table 5.1: Simulation parameters range and step size

Simulation parameter	Range	Step size
Rotor Angle Movement θ	0 to 180^o	2^o
Current Angle δ	90 to 180^o	10^o

$$i_a(t) = I\sin(\theta p + \delta) \tag{5.13}$$

$$i_b(t) = I\sin(\theta p - \frac{2\pi}{3} + \delta) \tag{5.14}$$

$$i_c(t) = I\sin(\theta p + \frac{2\pi}{3} + \delta) \tag{5.15}$$

where p are the pole pairs of the machine.

5.3.2 Experimental Setup

Figure 5.9 shows the block diagram of the setup utilized to collect all the experimental data. The top level controller in this figure controls the inverter in current mode; this control structure is described by the vector control setup shown in figure 2.7. The main characteristics of the electronics are given in table 5.2.

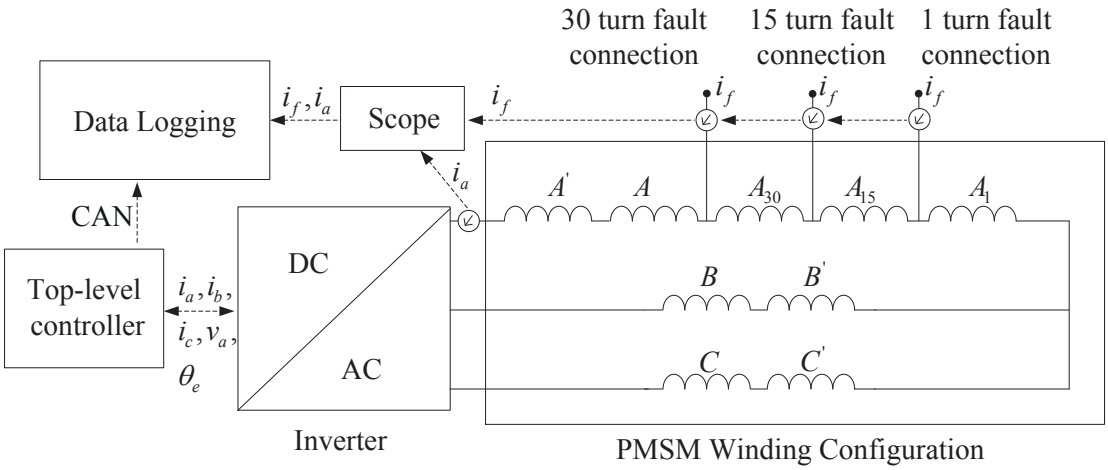

Figure 5.9: Experimental setup, with sectioned windings to insert the fault externally. The figure shows the winding configuration for the 2/5 SPP PMSM.

Table 5.2: Inverter and controller details

Specification	value	Specification	value
I_{max}	300 A	TI-DSP	TMS320F28335
V_{dcmax}	800 V	f_{sw}	10 kHz
CAN transmission speed	1 $Mbit/sec$	Sampling Rate	100 μs

The experimental data is recorded through the electric drive controller area network (CAN), to log the voltages command, rotor position and measured line currents. Using a high resolution oscilloscope the fault current and line current are measured. Information from the CAN unit and the scope are stored in the data logging computer.

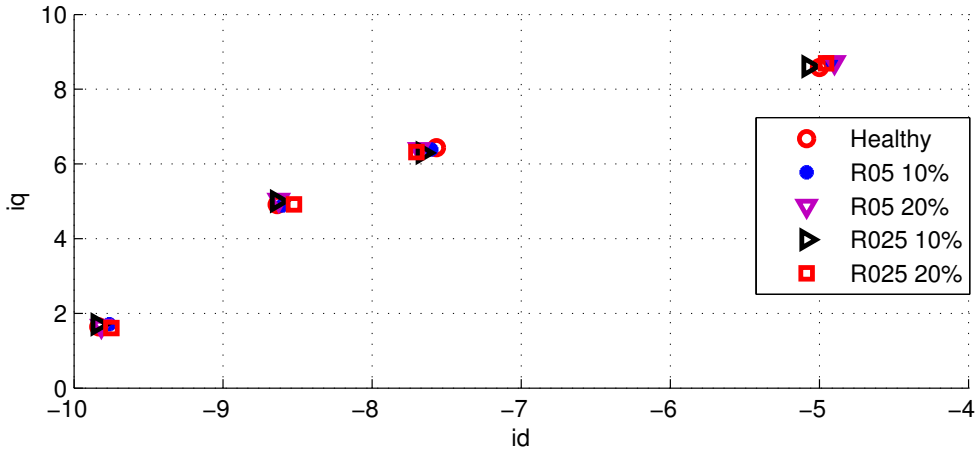

Figure 5.10: Measured current vector, $v_d + jvq$, while the 2/5 SPP PMSM experiences different fault conditions. Experiments were conducted at different angles of δ ,120^0, 140^0, 150^o and 170^o, throughout the experimentation process the space current vector magnitude at 10 A.

5.3.3 Drive's Current Controller Performance Under Turn-to-Turn Fault

Faults create harmonics, unbalanced conditions and other disturbances that can affect the performance of a motor drive. In this work the performance is defined as the capacity of the drive to maintain the commanded currents, under any operational condition. The controller performance is tested in this section because maintaining the correct current vector is crucial in the control of the fault current, especially the current angle δ.

The effectiveness of the current controller was tested for all the fault cases shown in fig. 5.10. As shown in this figure, the current controller was able to keep the desired direct and quadrature axis currents, regardless of the fault condition. Each data cluster in fig. 5.10 results from the angles 120^0, 140^0, 150^o and 170^o of the current space vector; the magnitude of the vector was kept constant at 10 A throughout the experiment.

The current waveforms for the fault case, $r_f = 1/2\ \Omega$ with 15 turns at 300 RPM, are

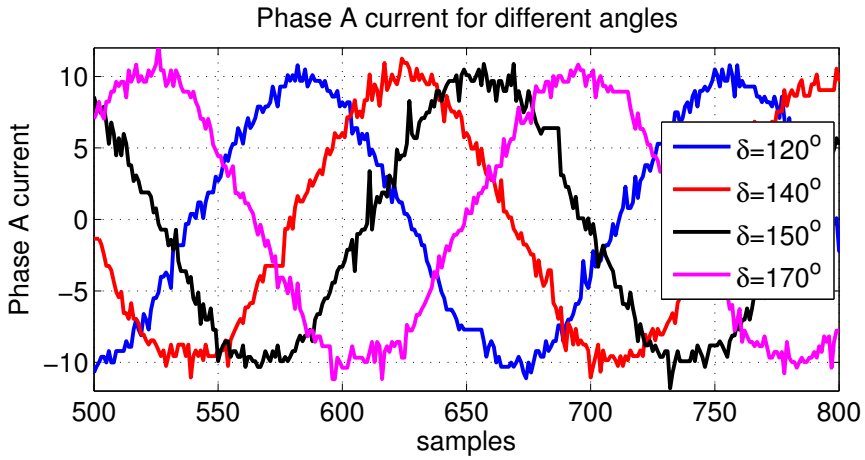

Figure 5.11: Phase A current in time domain, for different angles and a fixed magnitude of 10 A. The fault case is the 1/2 Ω fault for 15 turns at 300 RPM.

shown in fig. 5.11. This figure demonstrates that the controller is capable of tracking the commanded current, without having significant harmonic distortion.

5.3.4 Fault Current Behavior

FEA and experimental data were collected for faults across 15 and 30 turns with $r_f = 0.5\ \Omega$; while the speed was kept constant at 300 RPM. The current magnitude $|I|$ is kept constant to show only the effect of the current angle δ on the fault current. Normally in a motor drive both quantities, $|I|$ and δ change depending on the operating conditions. However, in this section the interest is to only show the dependence of the fault current on the angle, not the magnitude.

Figures 5.12 and 5.13 show the resultant fault current when the commanded line current magnitude $|I|$ is kept constant at 10 A, but its angle δ is swept from 90^o to 120^o and finally to 150^o. An important remark, is the decrease of the fault current magnitude as the current angle increases. This behavior was consistent for the 15 and 30 turns faults.

The fault progression and severity are mainly aided or caused by excess of heat in the

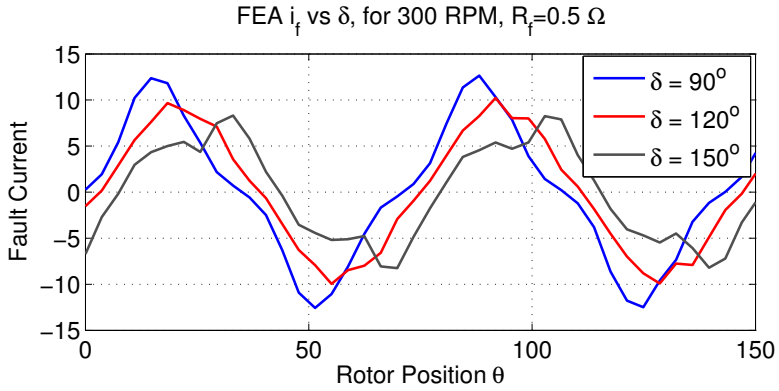

(a) Finite elements simulation for 90^o, 120^o and 150^o.

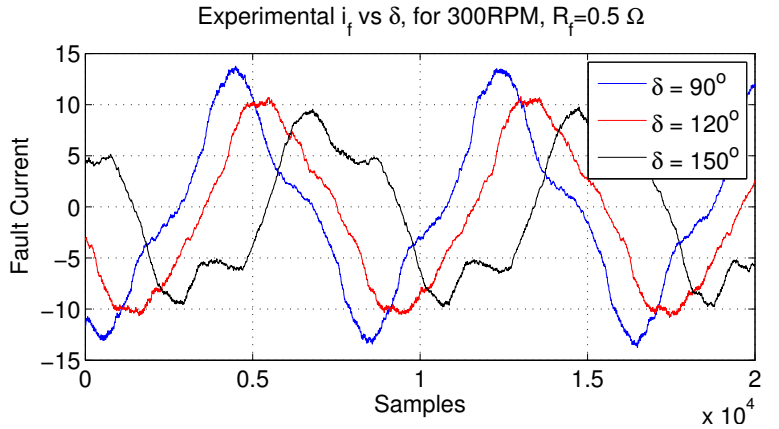

(b) Experimental results for 90^o, 120^o and 150^o

Figure 5.12: Results for a fault current thought 15 faulted turns, with $r_f = 0.5\ \Omega$. Speed fixed at 300 RPM and current space vector magnitude set to 10 A. This data was taken using the 2/5 SPP machine.

faulted location. This heat is caused by the increased power losses which depend on the true rms of the fault current; it is important to understand how the fault current true rms value changes as a function of the current angle. The effects of the true rms of the fault current are determined using the FEA and experimental data shown in figures 5.14 and 5.15.

Figures 5.14 and 5.15 show the resultant rms values for the 15 and 30 turns faults. Both figures show the attenuation of the true rms fault current. This shows how applying a field weakening d-axis current at speeds below the nominal reduces the fault current true rms value. Since, both data sets are in accordance with very similar results, it is concluded

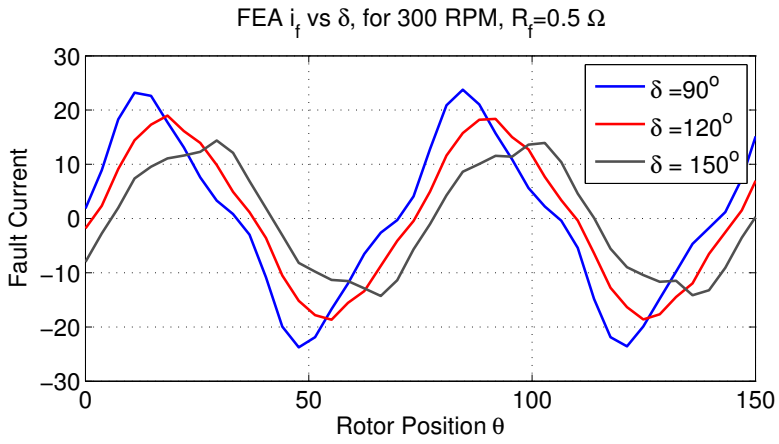

(a) Finite elements simulation for 90^o, 120^o and 150^o

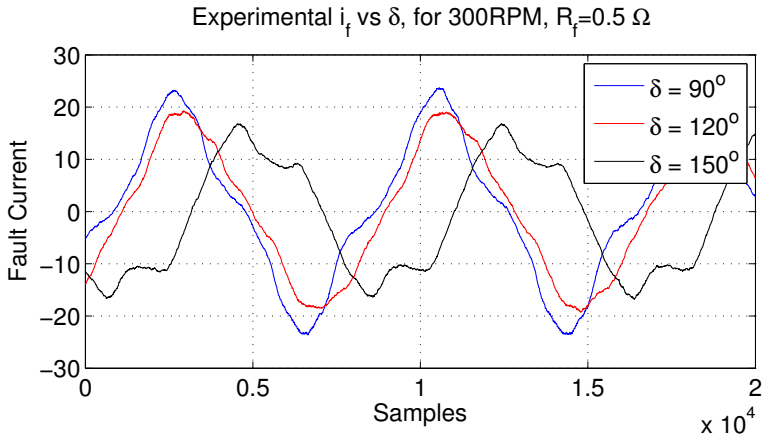

(b) Experimental results for 90^o, 120^o and 150^o

Figure 5.13: Results for a fault current thought 30 faulted turns, with $r_f = 0.5\ \Omega$. Speed fixed at 300 RPM and current space vector magnitude set to 10 A.This data was taken using the 2/5 SPP machine.

that the analysis and the FEA simulation setup are correct and closely resemble the real experimental results.

The effects of the current angle upon the fault current rms value were also tested at higher speeds, at 300 RPM, 500 RPM and 700 RPM, using experimental and FEA data; for different faulted turns conditions, 15 and 30 turns; and for different contact point resistances, $r_f = 0.5\ \Omega$ and $r_f = 0.25\ \Omega$. Figures 5.16, 5.17 and 5.18 show the fault current rms values behavior for $\delta = 120^o$, 140^o, 150^o and 170^o. The swept on the current angle δ starts at 120^o, since it is the optimal angle for maximum torque per amp (MTPA) operation and

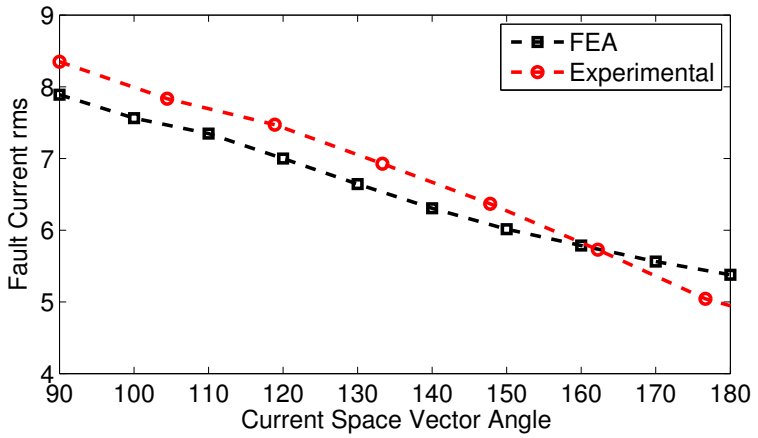

Figure 5.14: FEA and Analytical fault current RMS comparison for a 15 turns fault, with $r_f = 0.5\ \Omega$. Speed fixed at 300 RPM and current space vector magnitude set to 10 A. This data was taken using the 2/5 SPP machine.

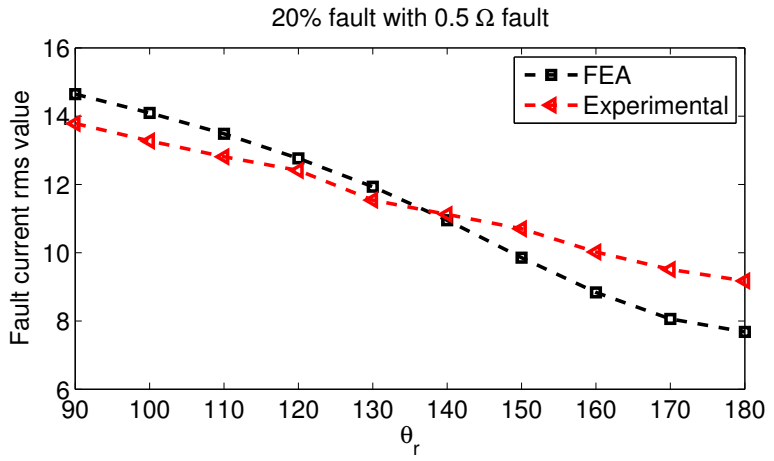

Figure 5.15: FEA and Analytical fault current RMS comparison for a 30 turns fault, with $r_f = 0.5\ \Omega$. Speed fixed at 300 RPM and current space vector magnitude set to 10 A. This data was taken using the 2/5 SPP machine.

the machine never operates below this angle. Even at higher speed and for different fault conditions, fault current mitigation is achieved as the angle δ is increased.

As the current angle δ increases, as a mitigation strategy to decrease the fault current causes, the output torque of the machine to be reduced. The worst case scenario studied in this work is shown in figure 5.17, where $r_f = 0.5\ \Omega$ and $N_f = 30$ turns at 500 RPM. Under normal operation the PMSM should be operating at the MTPA current angle, with

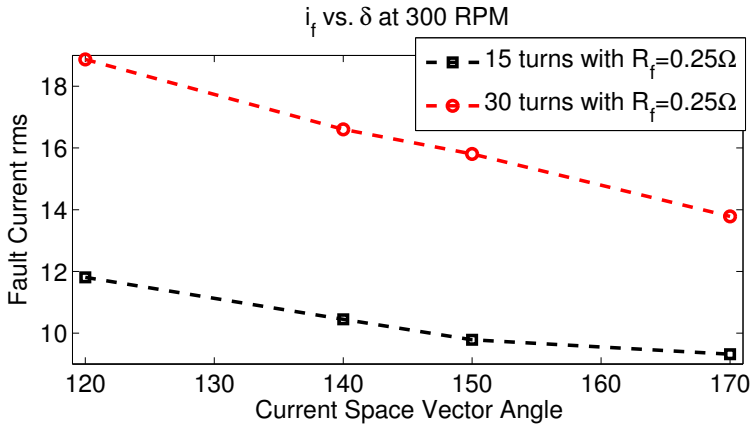

Figure 5.16: Fault current rms value as a function of the current space vector angle at 300 RPM and current space vector magnitude set to 10 A. This data was taken using the 2/5 SPP machine.

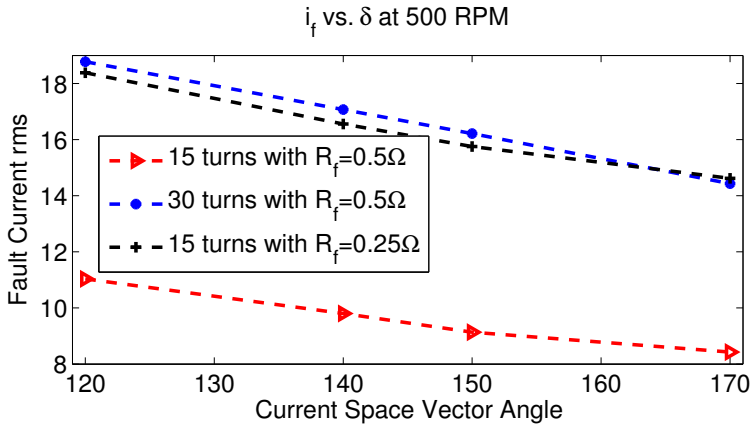

Figure 5.17: Fault current rms value as a function of the current space vector angle at 500 RPM and current space vector magnitude set to 10 A. This data was taken using the 2/5 SPP machine.

$i^* = 10\ A\angle 120^o$, producing 24.7 Nm as shown in figure 4.10(a). However, once the fault occurs, the fault current rms value becomes 18.8 A, as shown in figure 5.17, which is higher than the winding rated value. In order to mitigate the fault and continue safe operation, the controller must increase the angle δ until a safe point in reached. Assuming the new angle be $\delta = 150^o$, the fault current rms becomes 16.2 A and the machine torque drops to 17 Nm. With this new angle, the machine torque output is reduced, but the fault current rms value is kept below the rated value.

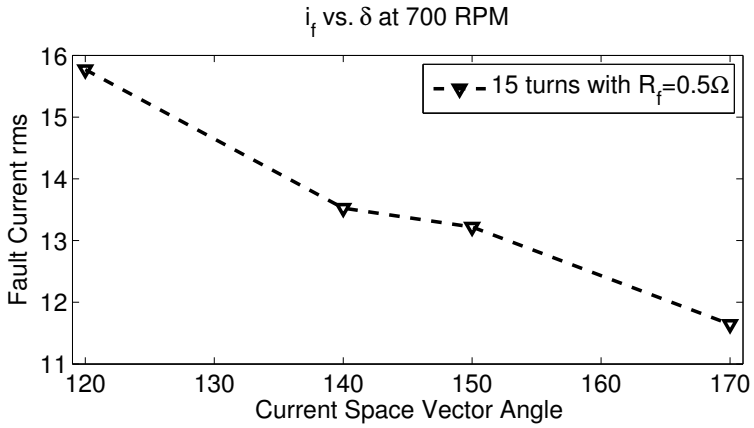

Figure 5.18: Fault current rms value as a function of the current space vector angle at 700 RPM and current space vector magnitude set to 10 A. This data was taken using the 2/5 SPP machine.

The work and results presented above in this section 5.3.4 were performed for the 2/5 SPP single layer PMSM. The same technique was experimentally tested using the double layer 1/2 SPP PMSM. The double layer 1/2 SPP PMSM exhibited the same behavior as the single layer 2/5 SPP PMSM. That is; the reduction of the fault current rms value as the current angle δ increases.

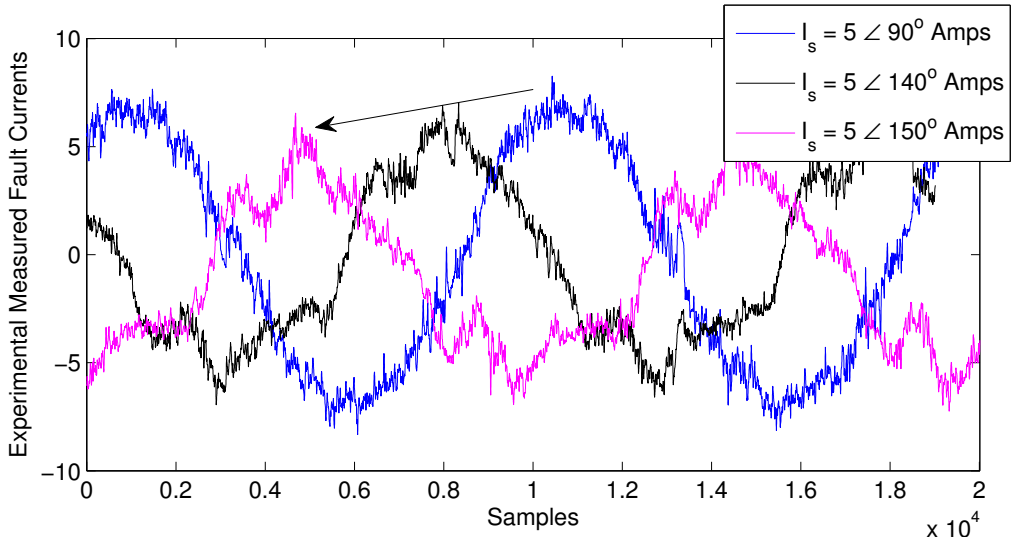

Figure 5.19: Fault current for different current angles, while the current space vector magnitude is kept at constant at 5 A. This data was taken using the 1/2 SPP machine.

In figure 5.20 the rms value for each current angle was calculated, while the magnitude was kept at 5 A. It is important to notice the fault current reduction as the angle δ is increased. This behavior confirms that the fault current can be reduced in the double layer machine as well, regardless of the value of mutual inductances. However, higher reduction of fault current was achieved for the single layer machine.

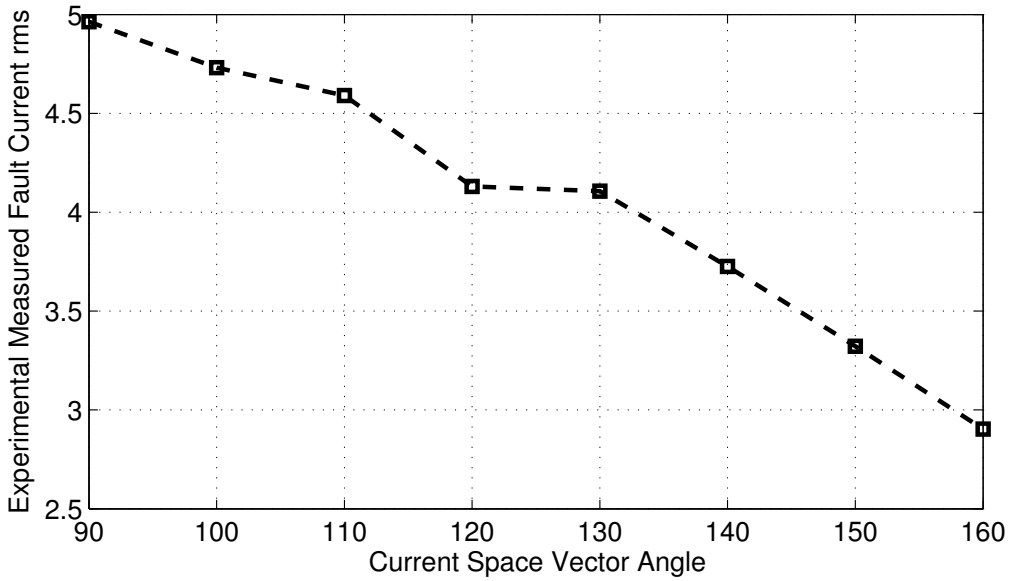

Figure 5.20: Fault current rms value as a function of the current space vector angle at 300 RPM and current space vector magnitude set to 5 A. This data was taken using the 1/2 SPP machine.

Some important remarks about the machines are:

- Higher fault current reduction was noted for the single layer 2/5 SPP PMSM. This is primary due to the machine's lower mutual inductances and the fact the inductance, L_s, is large and limits the fault current.

- Better experimental stability during a fault event was achieved on the single layer machine. High torque and mechanical vibration were noted in the double layer 1/2 SPP PMSM.

Although, the single layer machine showed better fault tolerant characteristics, fault current reduction was achieved in both machines.

5.4 Thermal Relief

A thermal simulation was performed using MotorCAD to show how changes in the current angle δ to mitigate the fault current can relieve the temperature rise caused by the turn-to-turn fault. MotorCAD uses built-in templates that utilize the actual measurements of the machine to generate the simulation geometry. This presents a modeling problem, since it is impossible to generate the exact geometric of the machine under study. The actual geometry of the machine utilized in this work is shown in figure 4.1(a) and it was approximated using the MotorCAD built in templates as shown in figure 5.21(a). The winding configuration inside each of the slots is shown in figure 5.22.

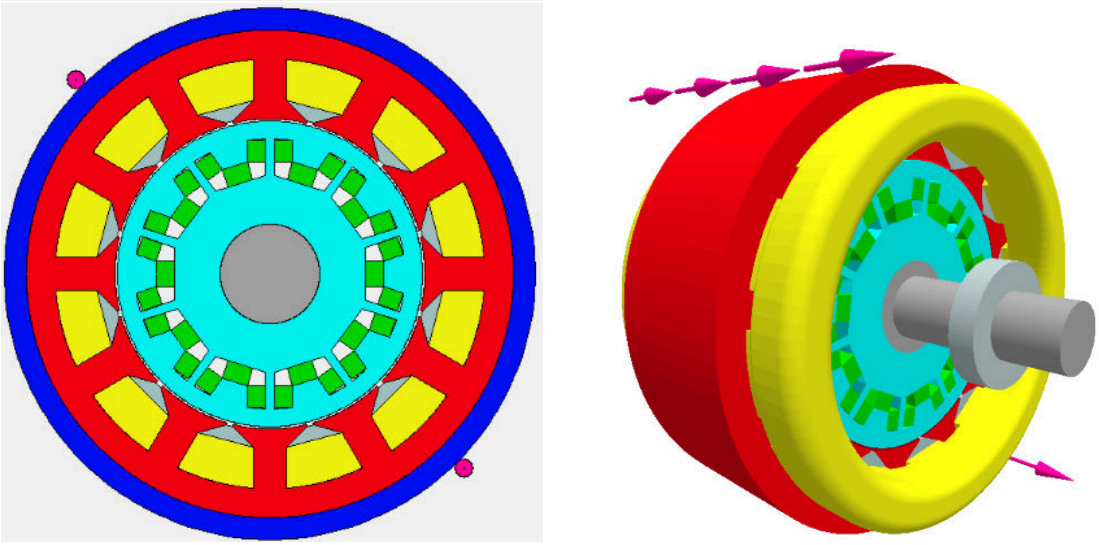

(a) MotorCAD motor geometry front view (b) MotorCAD motor geometry 3D view

Figure 5.21: MotorCAD geometry approximation of the actual machine shown in figure 4.1(a)

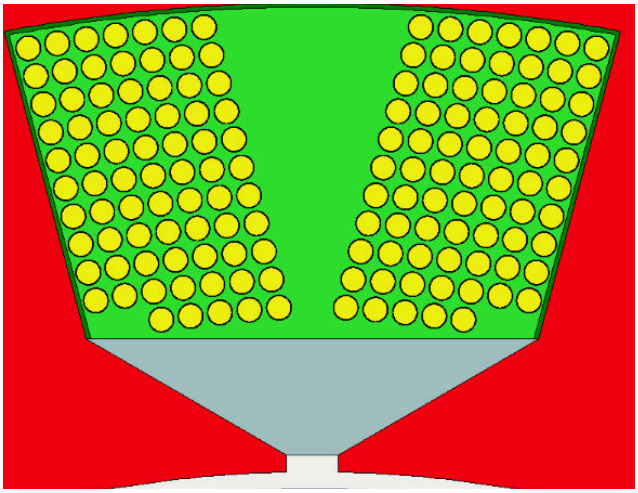

Figure 5.22: MotorCAD slot and winding configuration

MotorCAD is designed to simulate the thermal behavior in healthy machines. Therefore, it is not possible to simulate a PMSM with a turn-to-turn fault in a straight manner. To approximate the behavior of a turn-to-turn faulted three phase machine, a forth winding is added in the simulation. This forth winding is set to represent the loss distribution in the faulted coil A_{af}, while the other three are configure to represent the loss distributions in A_{ah}, B and C winding coils. The loss distribution in the simulations are calculated from the experimentally measured quantities in each specific case.

Because MotorCAD does not provide any means to add a fault, and it is approximated using a fourth phase windings, it is not possible to simulate a transition from healthy to faulted conditions. However, it is possible to simulate each of the operational conditions, for each current angle δ.

The simulations were performed for the $r_f = 0.5\ \Omega$, $N_f = 15$ turns at 300 RPM fault case, for the different current angles. To study the temperature rise and fall, the machine was simulated running at the corresponding load for 60 *sec*, followed by a 60 *sec* no-load condition. The results of this simulations are shown in fig. 5.23; (H 120d) stands for

healthy at $\delta = 120^o$, (R05 120d) stands for faulted with $r_f = 0.5\ \Omega$ at $\delta = 120^o$, the same nomenclature is used for the rest of the cases. The loading condition for each angle is shown in fig. 4.10(a); where the torques corresponding to of the each angles are the following: ($\delta = 120^o \rightarrow 24.7\ Nm$), ($\delta = 140^o \rightarrow 21.3\ Nm$) and ($\delta = 150^o \rightarrow 17\ Nm$).

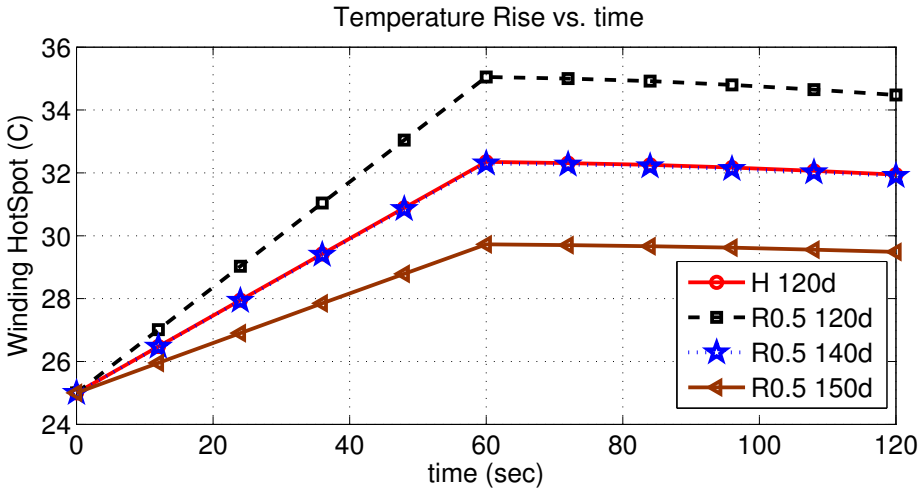

Figure 5.23: Thermal simulation for various current angles, healthy case and the $r_f = 0.5\ \Omega$, $N_f = 15$ turns at 300 RPM case. The current space vector magnitude is kept constant at 10 A for all simulations.

For this fault, operating at $\delta = 140^0$, instead of the MTPA angle $\delta = 120^o$ is better in terms of thermal stress. Operating with this angle reduces the output torque by only 3.4 Nm. However, the fault current is kept within acceptable limits, with a 10% drop as shown in figure 5.14, and the operating temperature is restored to nominal conditions, as shown in fig. 5.23.

5.5 Chapter 5 Remarks

- Analytical sensitivity calculations showed that the fault current becomes susceptible to the current angle δ, as δ increases into the field weakening region. Equation 5.3 shows how the line current in the faulted phase and the back emf contribute toward

the fault current. The induced current by the back emf can be controlled using the line current angle.

- Various experimental results demonstrated that changes in the current angle δ can reduce the fault circulation current, reducing the fault power losses and hence the operating temperature. The idea is to operate the faulted machine in the field weakening region, even if the speed is below base, to reduce the voltage induced in the faulted area.

- Thermal simulations demonstrate the thermal relief when the machine operated in field weakening below nominal speed, as a fault current reduction remedial technique.

Chapter 6

Proposed Methodology for Fault Mitigation

This chapter discusses a fault mitigation technique and its effectiveness in reducing the fault current. Once a fault takes place in the stator windings there is a high possibility of having overcurrent in the faulted area. This over-current condition has a negative effect on the motor performance and its operating temperature. It is essential to mitigate these effects to avoid a catastrophic event. The key objectives of this technique are denoted as follows:

- Maintain healthy current levels across the lines and the fault circuit loop.
- Keep all motor components operating under the maximum allowed temperature.
- If conditions allow continue operation under limited torque conditions.

The proposed method uses the current angle δ to mitigate the fault; and it also limits the machine capacity to avoid over current conditions. Figure 6.1 shows the space vector plane for the PMSM, it demonstrates how the increasing current angle δ cancels some of the flux linkage due to the magnets λ_{pm}. The induced voltage in the faulted coil depends on the total flux linkage, $v_{emf} = \omega_e \lambda_{total}$. As the angle increases, i_d becomes more negative and produces a flux λ_d that opposes the magnet flux λ_{pm}. The flux cancelation effect reduces the fault current due to the reduction of induced voltage.

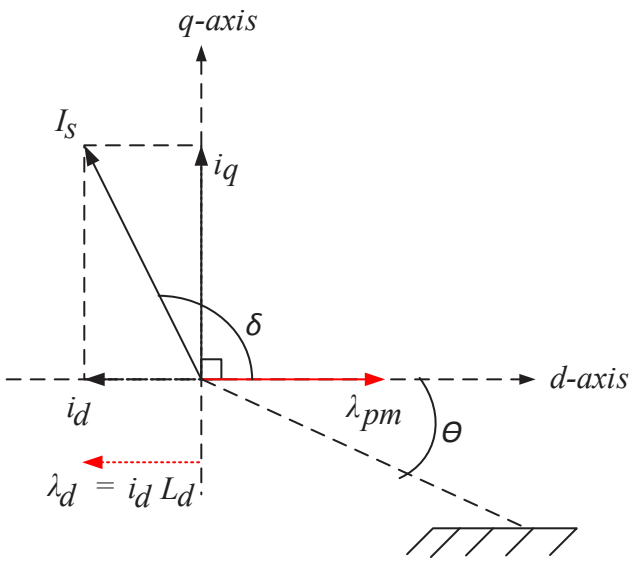

Figure 6.1: Space vector plane, dq axes

A fault mitigation technique relies on the ability to detect and estimate the fault conditions. A turn-to-turn fault creates unbalanced operating conditions that serve as indicators for fault detection purposes.

6.1 Fault Detection and Fault Current Estimation

In this work, fault detection is made using the variations in the voltage space vector, $\vec{v}_d = v_d + jv_q$. As stated in the introduction this topic has attracted a lot of work and contributions. Here we base the method on [24] and [25]. The effects of the fault in the voltage vector are analyzed using the model shown in equation 3.7. This model is simplified by neglecting the mutual inductances between the phases. A valid assumption, since a single layer fault tolerant PMSM with negligible mutual inductances is used for experimental validation. To derive the space vector form, equation 3.7 is transformed into the dq rotor frame of reference; the direct and quadrature axes voltages are shown in equations 6.1 and 6.2.

$$
\begin{aligned}
v_d = 2/3(i_d r_s + e_d + L_d \frac{di_d}{dt} \\
-i_f r_{af} \sin(\theta) - \frac{di_f}{dt}(L_{af} + M_{a_h a_f}) \sin(\theta)) \\
= \bar{v}_d + \tilde{v}_d
\end{aligned}
\tag{6.1}
$$

$$
\begin{aligned}
v_q = 2/3(i_q r_s + e_q + L_q \frac{di_q}{dt} \\
-i_f r_{af} \cos(\theta) - \frac{di_f}{dt}(L_{af} + M_{a_h a_f}) \cos(\theta)) \\
= \bar{v}_q + \tilde{v}_q
\end{aligned}
\tag{6.2}
$$

where $\bar{v}$ is the expected healthy value and $\tilde{v}$ is de variation cause by the fault.

The fault current fundamental value depends on the induced emf voltage and the line current commands, which are relatively sinusoidal. By considering only the fundamental component of i_f, of the form $i_f = |i_f| \cos(\theta)$, equations 6.3 and 6.4 are determined. These equations only show the variations on the voltage space vector due to the fault.

$$
\begin{aligned}
\tilde{v}_d = \frac{1}{3}\{|i_f| r_{af} \sin(2\theta) \\
+ |i_f| (L_{af} + M_{a_f a_h})(\cos(2\theta) - 1)\}
\end{aligned}
\tag{6.3}
$$

$$
\begin{aligned}
\tilde{v}_q = \frac{1}{3}\{|i_f| r_{af} + |i_f| r_{af} \cos(2\theta) \\
+ |i_f| (L_{af} + M_{a_f a_h}) \cos(2\theta)\}
\end{aligned}
\tag{6.4}
$$

A turn-to-turn fault introduces oscillations of double angle and a dc offset shift on the axes voltages. The oscillations on the voltage vector are not a practical indicator for fault

detection purposes. A more practical approach is to use the dc offset shift, as a simple digital filter in the controller can extract the information. Figure 6.2 shows the dc offset shift tendency for the voltage vector. Experimental and finite element data agree with the vector movement and tendency as the fault progresses.

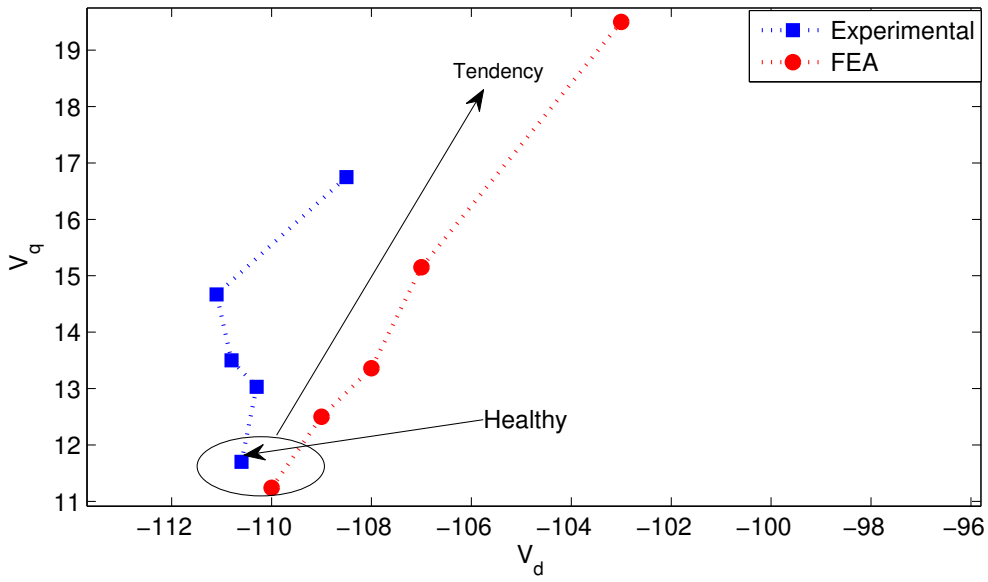

Figure 6.2: Changes in the voltage space vector for different fault conditions at 300 RPM with $10A\angle 120^o$ for the 2/5 SPP machine. Starting from healthy, then moving to r_f = 0.5 Ω@ 15 $turns$, r_f = 0.25 Ω@ 15 $turns$, r_f = 0.5 Ω@ 30 $turns$, and finalizing with r_f = 0.25 Ω@ 30 $turns$

Estimates of the parameters of a fault, N_f and r_f, are used to determine the severity of the fault and the amount of fault circulating current. N_f and r_f are estimated based on the position of the voltage vector, as shown in figure 6.2, it takes a particular position depending on N_f and r_f.

As a fault progresses the tendency of the voltage space vector is to increase more on the q-axis than in the d-axis, as shown in figure 6.2. This behavior observed in FEA and experiments validates equation 6.3 and 6.4, since for the machine under study $r_{af} >> (L_{af} + M_{af}a_h)$ and the dc offset in the q-axis is proportional to $|i_f| r_{af}$.

In this work, $\tilde{v}_q$ is used to detect and estimate the fault, given that the dc shift of the vector is more significant in the q-axis. As discussed in section 2.4.1.3, high performance controllers use lookup tables to control the machine for different operating conditions. These tables are generated by characterizing the PMSM over the operating range prior to the development of the control algorithm. Therefore, the controller has information and predictions of the expected axes voltages, for all the desired operating range of the motor. In this work we treat any persistent discrepancy in v_q as a turn-to-turn fault; and the magnitude of this discrepancy is used to estimate N_f and r_f. Figure 6.3 shows the detection technique experimental performance, when a 0.5 Ω fault is inserted across 15 turns of winding A. The delay between the fault insertion point and the detection time is due to the heavy moving average filtering of v_q. Detection, using the mean of $\tilde{v}_q$, requires a heavy moving average filtering to remove the controller noise, as shown in figure 6.3.

The decision to rise the fault flag is only taken using the mean of $\tilde{v}_q$ when the machine is operating under steady state conditions. This is to avoid false alarms during transitory operation.

Once, N_f and r_f are estimated the fault current magnitude is estimated using the system model on figure 3.2. This model can be solved for $|i_f|$ as follows,

$$\begin{aligned} R_f &= r_f + r_{af} \\ X &= R_f^2 + (\omega L_{af})^2 \end{aligned} \tag{6.5}$$

$$\begin{aligned} a = i_d r_{af} R_f + \Delta\lambda_{pm}\omega R_f - i_q\omega(L_{a2} - M_{a_1a_2})R_f \\ +\omega^2 L_{af} i_d (L_{a2} - M_{a_1a_2}) + \omega L_{af} i_q r_{af} \end{aligned} \tag{6.6}$$

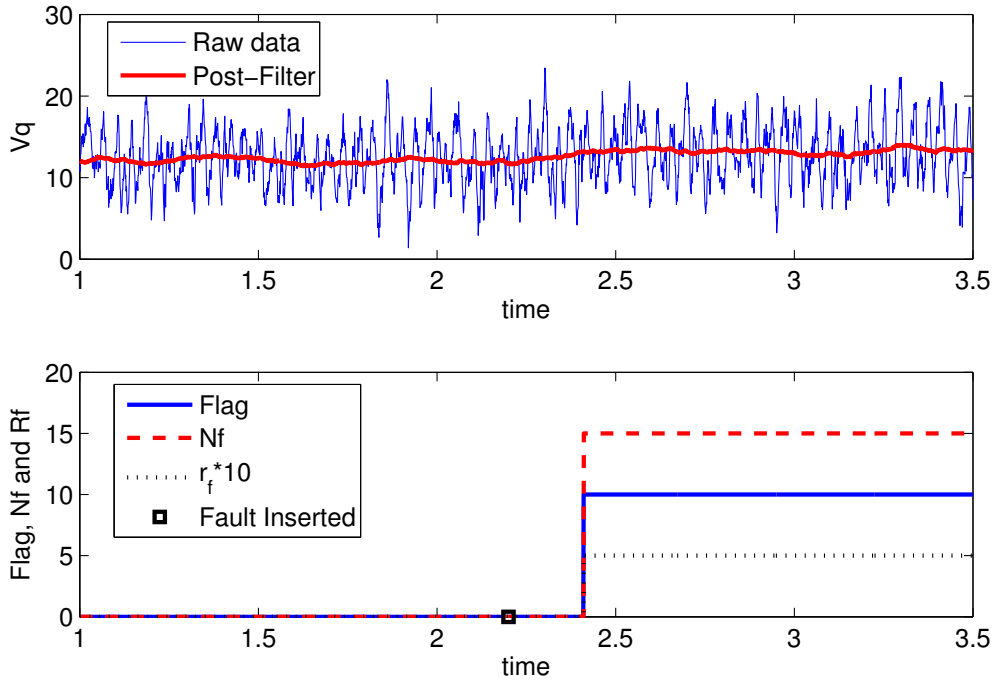

Figure 6.3: Detection experiment, healthy operation progressing into a $r_f = 0.5\ \Omega$ fault across 15 *turns* of the winding. All the testing was performed in the single layer 2/5 SPP machine.

$$\begin{aligned} b = i_d\omega(L_{a2} - M_{a_1a_2})R_f + i_q r_{af} R_f - \omega L_{af} i_d r_{af} \\ -\omega^2 L_{af}\Delta\lambda_{pm} + \omega^2 L_{af} i_q (L_{a2} - M_{a_1a_2}), \end{aligned} \tag{6.7}$$

$$|i_f| = \sqrt{\left(\frac{a}{X}\right)^2 + \left(\frac{b}{X}\right)^2}. \tag{6.8}$$

Figure 6.4 shows the solution of equation 6.8 for $r_f = 0.5\ \Omega$ fault across 15 *turns*, while the motor is operating at 300 RPM with a $|i_s| = 10\ A$. The solution of equation 6.8 in figure 6.4 closely resembles the experimentally measured current shown in figure 5.14.

The voltage movement tendency technique, presented on figure 6.2 and used to detect and estimate the fault parameters in the 2/5 SPP machine in figure 4.1(a), was also tested on the 1/2 SPP machine in figure 4.1(b). Different fault scenarios were used to study the

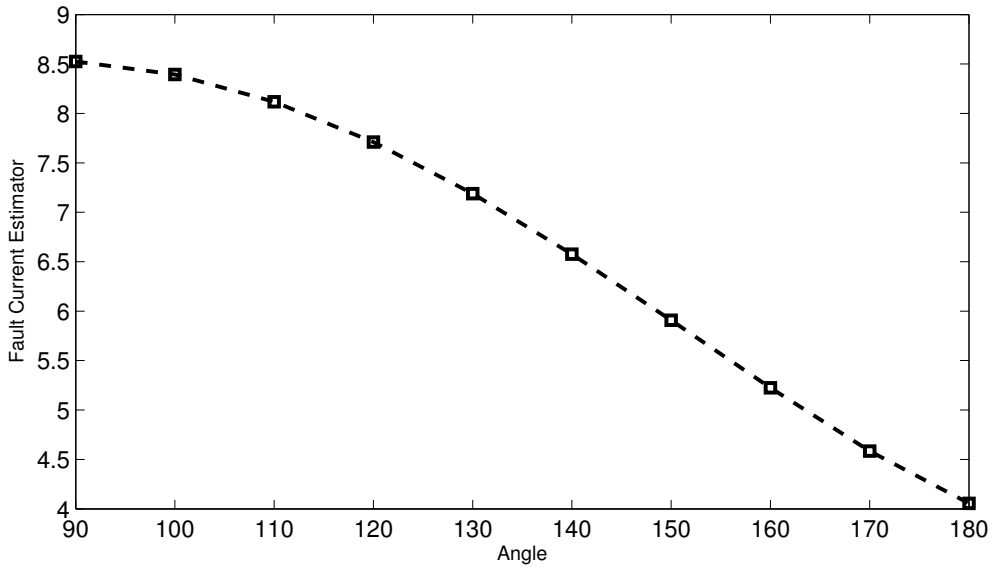

Figure 6.4: Fault current estimator for a $r_f = 0.5\ \Omega$ fault across 15 *turns* of the winding, motor operating at 300 RPM with a $|i_s| = 10\ A$. All the testing was performed in the single layer 2/5 SPP machine.

voltage vector tendency using finite elements analysis as shown in figure 6.5. On this double layer machine the voltage vector showed considerably measurable voltage changes in both axes. These voltage changes are used to detect and estimate the fault, in the same way it was performed on the 2/5 SPP single layer machine in figure 6.3.

The double layer 1/2 SPP machine showed more variation on the d-axis than on the q-axis. Contrary to the 2/5 SPP single layer machine where the q-axis variation dominated the variations on the d-axis. This behavior change is attributed to the higher self and mutual inductances in the machine. The different parameters for both machines are presented in tables 4.2 and 4.3.

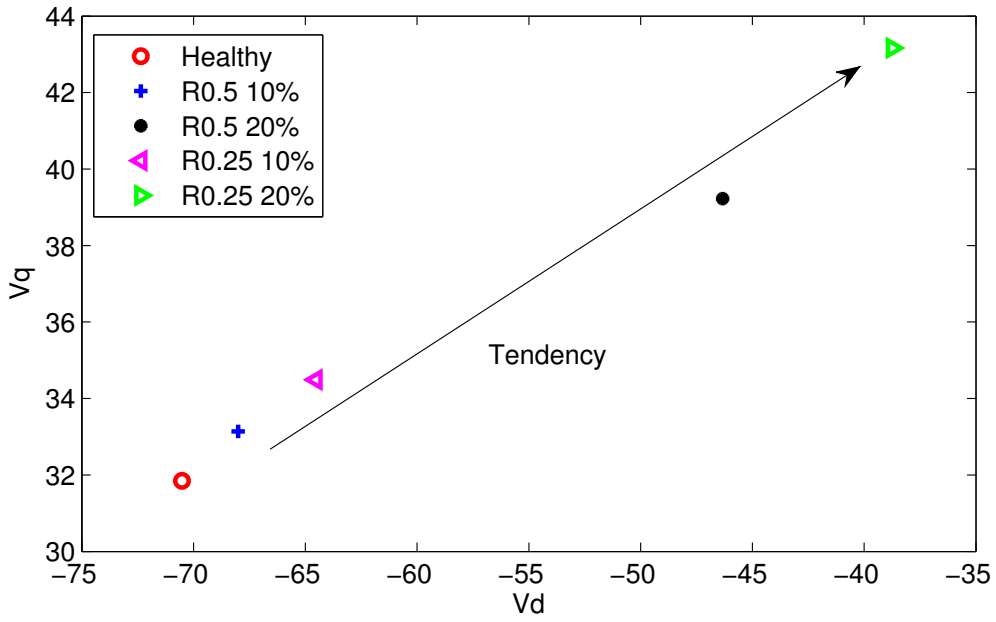

Figure 6.5: Changes in the voltage space vector for different fault conditions at 300 RPM with $10A\angle 140^o$ for the $1/2$ SPP double layer machine. Starting from healthy, then moving to $r_f = 0.5\ \Omega$@ 15 $turns$, $r_f = 0.25\ \Omega$@ 15 $turns$, $r_f = 0.5\ \Omega$@ 50 $turns$, and finalizing with $r_f = 0.25\ \Omega$@ 50 $turns$

6.2 Control Algorithm and Experimental Results

Based on the results shown in previous chapters, a fault mitigation technique is proposed. Upon detection of a fault, the motor drive controller must; limit the operating speed, restrict the amount of torque the machine can develop by restricting the line current and start field-weakening at speed bellow nominal to reduce the amount of induced voltage in the fault.

The mitigation algorithm is shown in figure 6.6. It was developed to mitigate and gain some degree of control over the fault current. The algorithm checks for the RMS value of i_f and if it is larger than a predetermined value, it reacts by applying a current vector that weakens the magnets field, known as flux nulling. In the case, the commanded current do not permit the limitation of i_f, the algorithm will automatically de-rate or lower the commanded $|i_s|$.

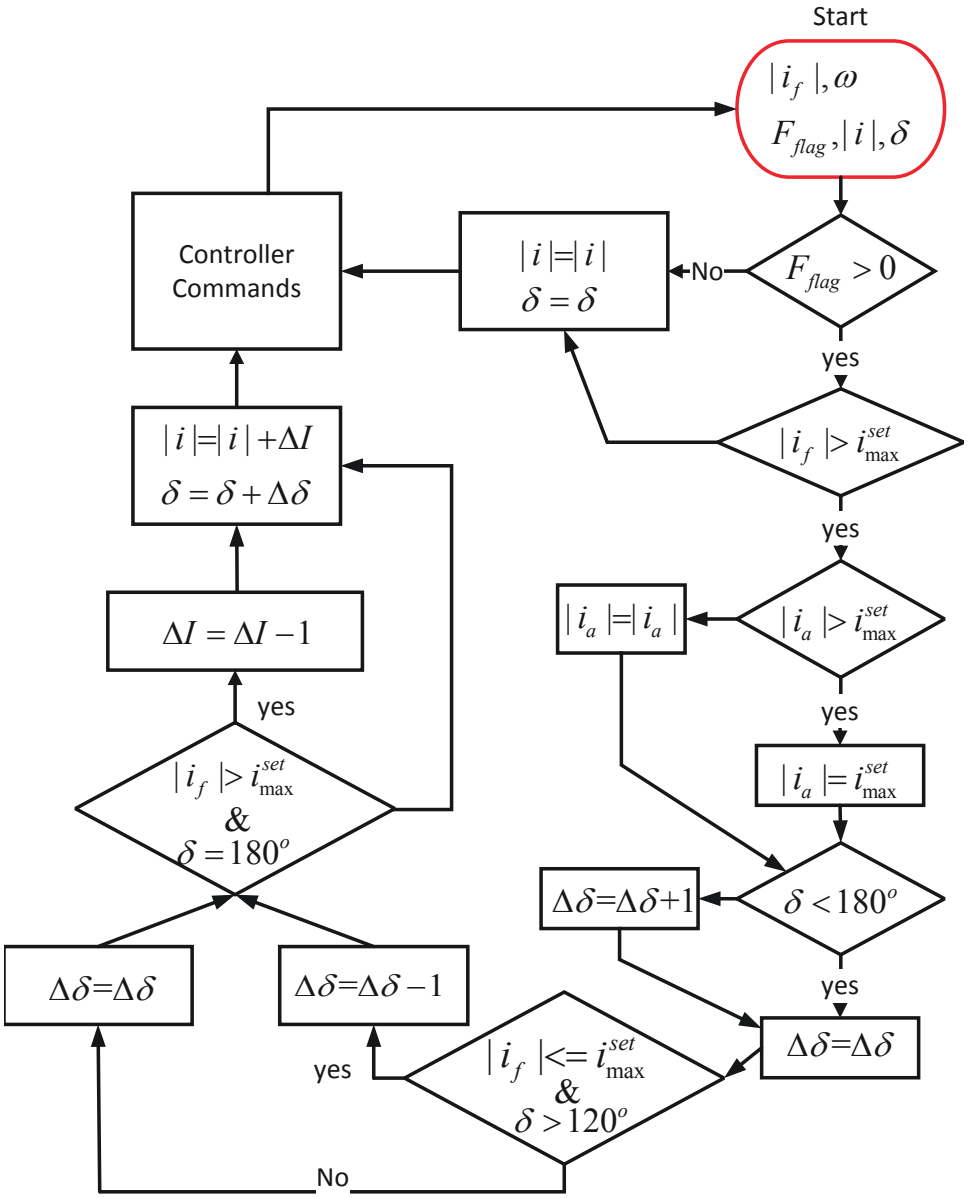

Figure 6.6: Fault mitigation algorithm, enables the limitation of i_f by δ and $|i_s|$.

Figure 6.7 shows the full controller used to collect the experimental data. The fault resistor is inserted at a random time using a switch box. This box connects r_f to the desired number of turns in the fault N_f.

The proposed algorithm is tested using two r_f resistances across a 15 and 30 turn fault.

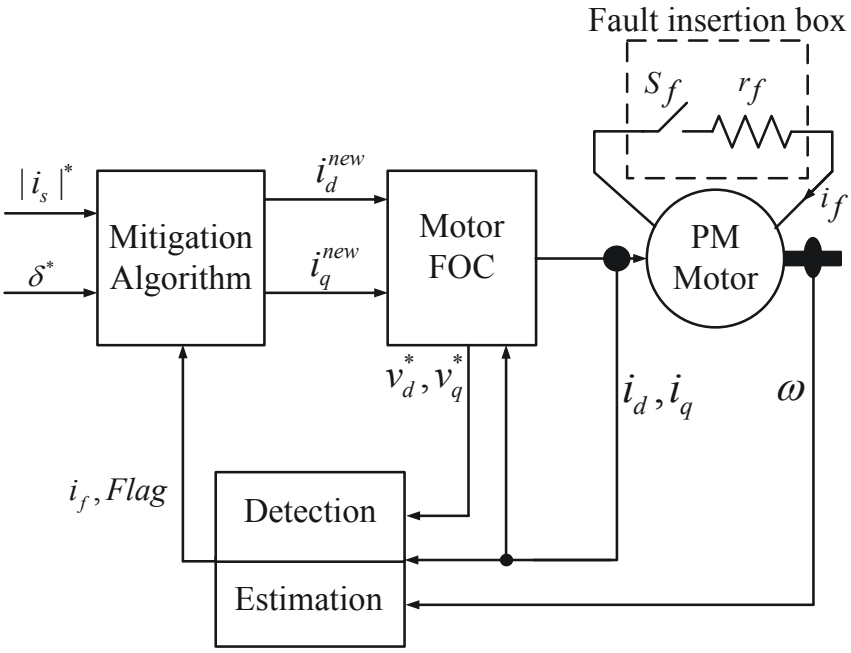

Figure 6.7: Motor controller including detection, estimation and mitigation

6.3 Experimental case: A 0.5 Ohms fault across 15 turns

In this experimental case, the mitigation technique, the detection and estimation procedures were tested using a $r_f = 0.5\ \Omega$ across 15 *tuns* fault. The experiment starts with the PM motor operating at 300 RPM with $i_s = 10\angle 120^o$ under healthy conditions. Then the fault is inserted and the speed is increased to test the controller's ability to maintain the fault current magnitude bellow a predetermined value. In this work the predetermined maximum $i_{\max}^{set}$ is set to 10 A, which is 40% of the rated winding current. The experiment is finalized by a decreasing the speed, to test the controller's ability to restore δ when the conditions allow.

As seen in figure 6.8 the mitigation algorithm successfully limited the fault current to the

desired maximum level of 10 A. For this fault case as shown in figure 6.8(d), only δ alterations were necessary to kept the current within the limit. No limitation on the commanded line current magnitude were applied for this fault case.

6.4 Experimental case: A 0.25 Ohms fault across 15 turns

The experiment performed in section 6.4 was implemented for a fault of $r_f = 0.25\ \Omega$ across 15 $tuns$, and the results are shown in figure 6.9.

Due to the severity of this case, the algorithm altered δ and $|i_s|$, in order to keep the fault current within the allowed limit. For this fault, even a full flux weakening at $\delta = 180^o$ did not lower i_f to $10A$. Therefore, the algorithm automatically de-rated the amount commanded line current, as it is shown in figure 6.9(d).

Encircled in figure 6.9(c) is a particular behavior in the detection of this $r_f = 0.25\ \Omega$ fault. Because the heavy filtering in v_q, the detection algorithm first detects a $r_f = 0.5\ \Omega$ before it detects the correct fault of $r_f = 0.25\ \Omega$. This behavior occurs because the voltage vector transitions through the $r_f = 0.5\ \Omega$ vector position before it reaches its final faulted vectorial position. The vectorial movement and tendency are shown in figure 6.2.

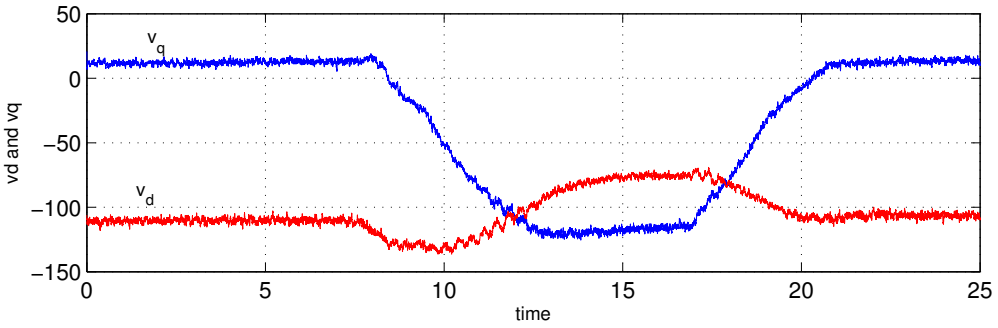

(a) v_d and v_q response to the operating conditions.

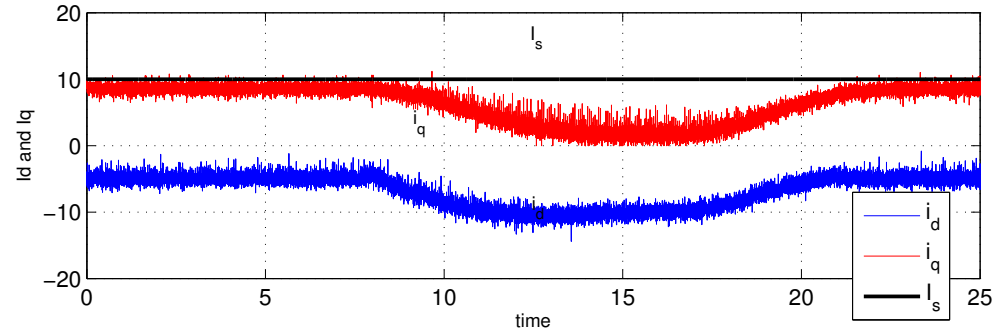

(b) i_d, i_q and $|i_s|$ response to the operating conditions.

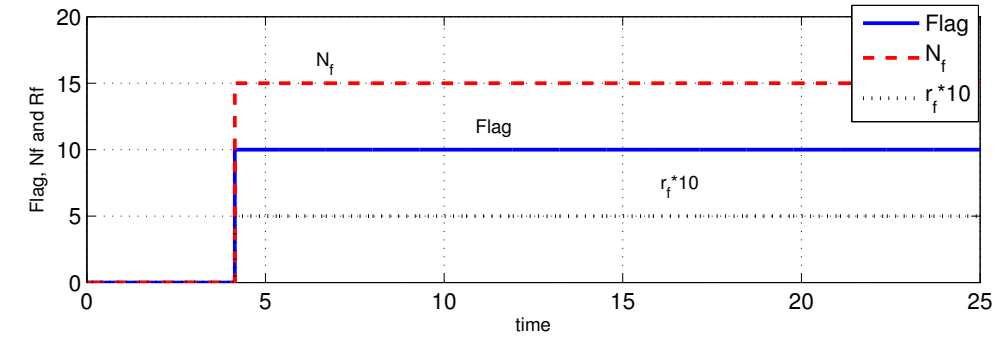

(c) Number of faulted turns, fault flag indicator and r_f estimation.

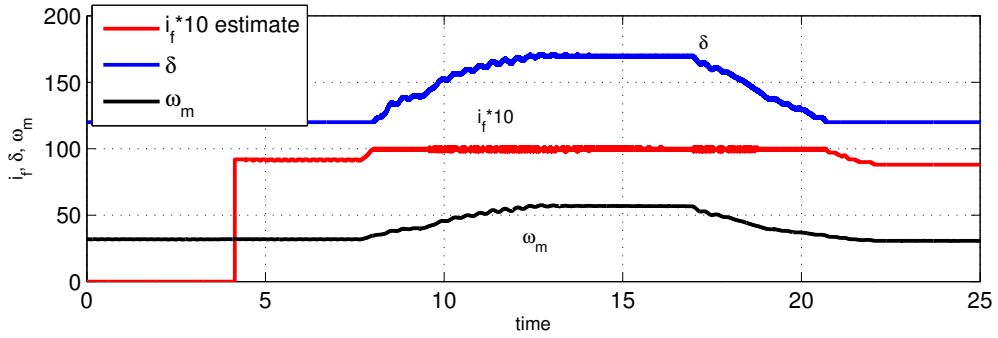

(d) Response to a fault, δ, i_f estimation and mechanical speed ω_m.

Figure 6.8: Experimental case $r_f = 0.5\ \Omega$ across 15 *turns*, including detection, estimation and fault current mitigation.

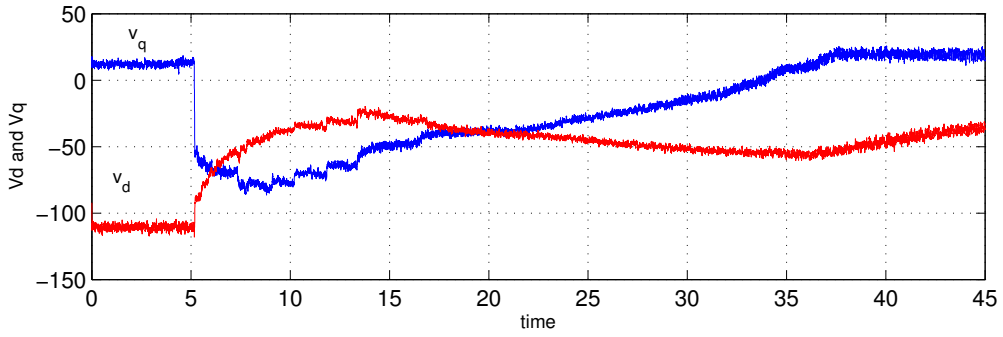

(a) v_d and v_q response to the operating conditions.

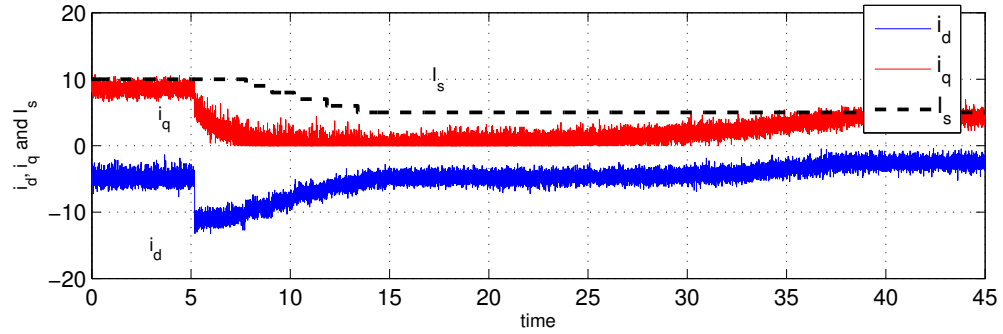

(b) i_d, i_q and $|i_s|$ response to the operating conditions.

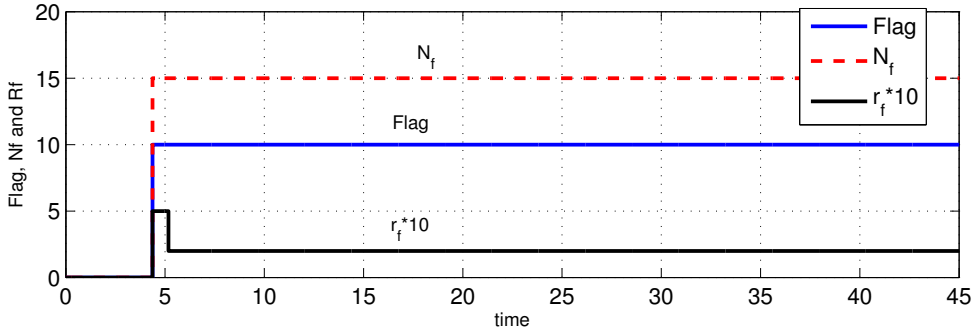

(c) Number of faulted turns, fault flag indicator and r_f estimation.

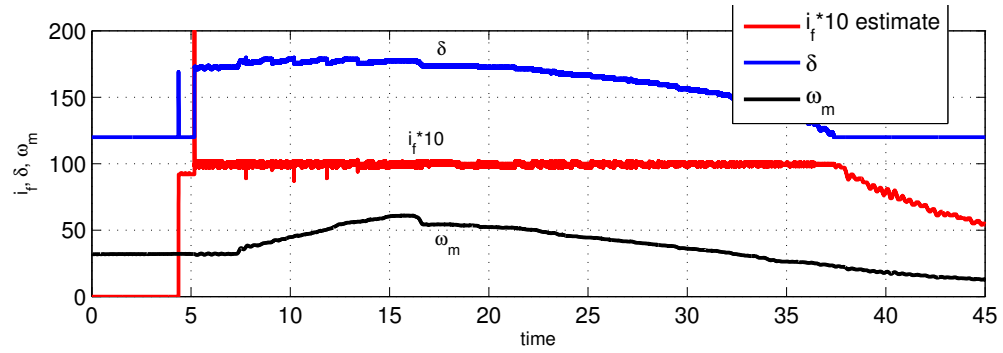

(d) Response to a fault, δ, i_f estimation and mechanical speed ω_m.

Figure 6.9: Experimental case $r_f = 0.25\ \Omega$ across 15 *turns*, including detection, estimation and fault current mitigation.

Chapter 7

Conclusion

The proposed mitigation algorithm presented in this work and sumarized in figure 6.6 successfully regulated the fault current, limiting it to a predetermined value. Limiting the amount of fault current, lowers the power losses and the dissipated heat. Heat is the main contributor to fault propagation and deterioration of a PMSM winding. Controlling the amount of heat, by controlling the power losses, can extend the post-fault life span of a PMSM.

The goal of the technique is to act upon a fault in its early stages, while it is an incipient fault, before it becomes a highly severe fault. As shown in figures 6.8 and 6.9, it is possible to control and limit i_f for incipient faults by applying field weakening at low speeds and/or derating the lines current. This controllability, allows the controller to auto-protect and attempt to delay the propagation of the fault. Although the method is intended for incipient faults, it is also applicable for severe faults to minimize the risk of a catastrophic even.

Mitigation is the main focus of this in this research; however, a mitigation technique is as good as the detection and estimation algorithm it relying upon. Quick detection of a fault is vital to ensure that the fault propagation is stopped or delayed by the mitigation technique. A simple, but effective way to detect the fault is presented in section 6.1. As shown in figure 6.2 it uses the deviations from the expected value of the voltage space vector as an early sign of a fault. The tendency and how far the voltage vector moves away from the expected value are used to estimate the parameters of the fault. This technique was successfully tested for

two fault cases in figures 6.3, 6.8 and 6.9.

Throughout the experimentation process excellent control performance was maintained, as it is demonstrated in figures 5.10 and 5.11. Having a robust controller capable of controlling the line currents during a fault event is vital for the proposed technique to properly work. The technique relies on the controller to inject currents at the correct angle and magnitude, in order to minimize fault current oscillations and mitigate the fault.

APPENDIX

APPENDIX A

DSP Controller and Data Handling

Experimental procedures and testing where performed using the system shown in figure 2.4. Its main components are:

- An industrial DC/AC inverter, fed by an uncontrolled diode rectifier.
- An ESI DSP system board, equipped with the Texas Instruments 32 bit Delfino TMS320F28335.
- Peak CAN adapter, CAN BUS to USB line converter, used to transfer data from the DSP unit to a computer equipped with LabView and the peak CAN data management software.

This chapter deals with the details about programming the DSP unit and data logging structures.

Figure A.1 show the general execution structure for a DSP unit. The two main components of the structure are the void main(void) function and the interrupt. The void main(void) function is where all the submodules, like the Analog to Digital Converter, the PWM enable, the encoder reading module and interrupt timers are set. Once all modules are properly set, the rest of the code, including the control algorithm, resides on the interrupt function. Note that the void main(void) function can handle several interrupts simultaneously and executed based on a priority flag. The basic DSP controller configuration show in figure A.1 is based on a single interrupt.

DSP units operate in discrete time, and the step change is set by a counter that runs at the DSP clock speed. This time change is known as the interrupt speed. For example the TMS320F28335 DSP has a internal clock speed of 150 MHz, but the time step can be set to a lower value.

In this work the interrupt or step time is set equal to the switching frequency of the PWM signals. In this way, every interrupt triggers all the submodules to gather all the feedback signals, update all PWM signals and transmit available information using the CAN BUS.

Figure A.2 shows a detailed programming structure, that expands the the interrupt function shown in figure A.1. The FOC controller shown in figure 2.7 and 2.8 is implemented using the DSP structure shown in figure A.2. All proportional integral controllers were transform to the discrete domain in order to close the current loops.

Instead of placing external measuring equipment, to measure the line currents, the rotor position and the commanded voltages, the inherent system sensors and estimators were utilized. In this work the technique was utilized to demonstrated that using the inherent system sensors is as accurate as using high end measurement devices. Differences between both techniques were studied in detail in [44]. Figure A.3 shows the information flow from the feedbacks signals to the data logging computer. Experimental data can be recorded using the LabView interphase and the Peak CAN software.

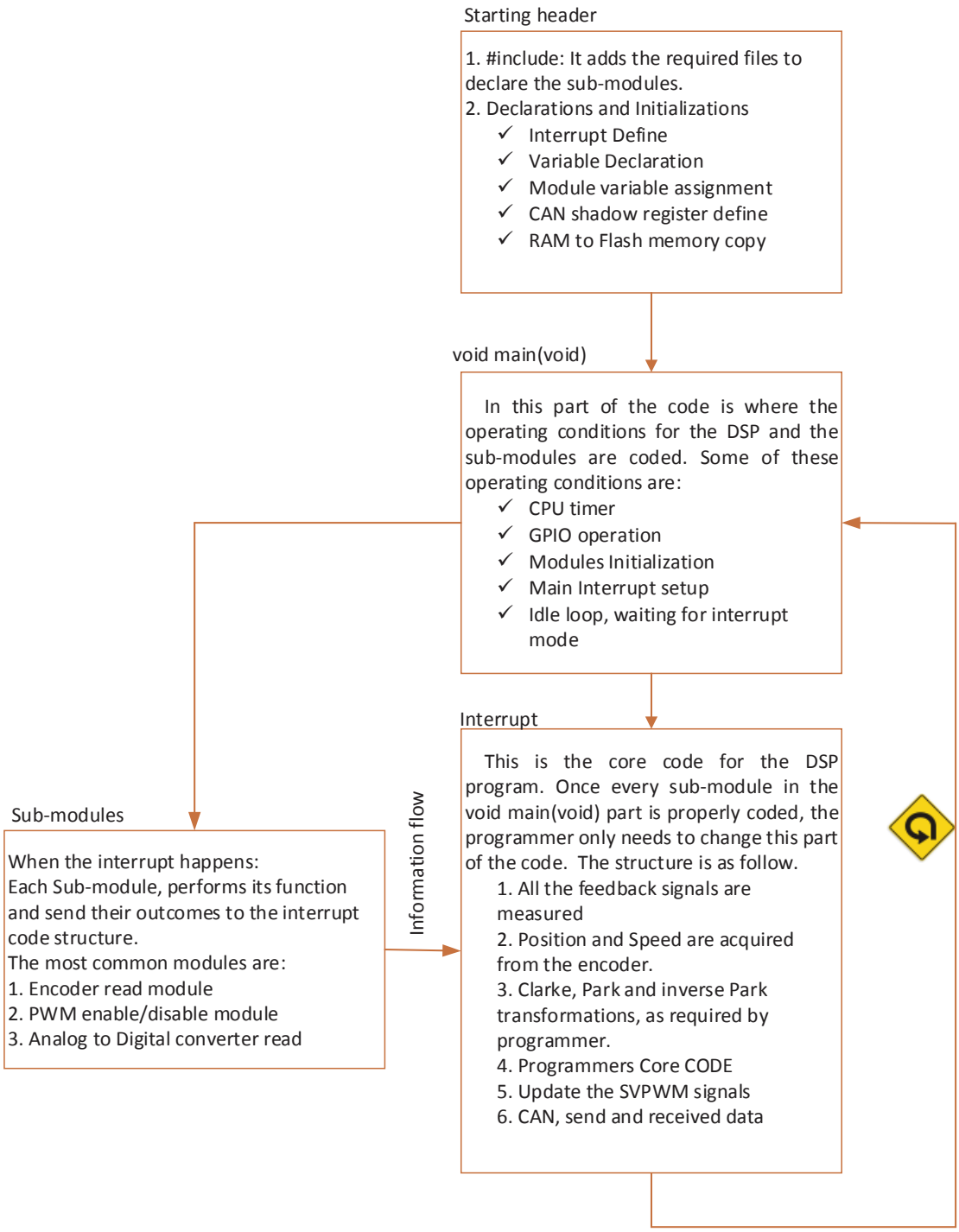

Figure A.1: Generalized DSP execution mode, shown sequence of operation and interrupt.

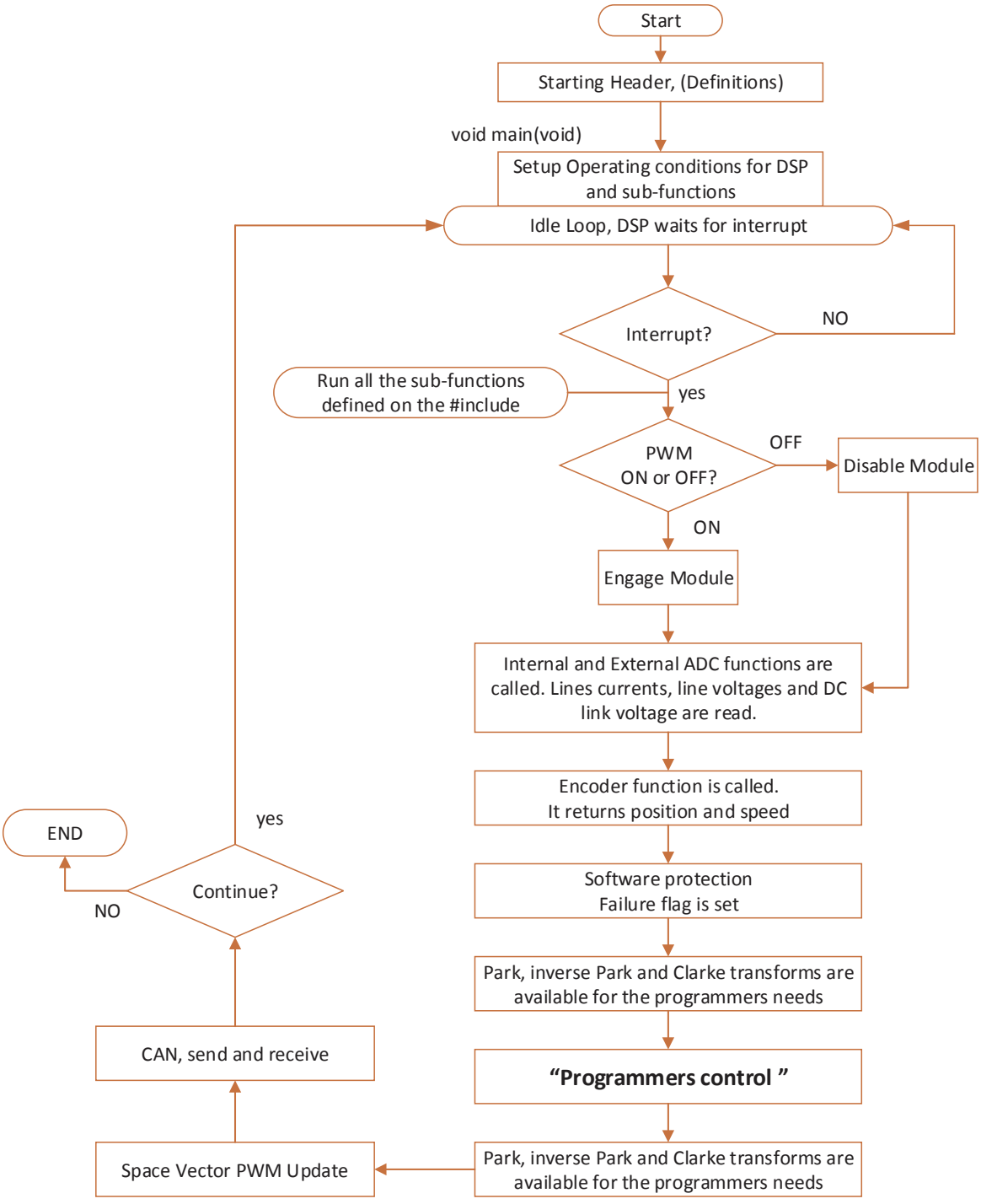

Figure A.2: ESI DSP system board specific case, C++ coding structure.

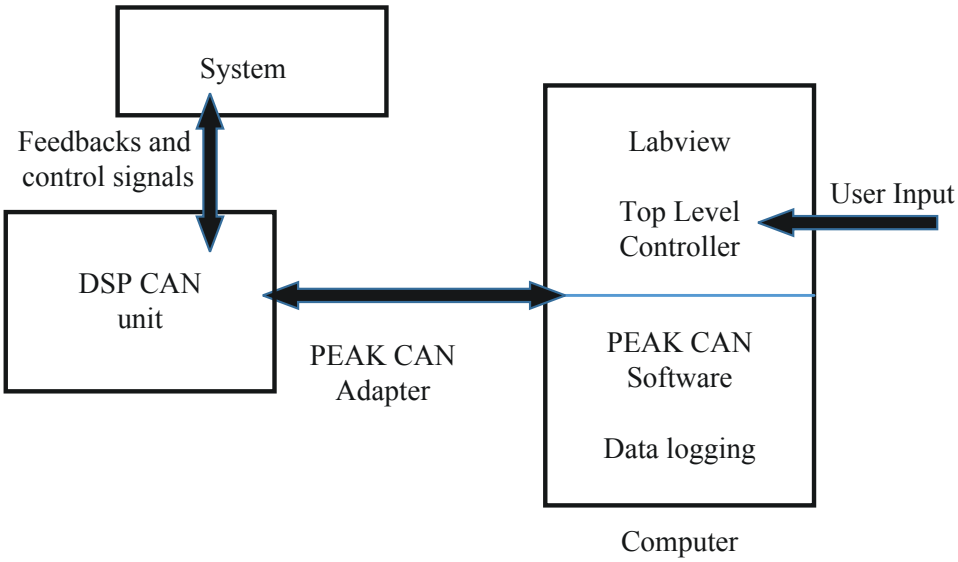

Figure A.3: DSP and data logging computer information flow.

BIBLIOGRAPHY

BIBLIOGRAPHY

[1] J. Neely and E. Strangas, "Fault types and mitigation techniques of PMAC machines," in *2006 IEEE International Conference on Electro/information Technology*, 2006, pp. 97–102.

[2] B. Welchko, T. Lipo, T. Jahns, and S. Schulz, "Fault tolerant three-phase AC motor drive topologies; a comparison of features, cost, and limitations," in *Electric Machines and Drives IEEE International Conference*, vol. 1, 2003, pp. 539–546 vol.1.

[3] K. H. Kim, D.-U. Choi, B. G. Gu, and I. S. Jung, "Fault model and performance evaluation of an inverter-fed permanent magnet synchronous motor under winding shorted turn and inverter switch open," *Electric Power Applications, IET*, 2010.

[4] S. Bolognani, M. Zordan, and M. Zigliotto, "Experimental fault-tolerant control of a PMSM drive," *IEEE Transactions on Industrial Electronics*, 2000.

[5] F. Aghili, "Fault-tolerant torque control of BLDC motors," *IEEE Transactions on Power Electronics*, vol. 26, no. 2, pp. 355–363, 2011.

[6] F. Baudart, B. Dehez, F. Labrique, E. Matagne, D. Telteu, and P. Alexandre, "Control strategy with minimal controller reconfiguration of fault tolerant polyphase PMSM drives under open circuit fault of one phase," in *2010 XIX International Conference on Electrical Machines (ICEM)*, 2010, pp. 1–6.

[7] R. Spee and A. Wallace, "Remedial strategies for brushless DC drive failures," in *Conference Record of the 1988 IEEE Industry Applications Society Annual Meeting*, 1988, pp. 493–499 vol.1.

[8] N. Bianchi, S. Bolognani, M. Zigliotto, and M. Zordan, "Innovative remedial strategies for inverter faults in IPM synchronous motor drives," *IEEE Transactions on Energy Conversion*, vol. 18, no. 2, pp. 306–314, 2003.

[9] O. Wallmark, L. Harnefors, and O. Carlson, "Control algorithms for a fault-tolerant PMSM drive," *IEEE Transactions on Industrial Electronics*, vol. 54, no. 4, pp. 1973–1980, 2007.

[10] W. O., H. Lennart, and O. Carlson, "Control algorithms for a fault-tolerant PMSM drive," *IEEE Transactions on Industrial Electronics*, vol. 54, no. 4, pp. 1973–1980, 2007.

[11] A. Mohammadpour, A. Gandhi, and L. Parsa, "Design and control of fault-tolerant permanent magnet machines," in *2013 IEEE Workshop on Electrical Machines Design Control and Diagnosis (WEMDCD)*, 2013, pp. 108–116.

[12] I. Jeong, B. J. Hyon, and K. Nam, "Dynamic modeling and control for SPMSMs with internal turn short fault," *IEEE Transactions on Power Electronics*, vol. 28, no. 7, pp. 3495–3508, 2013.

[13] B.-G. Gu, J.-H. Choi, and I.-S. Jung, "A dynamic modeling and a fault detection scheme of a PMSM under an inter turn short," in *2012 IEEE Vehicle Power and Propulsion Conference (VPPC)*, 2012, pp. 1074–1080.

[14] M. Taghipour-GorjiKolaie, S. Razavi, M. Shamsi-Nejad, and A. Darzi, "Inter-turn stator winding fault detection in PMSM using magnitude of reactive power," in *2011 IEEE International Conference on Computer Applications and Industrial Electronics (ICCAIE)*, 2011, pp. 256–261.

[15] Q. Wu and S. Nandi, "Fast single-turn sensitive stator inter-turn fault detection of induction machines based on positive and negative sequence third harmonic components of line currents," in *2008 IAS, IEEEIndustry Applications Society Annual Meeting*, 2008, pp. 1–8.

[16] B.-W. Kim, K.-T. Kim, and J. Hur, "Simplified impedance modeling and analysis for inter-turn fault of IPM-type BLDC motor," *Journal of Power Electronics*, 2012.

[17] A. Sarikhani and O. Mohammed, "Inter-turn fault detection in PM synchronous machines by physics-based back electromotive force estimation," *IEEE Transactions on Industrial Electronics*, vol. 60, no. 8, pp. 3472–3484, 2013.

[18] M. Hadef, M. Mekideche, and A. Djerdir, "Vector controlled permanent magnet synchronous motor (pmsm) drive with stator turn fault," in *2010 XIX International Conference on Electrical Machines (ICEM)*, 2010, pp. 1–6.

[19] B. Vaseghi, B. Nahid-Mobarakeh, N. Takorabet, and F. Meibody-Tabar, "Experimentally validated dynamic fault model for PMSM with stator winding inter-turn fault," in *IAS 2008 IEEE Industry Applications Society Annual Meeting*, 2008, pp. 1–5.

[20] N. Leboeuf, T. Boileau, B. Nahid-Mobarakeh, N. Takorabet, F. Meibody-Tabar, and G. Clerc, "Inductance calculations in permanent-magnet motors under fault conditions," *IEEE Transactions on Magnetics*, vol. 48, no. 10, pp. 2605–2616, 2012.

[21] A. Gandhi, T. Corrigan, and L. Parsa, "Recent advances in modeling and online detection of stator interturn faults in electrical motors," *IEEE Transactions on Industrial Electronics*, vol. 58, no. 5, pp. 1564–1575, 2011.

[22] G. Vinson, M. Combacau, T. Prado, and P. Ribot, "Permanent magnets synchronous machines faults detection and identification," in *IECON 2012 - 38th Annual Conference on IEEE Industrial Electronics Society*, 2012, pp. 3925–3930.

[23] K. Liu, Z. Zhu, and D. Stone, "Parameter estimation for condition monitoring of PMSM stator winding and rotor permanent magnets," *IEEE Transactions on Industrial Electronics*, vol. 60, no. 12, pp. 5902–5913, 2013.

[24] T. Boileau, N. Leboeuf, B. Nahid-Mobarakeh, and F. Meibody-Tabar, "Stator winding inter-turn fault detection using control voltages demodulation," in *2012 IEEE Transportation Electrification Conference and Expo (ITEC)*, 2012, pp. 1–6.

[25] Y. Lee and T. Habetler, "An on-line stator turn fault detection method for interior PM synchronous motor drives," in *APEC 2007 - Twenty Second Annual IEEE Applied Power Electronics Conference*, 2007, pp. 825–831.

[26] T. Boileau, B. Nahid-Mobarakeh, and F. Meibody-Tabar, "Back-emf based detection of stator winding inter-turn fault for PM synchronous motor drives," in *Vehicle Power and Propulsion Conference, VPPC 2007.*, 2007, pp. 95–100.

[27] S. Cheng, P. Zhang, and T. Habetler, "An impedance identification approach to sensitive detection and location of stator turn-to-turn faults in a closed-loop multiple-motor drive," *IEEE Transactions on Industrial Electronics*, vol. 58, no. 5, pp. 1545–1554, 2011.

[28] C.-Z. Liaw, W. Soong, B. Welchko, and N. Ertugrul, "Uncontrolled generation in interior permanent-magnet machines," *IEEE Transactions on Industry Applications*, vol. 41, no. 4, pp. 945–954, 2005.

[29] T. Jahns, "Uncontrolled generator operation of interior PM synchronous machines following high-speed inverter shutdown," in *Industry Applications Conference, 1998. Thirty-Third IAS Annual Meeting.*, vol. 1, 1998, pp. 395–404 vol.1.

[30] A. Mitcham, G. Antonopoulos, and J. J. A. Cullen, "Implications of shorted turn faults in bar wound PM machines," *IEE Proceedings on Electric Power Applications*, vol. 151, no. 6, pp. 651–657, 2004.

[31] B. Welchko, T. Jahns, W. Soong, and J. Nagashima, "IPM synchronous machine drive response to symmetrical and asymmetrical short circuit faults," *IEEE Transactions on Energy Conversion*, vol. 18, no. 2, pp. 291–298, 2003.

[32] B. Welchko, T. Jahns, and T. Lipo, "Short-circuit fault mitigation methods for interior PM synchronous machine drives using six-leg inverters," in *PESC 2004, The IEEE 35th Annual Power Electronics Specialists Conference*, vol. 3, 2004, pp. 2133–2139 Vol.3.

[33] Z. Sun, J. Wang, G. Jewell, and D. Howe, "Enhanced optimal torque control of fault-tolerant PM machine under flux-weakening operation," *IEEE Transactions on Industrial Electronics*, vol. 57, no. 1, pp. 344–353, 2010.

[34] J. G. Cintron-Rivera, A. S. Babel, E. E. Montalvo-Ortiz, S. N. Foster, and E. G. Strangas, "A simplified characterization method including saturation effects for permanent magnet machines," in *2012 XXth International Conference on Electrical Machines (ICEM)*, 2012, pp. 837–843.

[35] A. S. Babel, S. N. Foster, J. G. Cintron-Rivera, and E. G. Strangas, "Parametric sensitivity in the analysis and control of permanent magnet synchronous machines," in *2012 XXth International Conference on Electrical Machines (ICEM)*, 2012, pp. 1034–1040.

[36] K. Rahman and S. Hiti, "Identification of machine parameters of a synchronous motor," *IEEE Transactions on Industry Applications*, vol. 41, no. 2, pp. 557–565, 2005.

[37] B. Cheng and T. Tesch, "Torque feedforward control technique for permanent-magnet synchronous motors," *IEEE Transactions on Industrial Electronics*, march 2010.

[38] A. Babel, J. Cintron-Rivera, and E. Strangas, "A multiple look-up table torque controller for improved performance of ipm machines," in *2013 IEEE International Electric Machines Drives Conference*, May 2013, pp. 521–525.

[39] C.-T. Pan and S.-M. Sue, "A linear maximum torque per ampere control for IPMSM drives over full-speed range," *IEEE Transactions on Energy Conversion*, june 2005.

[40] C. Nino, A. Tariq, S. Jurkovic, and E. Strangas, "Optimal speed control of an interior permanent magnet synchronous motor including cross saturation," in *2009 IEEE International Electric Machines and Drives Conference*, may 2009, pp. 292 –298.

[41] C. Mademlis, I. Kioskeridis, and N. Margaris, "Optimal efficiency control strategy for interior permanent-magnet synchronous motor drives," *IEEE Transactions on Energy Conversion*, vol. 19, no. 4, pp. 715 – 723, dec. 2004.

[42] J. Cintron-Rivera, S. Foster, W. Zanardelli, and E. Strangas, "High performance controllers based on real parameters to account for parameter variations due to iron saturation," in *2013 Ndia Ground Vehicle Systems Engineering And Technology Symposium*, August 2013.

[43] J. Cintron-Rivera, S. Foster, C. Nino-Baron, and E. Strangas, "High performance controllers for interior permanent magnet synchronous machines using look-up tables and curve-fitting methods," in *2013 IEEE International Electric Machines Drives Conference*, May 2013, pp. 268–275.

[44] A. Babel, J. Cintron-Rivera, S. Foster, and E. Strangas, "Evaluation of a parameter identification method for permanent magnet AC machines through parametric sensitivity analysis," *IEEE Transactions on Energy Conversion*, vol. 29, no. 1, pp. 240–249, March 2014.

[45] T. Herold, D. Franck, E. Lange, and K. Hameyer, "Extension of a d-q model of a permanent magnet excited synchronous machine by including saturation, cross-coupling and slotting effects," in *2011 IEEE International Electric Machines Drives Conference*, May 2011, pp. 1363–1367.

[46] N. Leboeuf, T. Boileau, B. Nahid-Mobarakeh, N. Takorabet, F. Meibody-Tabar, and G. Clerc, "Estimating permanent-magnet motor parameters under inter-turn fault conditions," *IEEE Transactions on Magnetics*, vol. 48, no. 2, pp. 963–966, 2012.

[47] B.-G. Gu, J.-H. Choi, and I.-S. Jung, "Development and analysis of interturn short fault model of pmsms with series and parallel winding connections," *Power Electronics, IEEE Transactions on*, vol. 29, no. 4, pp. 2016–2026, April 2014.

[48] S. N. Foster, "Operation of interior permanent magnet synchronous machines with fractional slot concentrated windings under both healthy and faulty conditions," *Dissertation–Michigan State University. Electrical Engineering - Doctor of Philosophy, 2013.*, December 2013.

[49] J. Pyrhonen, "Design of rotating electrical machines," *US, Wiley, Feb. 2007, 0*, vol. 1, pp. 1–512.